Dependencies of SDSS Supernova Ia Rates on their Host Galaxy Properties

by

Yan Gao
B.Sc., Nanjing University, 2009

A Thesis Submitted in Partial Fulfillment of the
Requirements for the Degree of

MASTER OF SCIENCE

in the Department of Physics & Astronomy

Dependencies of SDSS Supernova Ia Rates on their Host Galaxy Properties

by

Yan Gao
B.Sc., Nanjing University, 2009

Supervisory Committee

Dr. C. J. Pritchet, Supervisor
(Department of Physics & Astronomy)

Dr. D. A. VandenBerg, Departmental Member
(Department of Physics & Astronomy)

Dr. F. Herwig, Departmental Member
(Department of Physics & Astronomy)

Supervisory Committee

Dr. C. J. Pritchet, Supervisor
(Department of Physics & Astronomy)

Dr. D. A. VandenBerg, Departmental Member
(Department of Physics & Astronomy)

Dr. F. Herwig, Departmental Member
(Department of Physics & Astronomy)

ABSTRACT

Studying how SN Ia rates (SNR) correlate with host galaxy properties is an important step in understanding the exact nature of SN Ia. Taking a sample of SNe and galaxies from the SDSS, we obtain the optimum parameter values for the A+B model for SNR, which states that SNR scale linearly with mass and star formation rate of the host, and compare them with previous work. We then proceed to show that the A+B model deviates very significantly from the SNR behaviour in our sample, demonstrate that no reasonable values for A and B could possibly match the observations, and investigate the possibility of a third-parameter correction to the generic A+B model. We find that several hypothesised models seem to match the distribution of SNRs in our sample; however, discriminating between them is a difficult task. We interpret the above to be an indicator that a new parameter may need to be taken into account when modelling SNR, and we present metallicity as a possible candidate for the new parameter. Also, by investigating decomposed bulge + disk components of the host galaxies, we find that the spatial positions of SNe Ia are correlated with bulge luminosity, but not with galaxy total luminosity or disk luminosity. It is also shown that SNe do not preferentially occur in bulge-dominated galaxies. Our interpretation of these results is that SNe arise from a population having a spatial distribution which

correlates very well with bulge luminosity, but does not usually contribute to bulge luminosity.

Table of Contents

List of Tables

List of Figures

ACKNOWLEDGEMENTS

First of all, I would like to thank my dear supervisor Chris Pritchet for supporting me through the past two years, for his patience and tolerance towards my social incompetence, and for guiding me through the turbulences of research. Many were the times that he pointed out my blundering errors and made suggestions which were vital to the completion of this work. Many were the times that he intervened to straighten issues for me when I was in a state of crisis. Most important of all, many were the times that he showed undue respect towards my naive ideas, even when they contradicted his, and even acknowledged them in the preciously few instances when I was right. He consistently let me speak first whenever we both had something to say, thereby raising my awareness that I had the tendency to interrupt people in mid-speech, a feat I would have probably been incapable of had I been in his shoes. If I were ever to become a supervisor to a student of my own, I wish I could emulate what he has been and done, in both tutorship and integrity.

Thanks to my committee members, Don VandenBerg and Falk Herwig, for supporting me throughout, even though I understand that I make poor presentations of my work. Thanks to the external examiner Sebastien Fabbro for his helpful suggestions.

Thanks also go to Sara Ellison, Trevor Mendel, and Luc Simard, for their help with navigating the SDSS and llaima databases, without whom this thesis would not have been possible. Sara also provided the initial inspiration for this work during a conversation with my supervisor, in addition to providing the author access to the llaima database. Trevor, an officemate of the author by the time this manuscript was complete, always patiently and helpfully guided the author with issues concerning the databases, whenever that guidance was needed. Luc has been a person exceedingly enthusiastic about helping the author, in one instance providing a whole program written in python for the purpose of making remote queries of the SDSS DR7 database. I owe them.

Thanks to my friends and fellow grad students for all the support I have received from them. Thanks to my academic elder sister Melissa Graham, for showing me the ropes during my first few months. Thanks to Razzi Movassaghi and Jean-Claude Passy, for academically significant discussion, and for support during my darkest of times. Thanks to Benjamin Hendricks, for explaining to me how to obtain dust attenuations from H_α/H_β, and for his consistent tolerance of my whims. Thanks

to Charli Sakari and Hannah Broekhoven-Fiene, for patiently explaining to me the ethical system under which they operate, and for respecting the fact that I could never conform to it. Thanks to Sarah Sadavoy and Andrew Pon for leisurely debates on non-academic matters. Thanks to Lisa Glass for her brief period of support, though why it ended abruptly I will never know. Thanks to Monica Turner, for being a very special person, and for putting up with all the stress I have caused, and once again to Hannah Broekhoven-Fiene, who stepped into the situation to resolve a conflict that could have turned out to be very ugly.

Last but not least, I would like to thank all the people who submitted to astro-ph the papers that I have read over the years, for honing my understanding of the world, for their contribution to science in general, and for further educating a species which I now unprecedentedly understand has a long way to go along the path of enlightenment.

DEDICATION

To my dear Mum & Dad,
I dedicate my contribution to our destiny,
to understand the mountains and seas,
the soul of man,
and the stars beyond...

Chapter 1

Introduction

1.1 Type Ia Supernovae and Their Rates

At the end of their lifetimes, many stars explode, and eject the material which they are comprised of back into the interstellar medium. Such explosions, which usually occur on a timescale of tens of days, and release an amount of visible light comparable to the luminosity of a typical galaxy (about $10^{10}L_{\odot}$, where $L_{\odot}$ is the luminosity of our sun, about $3.8{\times}10^{26}W$), are called supernovae.

Supernovae are among the most intensely studied objects in modern astronomy. They are important sources of stellar feedback, a process by which stars dump material back into the interstellar medium (ISM) to form molecular clouds, and hence a new generation of stars. This feedback is also responsible for producing much of the metals (elements heavier than Helium) found in the ISM. In addition, their spectra allow us to observe the internal chemical components within dying stars which would otherwise not have been seen, which places vital constraints on chemical evolution models. They are also known to be prominent neutrino sources, and contribute to our understanding of these elusive particles.

Not all supernovae are the same; in general, they can be classified into Type I supernovae and Type II supernovae, the dividing criterion being whether or not hydrogen emission lines are observed in the spectra which they emit (Minkowski 1941). Type I supernovae, which are the ones with no hydrogen emission lines, are further subdivided into Type Ia, Ib and Ic supernovae. The difference between these subdivisions again lies in their spectra (Filippenko 1997, see Figure 1.1 for details). Type Ia supernovae are characterized by their prominent Si II absorption lines, as

well as a multitude of emission lines from iron peak elements, most notably iron (Fe) and cobalt (Co). (^{56}Ni is also synthesized during the explosion, but this has nothing to do with the definition of a Type Ia.) Type Ib and Ic supernovae do not harbour any Si II absorption lines, and, observationally, the difference between them is that Type Ib supernovae show traces of helium (He), while Type Ic supernovae do not.

Of the many different types of supernovae (hereby abbreviated as SNe, which is the plural form, SN being the single form), this work will focus on Type Ia supernovae (hereby abbreviated as SNe Ia).

Perhaps the most important aspect of SNe Ia is their so-called "standard candle" properties. A perfect standard candle is defined as a class of objects which has exactly the same total intrinsic luminosity which is invariant with time and position, and which has a common property other than luminosity by which they can be identified. Such a class of objects, if widely scattered in the universe and luminous enough to be observable, are extremely valuable for the purposes of precision cosmology (explained in the next few paragraphs). In reality, small variations always exist between different members of a class of objects, and we have to satisfy ourselves with either objects which have a negligible variation in luminosity, or possess some other property by which luminosity can be calibrated.

Supernovae of type Ia are believed to be one of the most reliable standard candles for cosmological purposes (Riess et al. 1998, Perlmutter et al. 1999). There are two reasons for this. The first is that the peak luminosities of SNe Ia are inherently very stable, with a small dispersion which was consistent with a null hypothesis for no dispersion according to some early papers on the subject (eg Colgate 1979). Thus, it can be said that SNe Ia all have a similar intrinsic luminosity to a very high degree. The second is that this dispersion can be further corrected; Phillips (1993) noted that, while the afore mentioned dispersion amounted to 0.5 magnitudes (abbreviated as mags for the rest of this thesis) in terms of I band standard deviation, more luminous SNe Ia tend to last a longer duration in its rest-frame (i.e. corrected for redshift time dilation). Hence, once the rest-frame duration of a given SN Ia is known, the intrinsic peak luminosity of this particular SN Ia can be derived from this information alone, to a very high accuracy. Quantitatively, this can be done by defining the "stretch parameter" s (Perlmutter et al. 1997, 1999):

$$t = st_s, \tag{1.1}$$

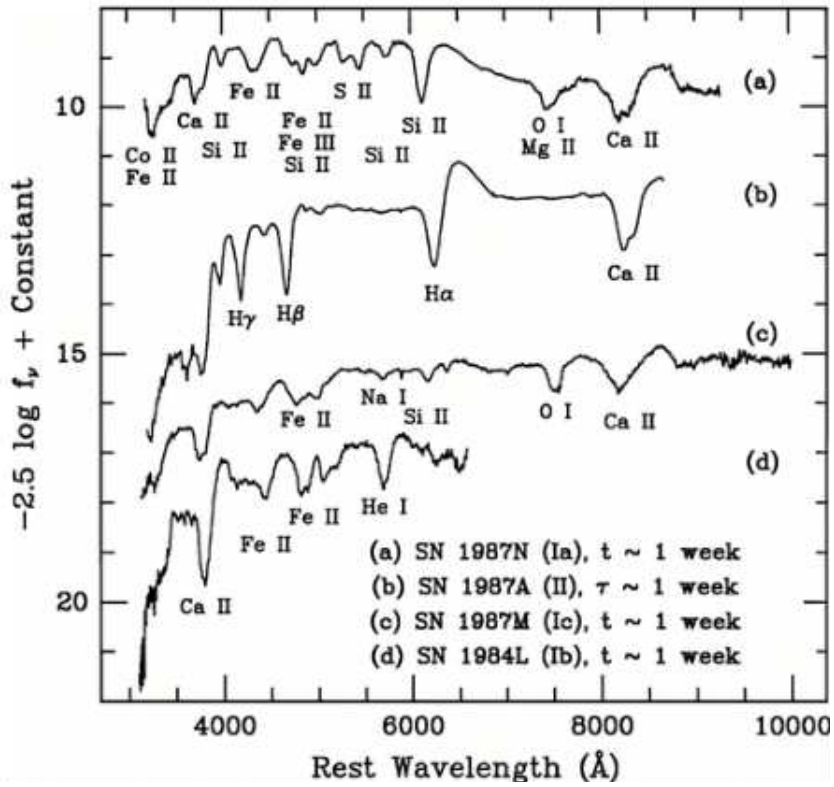

Figure 1.1: Spectra of different classes of SNe. This figure was taken from Filippenko (1997).

where t_s is some arbitrary constant typical standard timescale of a SN Ia (usually taken to be a sample average of some sort), and t is the observed rest-frame duration. Note that, when fitting s according to this equation, the entire light curve needs to be scaled to fit the standard template, not just the duration. The peak rest-frame luminosity in magnitudes M can then be calculated from

$$M = M_s + \alpha(s - 1), \tag{1.2}$$

where M_s is the peak luminosity corresponding to t_s, and α is an empirically constrained constant, usually of the order of 1.5. (Note that Phillips 1993 did this differently, using the luminosity drop 15 days after peak light, which should theoretically measure the same effect.)

In addition to the stretch factor, SNe luminosities can also be further calibrated by their colour. In principle, bluer SNe tend to be brighter (e.g., Guy et al. 2005). To correct for this, another term is added to the equation above:

$$M = M_s + \alpha(s - 1) - \beta c, \tag{1.3}$$

where β is some constant equal to roughly 1.5 (e.g., Astier et al. 2005), and c is the colour of the SN Ia at maximum light, defined as $(\text{B-V})_{max}$+0.057 in the case of Guy et al. (2005).

Peak luminosities calculated via a combination of stretch and colour corrections have a dispersion of only $\sim$0.1 magnitudes (e.g., Folatelli et al. 2010).

As mentioned above, one of the most prominent applications for this unique property of SNe Ia is in cosmology. For the currently dominant "Big Bang" model, the universe is globally expanding. Since the intrinsic luminosity of each SN Ia can be determined from s, and the observed flux can be measured by observation, some measure of the distance between the observer and the SN Ia can be obtained:

$$D_L = \sqrt{\frac{L}{4\pi F_{obs}}}, \tag{1.4}$$

where D_L is the luminosity distance, L is the SN Ia luminosity, and F_{obs} is the observed flux.

Wavelengths of any photons emitted by an object also expand with the global expansion of the universe mentioned above, and are consequently redshifted as time goes on. It is possible to measure by what factor the universe has expanded since SN

photons were emitted, simply by measuring the redshift of the SN spectrum. Hence, for a given SNe Ia, it can be calculated by how much the universe has expanded during the time it took for a photon to travel the distance from the SN Ia to the observer. Given enough SNe at different redshifts, the expansion history of the universe can be reconstructed.

To recover the time it takes for a photon to travel the distance from the SN Ia to the observer, it seems intuitive that one could do this by dividing the distance by the speed of light c. However, this distance is not the same as D_L.

According to the ΛCDM model, there are three parameters which affect the expansion of the universe: H_0, the Hubble parameter, Ω_M, the mass density parameter, and Ω_Λ, the dark energy density parameter. Ω_M decelerates the expansion of the universe, while Ω_Λ tends to accelerate it. For the case of a flat universe, the distance a SN Ia photon needs to travel in order to reach the observer is equal to the comoving distance D_C, which can be expressed as

$$D_C = D_H \int_0^z \frac{dx}{\sqrt{\Omega_M(1+x)^3 + \Omega_\Lambda}}, \tag{1.5}$$

where D_H is the Hubble distance (the radius of the observable universe at the present epoch, assuming that the rate of expansion has been H_0 since the big bang, equal to the speed of light c divided by H_0) and z is the redshift. D_C and D_L are related in the sense that

$$D_L = (1+z)D_C; \tag{1.6}$$

therefore

$$\sqrt{\frac{L}{4\pi F_{obs}}} = (1+z)D_H \int_0^z \frac{dx}{\sqrt{\Omega_M(1+x)^3 + \Omega_\Lambda}}, \tag{1.7}$$

and since L, F_{obs} and z are observables, and D_H is a known constant, Ω_M and Ω_Λ can be constrained from the calculations. The resulting constraints played an important role in the establishment that $\Omega_M = 0.27$, $\Omega_\Lambda = 0.73$.

Of course, there exist other non-mainstream cosmological models. Using similar principles, SNe Ia have been used to constrain them as well (e.g., Benitez-Herrera et al. 2011). However, such studies are beyond the scope of this work, and will not be discussed in detail here.

Note that all the work done above was completed under the assumption that all SNe Ia are more or less identical in both spectral features and intrinsic luminosity

after stretch calibration is applied, or at the very least do not have redshift-dependent systematic variations in such properties. To be confident of this assumption, one must know enough about SNe Ia to say that their properties are statistically the same at any redshift, and that the calibration methods mentioned above will yield standard candles regardless of how different the early (high-redshift) universe was in comparison to the universe we see today. However, variations among SNe Ia have been detected.

Almost immediately after the original work on SN Ia cosmology, Sullivan et al. (2006) found that SNe Ia hosted by star-forming galaxies tend to have a larger stretch parameter s, while those hosted by passive galaxies have a smaller s. Another study (Sullivan et al. 2010) found that more massive galaxies tend to host brighter SNe. Moreover, Gupta et al. (2011) found that, again for the same stretch, the luminosity of a hosted SN Ia increases with the host galaxy's age, as well as independently confirming the mass effects as found by Sullivan et al. (2010). The potential effect of these variations on cosmological work is not yet well understood.

Even if the systematic effects caused by the variations above are already known and have been corrected for, it is still not certain whether there are more unknown systematic effects which we do not yet know of. In order to completely eliminate such effects to any satisfactory degree, one must be familiar with the progenitors of SNe Ia (the stars which explode to become SNe Ia and the stellar systems which provide the environment for the formation of such stars). Studying the redshift variations of the progenitors, given the knowledge of exactly what the progenitors are, would give us a much better chance to reveal the exact nature of the variations. However, the identity of SN Ia progenitors has proven to be notoriously elusive. It has been pointed out (e.g., Hillebrandt & Niemeyer 2000) that the objects which explode to give rise to SNe Ia are very probably carbon-oxygen white dwarfs (abbreviated as COWD for the rest of this thesis) which have somehow attained enough mass to cause the unstable ignition of carbon and oxygen. This critical mass is called the Chandrasekhar mass limit (Chandrasekhar 1931). In order for a COWD to detonate under normal cosmic conditions, it must reach the Chandrasekhar mass limit (measured to be $1.38 M_{\odot}$), which satisfies the condition of having the same mass at detonation. In addition, no neutron stars or black holes are found at the sites of SN Ia occurrences. Since all stars with an initial mass $> 8 M_{\odot}$ are thought to form neutron stars or black holes after undergoing SN explosions, it logically follows that SNe Ia could only form from stars with an initial mass $< 8 M_{\odot}$, which tend to form white dwarfs at the end of their lifetimes. Additional arguments in favour of this hypothesis are as follows (Pritchet

et al. 2008). The early spectra of SNe Ia typically agree well with the spectra of an exploding COWD, especially the lack of hydrogen in the spectra, suggesting that it is COWDs which detonate to form them. Also, due to the fact that SNe Ia show a small dispersion of luminosity, it is likely that all SNe Ia progenitors have more or less the same mass at the time of detonation, and this luminosity is consistent with the conversion of C and O to Fe. The shape of observed SN Ia light curves are in agreement with that predicted for an exploding COWD. Lastly, SNe Ia have been known to occur in old stellar populations which contain low mass stars, which could not have undergone gravitational collapse to release the amount of energy observed.

In sharp contrast to the degree of confidence to which we claim that it is COWDs which explode to form SNe Ia, nobody knows exactly how they explode. COWDs are extremely faint objects, limiting the number which can be observed, and it is extremely hard to predict when one would detonate. Consequently, no direct observation of a SN Ia progenitor has ever been made, and the mechanism is still open to much speculation, with many models having been proposed. Among the many models proposed, there exist two mainstream hypotheses as to how the detonation happens: the "single degenerate" (SD) and the "double degenerate" (DD) models.

The SD model (Nomoto 1982, Hachisu et al. 1996) assumes that the progenitor COWD, less massive than the Chandrasekhar mass limit, is in a binary system, with the companion star being a younger, evolving star (usually a main sequence or red giant star). The companion star expands as it evolves, gradually filling up its Roche Lobe and giving up mass to the COWD. The COWD accretes this mass, gradually becoming more massive until it reaches the Chandrasekhar mass limit, whereupon it detonates. This model yields approximately the same SN Ia rates as those which are observed (Han & Podsiadlowski 2004). However, Kasen et al. (2009) conducted simulations of the effects of the companion star on the SN Ia shock wave, and found that asymmetries in the detonation due to the effect of the companion star should result in a luminosity excess for SNe Ia, which was not observed (e.g., Bianco et al. 2011). Other problems with this model have also been found. Investigating delay time distributions (to be defined in the next section), many authors (e.g., Greggio 2005, Mennekens et al. 2010) have found that SD models predict too steep a delay time distribution in comparison to what is observed. Pritchet et al. (2008) analytically found that COWD formation must be consistently $\sim$100 times the rate of observed SNe Ia, regardless of the mass of the COWD population involved. This is unrealistic, as less massive COWDs need to accrete more mass to allow detonation, which is

harder to obtain. Other studies show that SNe Ia which form via the SD model are likely to be significant X-ray sources during the accretion phase, but that the amount of X-ray emission is well below that expected for the expected SN Ia rate for certain regions (e.g., Gilfanov & Bogdán 2010). Thus, it is unlikely that the SD model is the only channel by which SNe Ia are formed, if it is one at all.

The DD model asserts that the progenitor of a SN Ia is in fact two COWDs in a binary system. There are two ways by which this can happen. One is by merging, forming a single body with the sum of the masses. This model has long been controversial, since it is hard in theory for a COWD-COWD binary to merge. Simple Newtonian two-body motion could never merge such a system, and merging by losing potential energy via gravitational waves takes too long ($\sim t_H$) to be plausible for all but the closest binaries. Although new life has been breathed into this model by a proposed third star in the system accelerating gravitational radiation (Thompson 2010), the birth rate of such triple stars is not very well-known. It is also expected that there is a significant probability that the two merging COWDs will result in an object well in excess of the Chandrasekhar mass limit, thereby generating an object much more luminous. This would explain the existence of "superluminous" SNe Ia well (Howell et al. 2006), but since a great majority of SNe Ia are not superluminous, this cannot be the main SN Ia formation channel. Also, such superluminous SNe do not follow the stretch-luminosity correlation explained above, so for the purposes of conventional cosmology investigations, SNe Ia formed through this formation channel serve to be contaminants (Howell et al. 2006). The other way by which binary COWDs can give rise to SNe Ia is by one of the WDs being tidally stripped of material by the other, resulting in a Roche lobe overflow similar to the SD model. It has been found (e.g., Mennekens et al. 2010) that this progenitor channel has good predictions of the delay time distribution (see next section for definition). However, very close binary pairs are also required for this scenario, limiting the total SN rate predicted by the DD model.

Worthy of note is the fact that, aside from the effects found by Kasen et al. (2009), the properties of SN Ia light curves are not sensitive to whether it is a SD or DD model which gives rise to SNe Ia. This is because during the detonation, the shock front that emits the light we see quickly becomes much larger in size than the distance between the SN Ia and the companion.

Both the SD and DD models fall short of giving an unequivocal explanation of what has been observed, and the mechanism by which COWD gain enough mass to

explode remains a mystery.

An alternative approach to the question of the identity of SN Ia progenitors is the investigation of the rates at which they form as a function of the host galaxy or environment properties. Once these rates are obtained, they can be compared with the predictions of theoretical models (e.g., Wang et al. 2010), and constraints can be placed on the models. Moreover, if it can be demonstrated that SNe preferentially form in galaxies which exhibit certain properties, then those properties could place constraints on the nature of the detonation mechanism. Models have been proposed to empirically fit SN Ia rates as a function of potential host galaxy properties.

The properties which have been included in models for SNe Ia rates include redshift (e.g., Dilday 2010b), host galaxy age (e.g., Gupta et al. 2011), environment galaxy number density (e.g., Cooper et al. 2009), and mass & star formation rate of the host (e.g., Sullivan et al. 2006, to be elaborated on later). It has also been found that SNe more or less follow host galaxy light within the host (e.g., Kelly et al. 2008), but nothing has been done so far to constrain the morphological components of a galaxy which give rise to SNe.

1.2 The A+B Model

One of the most prominent models for SN Ia rates is the so-called "A+B" model. Inspired by Mannucci et al. (2005), who found that SN Ia rate per unit mass was much higher for late-type (star-forming) galaxies, it was first presented by Scannapieco & Bildsten 2005 (SB05) in its explicit form

$$SNR = A{\cdot}M + B{\cdot}SFR \quad , \tag{1.8}$$

where SNR is the SN Ia rate, M is the stellar mass involved, and SFR is the star formation rate. The rationale behind this model is that the delay times (the time needed for a newly formed star to evolve into a SN Ia, abbreviated as DTs) of SNe are varied, leading many to think that SNe Ia can be divided into "prompt" and "delayed" classes. The former consists of SNe Ia which explode very soon after the progenitor star is formed, thus being proportional to the SFR, while the latter contains SNe Ia resulting from stars which have formed an indefinitely long time ago, and are consequently more or less proportional to the total stellar mass.

Taking the delay time distribution (number of SNe Ia of a certain DT as a function

of DT, abbreviated as DTD) of SNe Ia as a function of the delay time t_{DT} to be $D(t_{DT})$, and the SFR relative to local time t to be $SFR(t)$, then the SNR is given by a simple convolution of the two:

$$SNR(t) = D(t) * SFR(t) \quad , \tag{1.9}$$

or, in explicit integral form,

$$SNR(t) = \int_{-\infty}^{+\infty} D(\tau) \cdot SFR(t-\tau) d\tau = \int_{0}^{+\infty} D(\tau) \cdot SFR(t-\tau) d\tau \quad . \tag{1.10}$$

where the second equality sign is due to the fact that $D(\tau)$ is always 0 when $\tau < 0$.

As already mentioned, the DTD was approximated in SB05 by an overlay of two components: (1) the "prompt" component, which consists of a delta function at $t = 0$, and (2) the "delayed" component, consisting of a flat distribution for $t > 0$. Later research has found the approach by SB05 to be a good approximation to observations (e.g., Sullivan et al. 2006), and the A+B model has been in use ever since, even though it has been found that the DTD is well described by a single power law distribution (Totani et al. 2008, Pritchet et al. 2012).

Thus, we take $D(t) = A + B\delta(0)$ for $t \geq 0$, and substitute into Eq.(1.10):

$$SNR(t) = A \int_{0}^{t} SFR(t) dt + B \cdot SFR(t) \quad . \tag{1.11}$$

Neglecting the stellar mass that is lost through evolution, $\int_0^t SFR(t) dt$ is equal to the total stellar mass of the system concerned, which in turn gives us Eq.(1.9).

Having made these assumptions, SB05 proceeded to make simplified estimates for the values of A and B, based on special populations with either negligible mass or negligible star formation. Using SNe Ia found in E/S0 galaxies, which are considered to be passive (having no star formation) for these purposes, they obtained $A = 4.4^{+1.6}_{-1.4} \times 10^{-14}/\mathrm{yr}/M_{\odot}$. For B, they found two different values which agree with each other within error bars: $B = 2.6 \pm 1.1 \times 10^{-3}/\mathrm{yr}/M_{\odot}\mathrm{yr}^{-1}$ from core-collapse rates, and $B = 1.2^{+0.7}_{-0.6} \times 10^{-3}/\mathrm{yr}/M_{\odot}\mathrm{yr}^{-1}$ from blue starburst galaxies. See Chapter 3 for a table summarizing these and other values of A and B for the A+B model.

It was not long before significant improvements were made to this method. Neill et al. (2006), and later Dilday et al. (2008), assumed the averaged star formation history results obtained by Hopkins & Beacom (2006), which expressed average SFR

density in the universe as a function of redshift only:

$$\dot{\rho}(z) = \frac{a+bz}{1+(z/c)^d} h M_{\odot} yr^{-1} Mpc^{-3} \quad , \tag{1.12}$$

where $a = 0.0118$, $b = 0.08$, $c = 3.3$, $d = 5.2$, and z is the redshift. This yielded SFRs which are statistically correct for a given spatial volume, from which results for A and B can be obtained by means of applying statistical methods over a large sample. These results were independent from the earlier ones by SB05: Neill et al. (2006) obtained $A = 1.4 \pm 1.0 \times 10^{-14}/\mathrm{yr}/M_{\odot}$, $B = 8.0 \pm 2.6 \times 10^{-4}/\mathrm{yr}/M_{\odot}\mathrm{yr}^{-1}$, while Dilday et al. (2008) found $A = 2.8 \pm 1.2 \times 10^{-14}/\mathrm{yr}/M_{\odot}$, $B = 9.3^{+3.4}_{-3.1} \times 10^{-4}/\mathrm{yr}/M_{\odot}\mathrm{yr}^{-1}$ with different data. However, these authors did not have the means to directly determine the stellar masses and SFRs of each individual SN Ia host galaxy in a reliable manner.

Sullivan et al. (2006) used multi-band photometry to obtain the stellar masses and SFRs of each individual host by means of fitting a best-fit PEGASE2 spectral template (Fioc & Rocca-Volmerange 1997) to the photometry while calculating A+B rates, obtaining an advantage which had been denied to the previous authors. This way, the complexities induced by a redshift-dependent SFR no longer existed, and the A+B fit results were more reliable. They ultimately concluded that $A = 5.3 \pm 1.1 \times 10^{-14}/\mathrm{yr}/M_{\odot}$, $B = 3.9 \pm 0.7 \times 10^{-4}/\mathrm{yr}/M_{\odot}\mathrm{yr}^{-1}$. This is may be the most reliable A+B fit to date.

It has been found that SNRs are not perfectly described by the A+B model. Smith et al. (2011) (see also Li et al. 2010) investigated SDSS II SNe and photometric galaxies of the SDSS, and obtained photometric masses and SFRs using the same PEGASE2 fits as Sullivan et al. 2006. Using the same methods as Sullivan et al. 2006, Smith et al. (2011) obtained the parameters for the A+B model, and found $A = 2.8^{+0.6}_{-0.5} \times 10^{-14}/\mathrm{yr}/M_{\odot}$, $B = 1.4^{+0.2}_{-0.1} \times 10^{-4}/\mathrm{yr}/M_{\odot}\mathrm{yr}^{-1}$, but demonstrated that it did not match the data well. They also proposed an alternate $AM^x + BSFR^y$ model (referred to as the "Smith model" for the rest of this paper), and found that $A = 1.05 \pm 0.16 \times 10^{-10}$, $B = 1.01 \pm 0.09 \times 10^{-3}$, $x = 0.68 \pm 0.01$, $y = 1.00 \pm 0.05$, which fits the data better than the generic A+B model. Note that the A value is much larger than for a generic A+B fit, due to the index on the mass term. However, this model has no physical explanation, and the power-law index x could be explained as the manifestation of another term which is correlated to galaxy mass. In short, further investigation is required on this issue.

In our analysis in this paper, we use *spectroscopically* determined SFRs from

the SDSS DR7 MPA/JHU value-added catalogue, making our SFR estimates more reliable than those in Sullivan et al. 2006 (and Smith et al. 2011, who rely on the same method as Sullivan et al. to obtain mass and SFR from photometry). The masses we use are also shown to correlate well with more advanced derivations. This is of high significance, since it has been pointed out (e.g., Förster et al. 2006) that the uncertainty in measurements of star formation histories is an important limiting factor in the determination of the values of A and B in the A+B model. In addition, we use a new fitting algorithm based on maximum likelihood, which is shown to be more reliable than previous fitting methods in the case of our sample. The details of these processes will be discussed later.

Apart from investigating what kind of galaxies give rise to SNe Ias, it is also interesting to investigate how they are distributed *within* the hosts. The following section addresses this.

1.3 Empirical Models of Galaxy Components & the Sérsic Profile

To parametrically describe the 2-dimensional radial profiles of different galaxy components, the most prominent and well-used empirical model is the Sérsic profile (Sérsic 1968):

$$I(R) = I(0)e^{[-(\frac{R}{a})^{\frac{1}{n}}]}, \tag{1.13}$$

where $I(x)$ is the surface brightness at x, R is the distance from the centre of the galaxy involved, a is some scale radius, and n is a parameter named the Sérsic index. It has been demonstrated that disks are well represented by a Sérsic profile with a Sérsic index of 1, also called an exponential profile:

$$I(R) = I_0 e^{-\frac{R}{a}}, \tag{1.14}$$

while most (though not all) bulges and elliptical galaxies follow a Sérsic profile with a Sérsic index of 4, known as the de Vaucouleurs profile (de Vaucouleurs 1948):

$$I(R) = I_0 e^{[-(\frac{R}{a})^{\frac{1}{4}}]}. \tag{1.15}$$

Worthy of note is the fact that bulges are always more centrally concentrated than

disks. This makes the bulge and disk profiles somewhat counterintuitive, since an exponential profile always declines faster than a de Vaucouleurs profile *when the same a is adopted*. Consequently, bulge profiles usually have a much smaller scale length. Using the above models, it is only necessary to provide a disk scale length and a bulge scale length to constrain the radial profile of a galaxy.

While the exponential and de Vaucouleurs profiles will suffice for most galaxies, some galaxies have bulges which do not behave as $n = 4$. To model these, the Sérsic index must be fitted simultaneously. Thus, for a radially symmetric galaxy, it takes 5 parameters to fully describe a galaxy's radial profile if it has a non-de Vaucouleurs bulge: the disk scale length, the bulge scale length, a bulge Sérsic index, the total luminosity, and a bulge-to-total light ratio.

In reality, galaxies tend to have an elliptical appearance, and methods for treating this effect vary. For the data that we use in this thesis, the authors (Simard et al. 2011) only fit the scale lengths and bulge Sérsic indices along the major axis (see Chapter 2 for details), and give other parameters as a description of the shape (see Chapter 5).

Some galaxies have an additional component called the nucleus, which is even more concentrated than the bulge. Simard et al. (2011) do not account for such a third component in their fits. We discuss the effect this may have on our results in Chapter 6.

Lastly, since the bulge scale length is always remarkably smaller than the disk scale length, usually by quite a few orders of magnitude, convention has it that bulge scale lengths are usually quoted as the bulge half light radius (the value of R within which half the total light of the bulge is included), which is a function of the Sérsic index and the bulge scale length. Bulge half light radii and disk scale lengths are usually comparable; thus quoting bulge half light radii and disk scale lengths makes it easier to compare the sizes of the two.

1.4 Structure of This Paper

In the introduction above, we have given a brief summary of the significance of SNe Ia, what is known about them, and introduced previous attempts to model supernova rates. We have also mentioned a few concepts concerning galaxy structures that will be important for the rest of this paper.

In Section 2, we present the data samples we use in our studies, which include

the sample of SNe Ia, as well as the essential preprocessing of the data, most notably the matching of the SNe Ia to their host galaxies. We discuss different methods of fitting the parameters of the A+B model using our data in Section 3, where our results, obtained via our optimum fitting method, are also presented. We proceed to point out our new findings about the A+B model; in particular, that it does not model the supernova rates of our data well, in Section 4, and attempt to modify the A+B model to match the observations. We apply tests to the modified models, and eliminate a significant proportion of them. We also investigate the correlation between distribution of SNe Ia within their host galaxies and the distribution of host galaxy light in Section 5. We discuss the interpretation of our results, as well as the implications for future studies in the field, in Section 6. We give a full summary of our results in Section 7.

Chapter 2

Data

To investigate how SNe Ia rates are correlated with different galaxy properties, data need to be collected on a sample of galaxies with known properties, as well as on the frequency of SNe Ia hosted by them. In our case, most of these data have already been collected by previous studies. The SDSS project has sampled a large number of galaxies, and the information on the sampled galaxies has been made public via its DR7 data release (Abazajian et al. 2009). Much of the information sampled for each given galaxy has already undergone rigorous refining, most notably a subset with masses, and star formation rates (Kauffmann et al. 2003, Brinchmann et al. 2004, Tremonti et al. 2004) having been derived. The SDSS II supernova survey, conducted in conjunction with the SDSS project, obtained hundreds of SNe Ia within the same sky area, providing information on the rates within these host populations.

Once these data have been obtained, we need to match the observed SNe Ia to appropriate host galaxies, such that statistical methods can be applied in later chapters to retrieve the correlations we seek.

This chapter presents a brief introduction to how the previous work mentioned above was extracted and how it was modified for use in this thesis.

2.1 The SDSS Project

To obtain a generalised view of the demographics of the objects in the universe, it is usually desirable to make observations over a large solid angle. Such observations tend to sacrifice resolution and depth in exchange for a wide observing field, and are reliable as a magnitude-limited census of objects within the field of observation.

The Sloan Digital Sky Survey (SDSS) is one such survey (Abazajian 2009). Using a 2.5m telescope located at Apache Point Observatory, observations were made over 11,000 deg^2 of sky in 5 photometric bands, dubbed u,g,r,i and z. This is slightly different from the originally proposed $u'g'r'i'z'$ system (Gunn et al. 1998) due to a series of mechanical failures, mostly filters reacting poorly to moisture (Doi et al. 2010); this system is completely unrelated to the Thuan-Gunn photometric system (Thuan & Gunn 1976). The photometry is calibrated to an AB magnitude system (where 1 ergs·cm^{-2}·s^{-1}·Hz^{-1} corresponds to -48.60 mags, or 0 mags corresponds to 3.63×10^{-20} ergs·cm^{-2}·s^{-1}·Hz^{-1}), and has a limiting magnitude of 22.0, 22.2, 22.2, 21.3 and 20.5 for the 5 bands respectively, with the g and r bands having the deepest observations. For this paper, we use the data from r band observations for the photometric sample.

The 11,000 deg^2 observation area is divided into the >7,500 deg^2 covering the North Galactic Cap in addition to a few other areas (Stripes 76, 82 and 86, see below), called the Legacy footprint area, and the >3,500 deg^2 at lower Galactic latitudes, named the Sloan Extension for Galactic Understanding and Exploration (SEGUE) footprint area. These areas are further divided into a number of "Stripes", or band-shaped areas that were each covered by one single sweep of the telescope, each of which is identified by a unique integer to which it is assigned. To make the information publicly available, the data were released in a series of data releases, of which Data Release 7 (DR7) was the most recent at the time that this work began. In DR7, a total of 357 million unique objects were observed and catalogued in the photometric sample, of which nearly 930,000 were galaxies for which spectra were obtained using a separate pipeline. For every galaxy in the sample, a large number (order of 10^2) of observed and derived quantities were catalogued in the DR7 database, accessible online.

Of particular interest for our work is SDSS Stripe 82, located in the Legacy footprint area. This Stripe covers an area along the celestial equator (not to be confused with the Galactic equator) with a Right Ascension (RA) of -50° < RA < 60°, and a Declination (Dec) of -1.3° < Dec < 1.3°, for a total of approximately 300 deg^2. Stripe 82 holds ∼4.4 million photometric galaxies, with 101978 entries in the Simard et al. sample (see next section), and ∼20,000 spectroscopic galaxies; what makes it unique is that it is also the site of the SDSS II supernova survey, the details of which are explained in a separate section below. The observations of galaxies in this Stripe comprise what is used for the work discussed in this paper.

2.2 Morphological Parameters of Galaxies in the SDSS

To investigate the morphological properties of the SDSS photometric galaxies, Simard et al. 2011 took a sample of 1.12 million galaxies and created a catalogue of bulge + disk decompositions for them. Their selection criteria and methods are as follows.

In order to decompose galaxy photometry into bulge + disk components, it is necessary for the galaxies in question to be reasonably bright. Therefore, Simard et al. take galaxies with $14 \leq m_{petro,r,corr} \leq 18$, where $m_{petro,r,corr}$ is galactic-extinction-corrected r band Petrosian magnitude. The Petrosian magnitude is defined as the apparent magnitude of the integrated light within N_P Petrosian radii of the galactic centre, where $N_P = 2$ in this case. The Petrosian radius is in turn defined as the radius r at which the local surface brightness at r is a certain fraction R_{lim} of the average surface brightness within r, where $R_{lim} = 0.2$ in this case.

Having obtained the sample images, the authors proceed with 3 steps: the first is to determine the sky level around the galaxies, which can be done with either SDSS sky levels or GIM2D (Simard et al. 2002) sky level determination, the second is to deblend the galaxies from the background, which can be done with either SDSS deblending or SExtractor (Bertin & Arnouts 1996) deblending, and the final bulge + disk fits, which can be done either individually or simultaneously. To test the methods for reliability, 4 sets of fits were made:

(1)SDSS sky level + SDSS deblending + individual fitting,

(2)GIM2D sky level + SDSS deblending + individual fitting,

(3)GIM2D sky level + SDSS deblending + simultaneous fitting,

(4)GIM2D sky level + SExtractor deblending + simultaneous fitting,

and the results were examined with 3 quality assessment metrics, the details of which can be found in Simard et al. (2011). The last method is the one deemed most reliable, and the authors proceed to make the bulge + disk decompositions with it. Corrections for seeing effects and instrument PSFs (which are typically are degenerate with one another) were also applied using GIM2D.

When fitting bulge + disk components, Simard et al. assumed Sérsic profiles (see Chapter 1 for details). The disks were assumed to have an exponential profile (i.e. Sérsic index n=1). The bulges were more problematic, since not every bulge follows a de Vaucouleurs profile. Thus, for every galaxy, two separate fits were made: one with a de Vaucouleurs bulge profile, another with a bulge profile in which the Sérsic index

is free and determined by the fits. We use the data from the latter, largely due to the necessity of obtaining bulge profiles as precise as possible when comparing such profiles to Type Ia supernova spatial distributions. Indeed, the authors show that a free Sérsic index is necessary for a robust fit via an F test - see Simard et al. (2011) for details.

Of the 351 matches we find between SNe and their photometric hosts (see Section 2.6), a number of the hosts were also previously investigated by Simard et al. (2011), resulting in decomposed bulge + disk profiles, which we compare to the SNe positions within their respective hosts in Chapter 5.

2.3 Mass & Star Formation Rate Measurements from the SDSS DR7 MPA/JHU Value-Added Catalogue

The SDSS DR7 MPA/JHU value-added catalogue contains derived masses and SFR values for the spectroscopic galaxies, which we use extensively for our study. This subsection provides a brief account of how they were obtained.

Masses have historically been obtained either through rotation curves or by multiplying the luminosity with an assumed mass-to-light ratio. While both methods have their own merits and limitations, we will concentrate on the latter for the purposes of this section. The primary concern of estimating total mass via a mass-to-light ratio is that the ratio itself varies among galaxies with different star formation histories. As a result, using a mass-to-light ratio averaged over a large population of galaxies can lead to significant biases. Kauffmann et al. (2003) addressed the issue, pointing out that $D_n(4000)$ (the ratio between the average flux density between 3850-3950$\mathring{A}$ and 4000-4100$\mathring{A}$, a measure of the 4000$\mathring{A}$ break) and the $H\delta_A$ index (a measure of the $H\delta$ absorption lines) are reliable indicators of star formation history. According to their methodology, the mass-to-light ratio can be gauged by creating models which match the observed $D_n(4000)$ and $H\delta_A$ values of the galaxy in question, and making predictions about the mass-to-light ratio using the model. To make this match, they create a library of star formation histories using Monte Carlo methods, by the following methods. Galaxies are assumed to have a continuous star formation rate which exponentially decays as a function of time. Upon this background of star formation, random bursts of star formation were added, with randomized amplitudes.

The metallicities are distributed uniformly between $0.25Z_{\odot}$ to $2Z_{\odot}$.

The mass estimates for the MPA/JHU catalogue follows a similar philosophy, as explained below. For the MPA/JHU value-added catalogue, photometric masses were derived in a manner similar, though not identical, to that of Sullivan et al. (2006). The theoretical photometry of a grid of models (similar to the afore mentioned library of star formation histories) spanning the Monte Carlo library of star formation histories was calculated using software previously developed for the purpose of computing spectral evolution, in this case Bruzual & Charlot (2003). Each model was compared with the attenuation-corrected five-band photometry observations for the galaxy; a probability of each model in question matching the observational data was calculated, using the photometry. The models were then weighted by probability, binned by mass-to-light ratio and plotted as a histogram, resulting in a probability distribution function for the ratios. The median values of the probability distribution functions were then taken for galaxy mass-to-light ratios, which were finally multiplied by the total luminosities obtained by photometry to obtain mass. This is slightly different from the approach of Kauffmann et al. (2003), which matches $D_n(4000)$ and $H\delta_A$, but it has been shown that the mass estimates of the two methods do not differ by more than ~ 0.1 orders of magnitude (see http://www.mpa-garching.mpg.de/SDSS/DR7/mass_comp.html for details). This is also different from Sullivan et al. (2006) in the sense that a more advanced spectral evolution code was used (Sullivan et al. 2006 used PEGASE), but is identical otherwise.

Obtaining SFR measurements is a more complicated matter. The basic methods used were similar to those proposed by Brinchmann et al. (2004), with minor modifications.

H_{α} emission has been shown to correlate strongly with SFR (e.g., Kennicutt 1998) once a fixed IMF is assumed, but in many cases it is hard to obtain the intrinsic SFR-induced H_{α}, since dust attenuation and contaminants such as AGN can easily bias measurements, and the H_{α} lines themselves are frequently dominated by the noise in low S/N cases. To make the SFR measurements more reliable, the galaxies were divided into three different classes: (1) the "SF" class, comprised of galaxies which have a significant amount of ongoing star formation, have a very large S/N ratio, and have negligible AGN contribution to the spectra, (2) the "low S/N SF" class, which encompasses all galaxies which have very low star formation, have spectra with S/N<3 for any of 5 line spectra (H_{α}, H_{β}, O III, N II and S II), but have no AGN associated, and (3) the "AGN, Composite and Unclassifiable" class, which contains

all galaxies which are suspected to suffer from AGN contamination in the spectra, which they distinguish by checking for an excess in N II/H_α and O III/H_β above the upper limit of a pure starburst model (Kewley et al. 2001).

The "SF" class is assumed to have H_α affected only by galactic dust attenuation. Assuming that there is an abundance of neutral hydrogen within a galaxy (such that it is optically thick), Lyman series emission lines are easily re-absorbed, causing the Balmer series to be the dominant emission feature aside from Lyman α. This process is called Case B recombination. When this process is dominant, the ratio the H_α emission to H_β emission from the galaxy is fixed. This is opposed to Case A recombination, when the dust is optically thin, in which case it H_α/H_β is fixed at another different value. Assuming a Case B recombination ratio for all galaxies (which gives the H_α/H_β ratio of emission from the galaxy) and $R_V = 3.1$ (which is a good approximation for dust within galaxies, and also gives the ratio by which H_α and H_β emission is absorbed by dust), the dust attenuation can be estimated by taking H_α and H_β emission lines from the spectra and calculating H_α/H_β. After correcting for this attenuation effect, the resultant H_α and the other four lines were then compared with a model grid of 2×10^5 models simulated using the code by Charlot & Longhetti (2001). When fitting the models, all 5 emission lines are taken into account (H_α, H_β, O III, N II and S II), and a probability of the model being feasible was obtained for each model individually. The models were then processed in a similar fashion as for the stellar mass estimates as explained above, resulting in a histogram of SFRs which takes the form of a probability distribution function. Again, the median value is taken as the SFR measurement for a given galaxy.

For the "low S/N SF" class, the method explained above becomes less reliable, since with lower S/N, the resultant SFR probability distribution functions tend to be double peaked, non-symmetric or flat. This is primarily due to the problem that spectral features with a lower S/N are less reliable, and the program is consequently unable to find a prominent match with a group of galaxies with consistent SFR. To address this problem, and obtain SFR measurements for this galaxy class, the MPA/JHU group obtained a conversion factor between attenuation-corrected H_α luminosity and SFR:

$$\eta^0_{H_\alpha} = L_{H_\alpha}/SFR, \tag{2.1}$$

where $\eta^0_{H_\alpha}$ is the conversion factor. This factor was obtained by binning the "SF" class by mass, and deriving $\eta^0_{H_\alpha}$ for each bin. To obtain corrections for the attenuation

effects for galaxies with S/N<3 for either H_α or H_β, the "SF" class was binned by mass the same way as above, and the dust attenuations for every different mass range were plotted as a histogram. The median values were taken to be the dust attenuation corrections for the respective mass ranges, and applied to the "low S/N SF" class. The ones with H_α and H_β S/N ratios of less than 3 were further processed by having each mass bin binned by H_α/H_β, with the closest bin picked for the purposes of dust attenuation.

In principle, it should be possible to subtract an AGN spectrum from the galaxy spectrum; however, this process is deemed unreliable. The "AGN, Composite and Unclassifiable" class was processed by means of an empirical relation between SFR and D4000, a parametrization of the $4000\mathring{A}$ break. The probability distribution of SFR as a function of D4000 was plotted as a contour plot, and then convolved with the likelihood distribution of D4000 of the given galaxy.

Last, but not least, for all classes, the aperture effects (resulting from the fibre size limitation, preventing the spectroscopic fibre from sampling the entire object) were removed. Brinchmann et al. (2004) proposed doing this by binning the galaxies by $(g-r)$ and $(r-i)$ colours at z=0.1, and obtaining from simulations the probability distribution function of SFR/L for each bin from the fibre spectrum. The resultant median SFR/L was then applied to the photometric light observed to be outside the fibre, and a value of SFR missed due to aperture effects was inferred. However, this process was shown to overestimate the SFR of low-SFR galaxies, due to the problem that the colour dependence of SFR/L is not the same within and outside the fibre (Salim et al. 2007). Adopting similar methods to those used by Salim et al. (2007), the MPA/JHU group fitted a grid of random simulations to the five-band photometry outside the fibre, and adopt the best-fit model.

There is only one major problem in the MPA/JHU database as a result of obtaining SFRs using the methods above. The methods cannot distinguish between passive galaxies (i.e. those which have practically no SFR whatsoever) and galaxies which merely have a small SFR ($\log[SFR/(M_\odot/yr)]\sim -1$). This is due to the median SFR/L always being of some significant value. This can be seen in Figure 2.1, where all MPA/JHU spectroscopic galaxies are plotted on a mass-SFR plane. It is demonstrated in Chapter 6 that this does not significantly affect our results.

In total, we use a subset of 19987 elements taken from the SDSS DR7 MPA/JHU value-added catalogue for our spectroscopic sample. Our selection criteria within the MPA/JHU catalogue are that any entry must be a science primary, extended source

(and, therefore, a galaxy) which falls within Stripe 82, and must have a redshift of < 0.25 to be included in our sample, for reasons explained in Chapter 3.

2.4 The VESPA Database and Mass & Star Formation Rate comparisons with MPA/JHU data

The VESPA catalogue of SDSS spectroscopic galaxy properties (Tojeiro et al. 2009) gives the masses and SFRs of a total of nearly 800,000 galaxies, a great majority of which are also catalogued in the MPA/JHU sample. To test the reliability of the masses and SFRs of the MPA/JHU sample, we compare them with the corresponding entries in the VESPA sample, which were derived differently. The following is a brief introduction of how VESPA obtains masses and SFRs.

For a single stellar population, with a known initial mass function (number density of stars as a function of mass when they are first formed, abbreviated IMF), the evolution of the light emitted from the population can be calculated by applying well-known mass-dependent isochrones and corresponding spectral libraries. Thus, given the spectra from a galaxy, recovering the star formation histories from the galaxy in question is equivalent to the following analytical problem:

$$F_\lambda = \int_0^t f_{dust}(\tau_\lambda, t) SFR(t) S_\lambda(t, Z) dt, \tag{2.2}$$

where F_λ is the flux observed from the galaxy at a certain wavelength, f_{dust} is a dust correction term, Z is the stellar metallicity of the population involved, and $S_\lambda = (\frac{L}{M})_\lambda$. For the dust correction term, a one-parameter dust model based on the mixed slab model (Charlot and Fall, 2000) for small optical depths and uniform screening for large optical depths is applied:

$$f_{dust}(\tau_\lambda) = \frac{1}{2\tau_\lambda}[1 + (\tau_\lambda - 1)\exp(-\tau_\lambda) - \tau_\lambda^2 E_1(\tau_\lambda)], \quad \tau_{5500\mathring{A}} \leq 1 \tag{2.3}$$

$$f_{dust}(\tau_\lambda) = \exp(-\tau_\lambda), \quad \tau_{5500\mathring{A}} > 1. \tag{2.4}$$

To find the star formation histories in a galaxy, VESPA assumes that stars form in a number of age bins, in each of which is inserted a stellar population conforming to a fixed IMF. Each bin is traced using the models adopted by Bruzual and Charlot (2003), and the resulting spectra recovered. This is done for a grid of points in

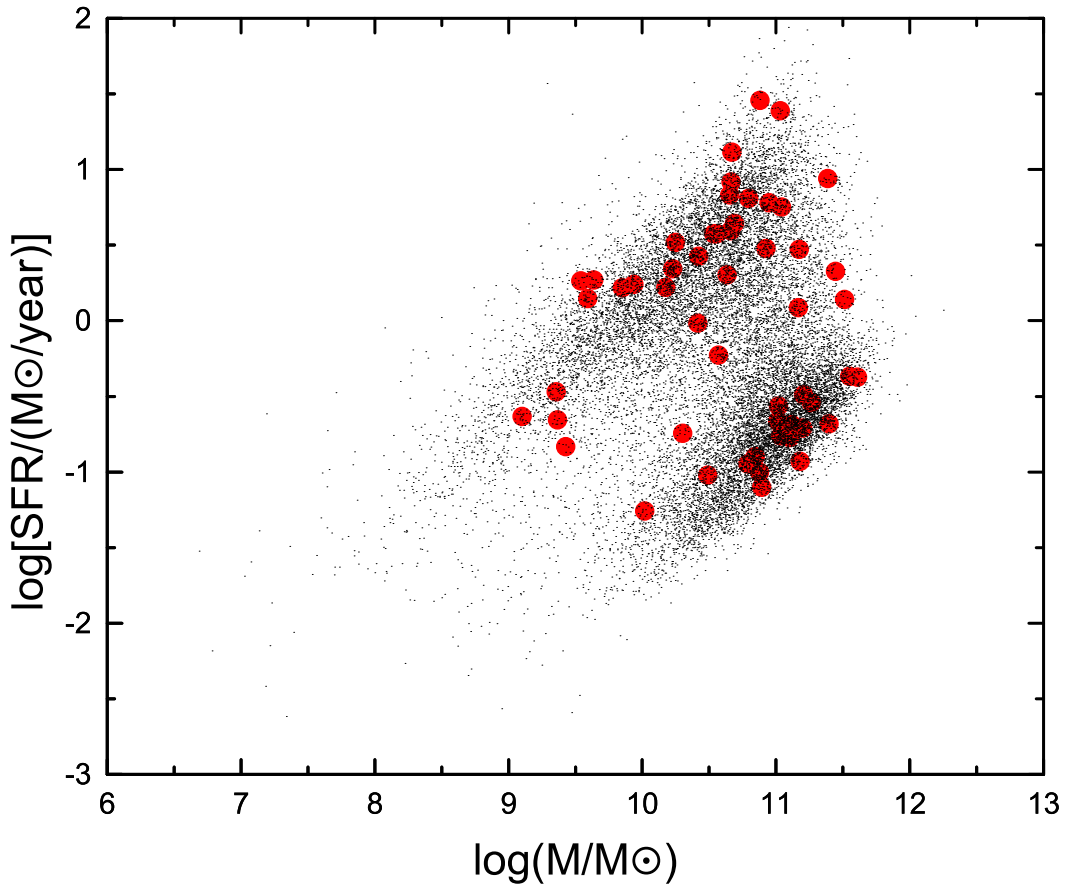

Figure 2.1: Distrbution of spectroscopic galaxies in the MPA/JHU catalogue (black dots), with the 53 hosted SNe (filled red circles) on a $\log(M/M_{\odot})$ - $\log(SFR/(M_{\odot}\mathrm{yr}^{-1}))$ plane.

parameter phase space, and for every point, a quantity χ^2 is calculated:

$$\chi^2 = \frac{\Sigma_j (F_j^{obs} - F_j^{mod})}{\sigma_j^2}, \tag{2.5}$$

where j is the corresponding wavelength bin, *obs* and *mod* signify the observed values and the values recovered using Bruzual and Charlot 2003 respectively. Thus, the treatment is based on least squares methods.

To obtain masses for the galaxies, the total amount of star formation for each bin is summed up, and for the SFRs, the average is taken for all bins with an age < 0.11Gyrs (which should reflect the most recent star formation history), with weighting on the age duration of each bin. A comparison of these quantities with their MPA/JHU counterparts is made in Figure 2.2. We see that there is a constant 0.26 dex offset, in addition to scatters of 0.18 dex for mass and 0.48 dex for SFR (standard deviation). Since the MPA/JHU masses and SFRs were derived using different methods from their VESPA counterparts, it can be said from their apparent agreement in these plots that masses and SFRs in the both samples are reliable. We therefore find it feasible to use the MPA/JHU masses and SFRs in our studies.

2.5 The SDSS-II Supernova Survey, Observing Windows and Completeness

Our SN Ia data was taken from the SDSS-II Supernova Survey (http:// sdssdp62.fnal.gov / sdsssn / snlist_confirmed_updated.php). We select the complete sample of 660 supernovae, and extract from this sample 520 undisputed, spectroscopically confirmed SNe Ia, 503 of which were observed during the 3 observation seasons in 2005, 2006 and 2007. (For the rest of this paper, "SNe" refers to SNe Ia by default unless stated otherwise.) We omit the 17 SNe on the website reportedly observed in 2004, since the observation windows of these "unofficial" SNe and their completeness would be hard to gauge.

The SDSS-II Supernova Survey is a 3-year (2005-2007) survey conducted within Stripe 82 of the Sloan Digital Sky Survey (SDSS). As mentioned above, Stripe 82 covers an area of over 300 square degrees in a belt 2.5 degrees wide, centred on the celestial equator and covering an RA of -50 to 60 degrees. For each year the survey was conducted, supernova imaging was conducted once every 5 nights between 1st

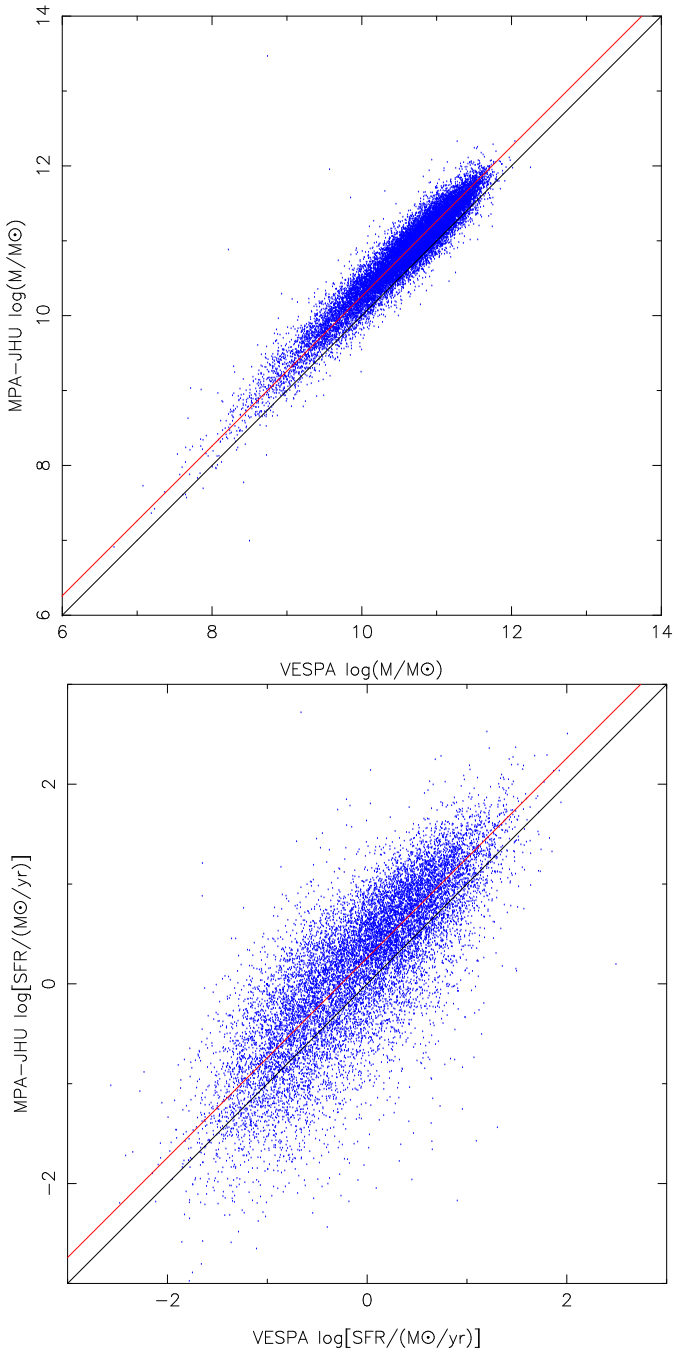

Figure 2.2: A comparison between MPA/JHU and VESPA entries for mass (top) and SFR (bottom). Note the constant 0.26 dex offset (red line), as predicted in Tojeiro et al. 2009, which is the result of a calibration offset between the VESPA and MPA databases. The scatters (standard deviation) for the masses and SFRs are 0.18 dex and 0.48 dex respectively.

September and 30th November, resulting theoretically in a total observation period of 9 months. In practice, however, the observing window is not so clear-cut: SNe which reached peak light before or after the window do occasionally to make it into the final data, with extreme elements reaching peak light $\sim$ 20 days both before and after the official observing windows. This potentially sets the upper limit of the effective length of the observing window at $\gtrsim$ 1 year.

When calculating the SN rates of a given host sample, it is necessary to take into account the completeness of the observations. We use the previous results of Dilday et al. (2008 and 2010), which obtained the SDSS-II Supernova Survey search pipeline efficiency as a function of redshift by means of Monte Carlo simulations. They use the MLCS2k2 model (see below) to generate simulated SN Ia model light curves randomly drawn from parent distributions:

Redshift: distributed such that the SN Ia rate is constant per element of comoving volume.

Host extinction A_V: drawn from a distribution $P(A_V) \propto e^{-A_V/\tau}$, with $\tau = 0.4$.

MLCS2k2 light curve shape/luminosity parameter Δ: drawn from a bimodal Gaussian with $\sigma_1 = 0.26$ for $\Delta < 0$ and $\sigma_2 = 0.12$ for $\Delta > 0$, and truncated to lie within the range of the MLCS2k2 model.

Time of peak light in rest-frame B-band: drawn randomly during the range of the "official" observing times.

Sky position: Randomly positioned within Stripe 82.

Location within host galaxy: Drawn from distribution proportional to host galaxy surface brightness.

They find a SNe detection efficiency consistently $\gtrsim$ 95% out to a redshift of 0.25, the redshift range we are concerned with. However, not all detected SNe can be identified as Ia, resulting in some SNe which peaked in early September or late November being removed from the database. This results in the removal of $\sim$ 30% of the SNe, with a lower identification rate at higher redshift. Note, however, that unlike the Dilday et al. papers, which concentrate on the redshift variance of volumetric SN rates, our results are not sensitive to any redshift variation in the detection efficiency, and this lower high-redshift identification rate will likely only result in scaling of our SN rates by some constant factor. While there are SNe which peak outside the 9 months of observation time, the detection efficiency for them is much lower (see Chapter 6 for details).

The positions of host galaxies are plotted (in red) over the entire population of

spectroscopic host galaxies on a mass-SFR plane in Figure 2.1.

For the rest of this thesis, we assume that the observation window T is precisely 9 months in length, and that the detection efficiency ϵ_t is consistently 100% within this window. The supernova identification ϵ_z efficiency is assumed to be invariant with redshift, and is assumed to be ~ 0.7. Thus, the size of the SN sample is assumed to be the intrinsic number occuring in the sky within a timeframe of $\epsilon_t \epsilon_z T \sim 0.5$years. Whether or not our assumptions above are reasonable are investigated further in Chapter 6.

2.6 Host-Matching Criteria

The problem of matching SNe Ia to host galaxies is not as simple as it may seem. Intuitively, the closest galaxy in terms of angular distance to any given SN Ia should be identified as the host, but in some cases, this may not be the correct identification. Sometimes, a multitude of hosts lie closely within the vicinity of the SN, and the closest in terms of angular distance may not be the host (see Figure 2.3, taken from Sullivan et al. 2006 for some examples).

We adopt a matching algorithm similar to that used by M. Sullivan et al. (2006). We assume that the angular distance divided by the degree of extension of galaxy light in the direction of the SN is a better indicator, and use this as our matching criteria. This is done via the following steps. First, we obtain r-band isophotal parameters of the galaxies. These are presented as the semimajor axis (r_A), semiminor axis (r_B) and position angle (ϕ) of the 25 magnitudes/arcsec^2 isophote. Next, we determine the difference in right ascension (RA) and declination (DEC) between the SNe and the prospective host galaxies, denoted as x_r and y_r respectively. Thus, for every potential redshift-matched SN - host pair, an R_{25} parameter is calculated according to the equation below:

$$R_{25}^2 = C_{xx} x_r^2 + C_{yy} y_r^2 + C_{xy} x_r y_r, \tag{2.6}$$

where $C_{xx} = \cos^2(\phi)/r_A^2 + \sin^2(\phi)/r_B^2$, $C_{yy} = \sin^2(\phi)/r_A^2 + \cos^2(\phi)/r_B^2$ and $C_{xy} = 2\sin(\phi)\cos(\phi)(1/r_A^2 - 1/r_B^2)$. Geometrically, this R_{25} is the ratio of L_{SN} to $L_{25}(SN)$, where L_{SN} is the angular length of a straight line connecting the SN to the galaxy centre, and $L_{25}(SN)$ is the angular distance between the galaxy centre and the intersection of the afore-mentioned line with the elliptical 25 magnitudes/arcsec^2 isophote (see

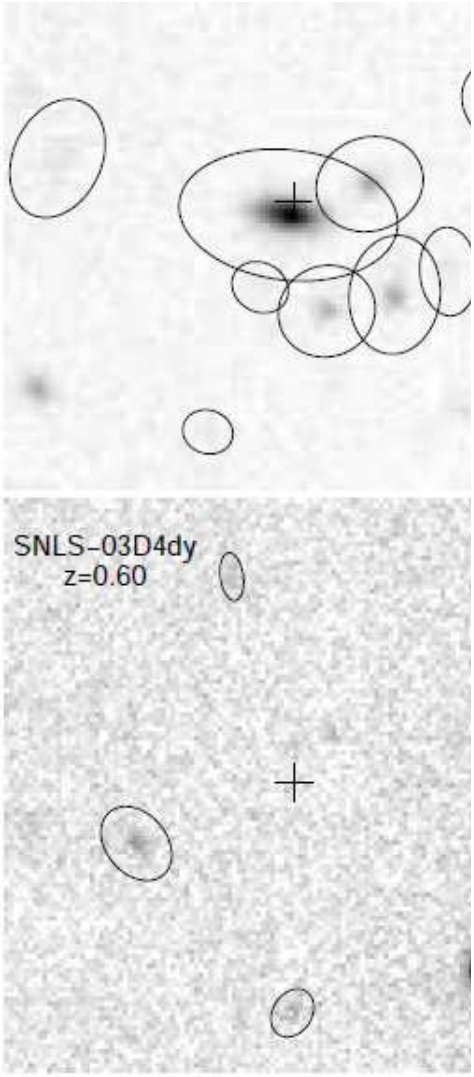

Figure 2.3: Figure illustrating problems with matching SNe to the closest galaxy in terms of angular distance. Taken from Sullivan et al. (2006).

Figure 2.4 for a more illustrative view of R_{25}). The host with a reasonable redshift possessing the lowest R_{25} value is then identified as the host candidate for the SN in question. The SNe with no host with a matching photometric redshift within 3 times the photometric redshift error are discarded. For hosts which have spectroscopic measurements of redshift, the spectroscopic redshift of the host is also compared to the SNe, though this does not eliminate any of our host candidates which passed further criteria (as stated below).

Naturally, these R_{25} values vary for every host candidate - SN Ia pair, which introduces the question of what R_{25} value could be regarded as a genuine host match for our purposes. To answer this question, an algorithm was created to generate a random table of 600 fake SNe Ia positions within the area of Stripe 82. This was processed the same way as the genuine SNe (minus redshift selection), and the R_{25} values of these fakes were obtained. Due to the randomness of their positions, it is expected that these fake SNe yield no matches to their hosts. It was concluded, after 20 runs, that only $\sim 8\%$ of these fakes attained an R_{25} smaller then 3.8. Therefore, we treat every host candidate - SN Ia pair with $R_{25} < 3.8$ as a genuine match. Applying this criterion, we find 351 matches for the SNe within the SDSS DR7 database. It may be argued that since ~ 170 SNe found no match, $\sim 8\% \times 170 \sim 14$ SNe of the 351 could be random matches too. However, we consider this number to be relatively small in comparison to the 351 matches we find, and also the additional redshift constraints explained above would help further lower the number of random matches.

This selection process eliminates the potential bias caused by any deviation of galaxy geometry from being perfectly circular, as opposed to the intuitive angular distance method.

2.7 Tests for Host-Matching

To test our host-matching procedure, we use 3 separate methods, each of which tests a necessary condition of the matching process being correct.

First, we visually examine the positions of a randomly chosen sample of 20 images containing SN Ia hosts. The positions of the SNe are given by a red cross, while an elliptical line shows the position of the 25 magnitudes/arcsec^2 isophote. The relative physical positions all seem reasonable. See Figure 2.5 for an example. These are then compared to the R_{25} values which are calculated by our algorithm to check for programming errors. They all look reasonable.

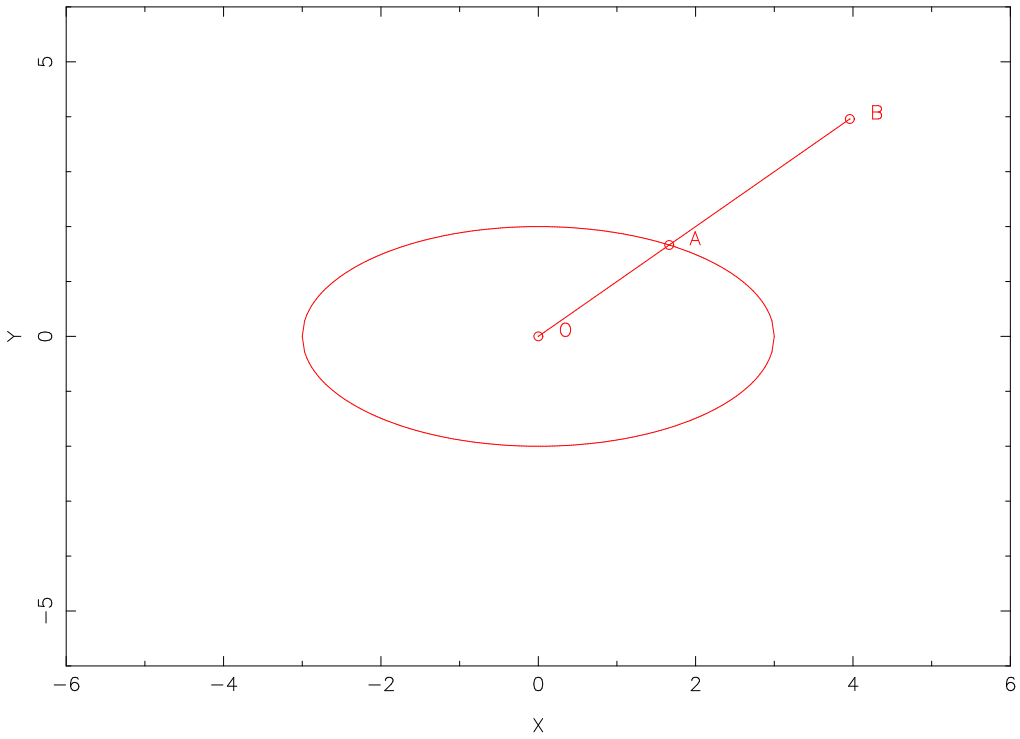

Figure 2.4: Diagram illustrating the concept of R_{25}. The ellipse is the 25 magnitudes/arcsec^2 isophote for the potential host galaxy, O is the centre, the SN Ia is at B, and A is the point of intersection between the ellipse and line OB. R_{25}=OB/OA.

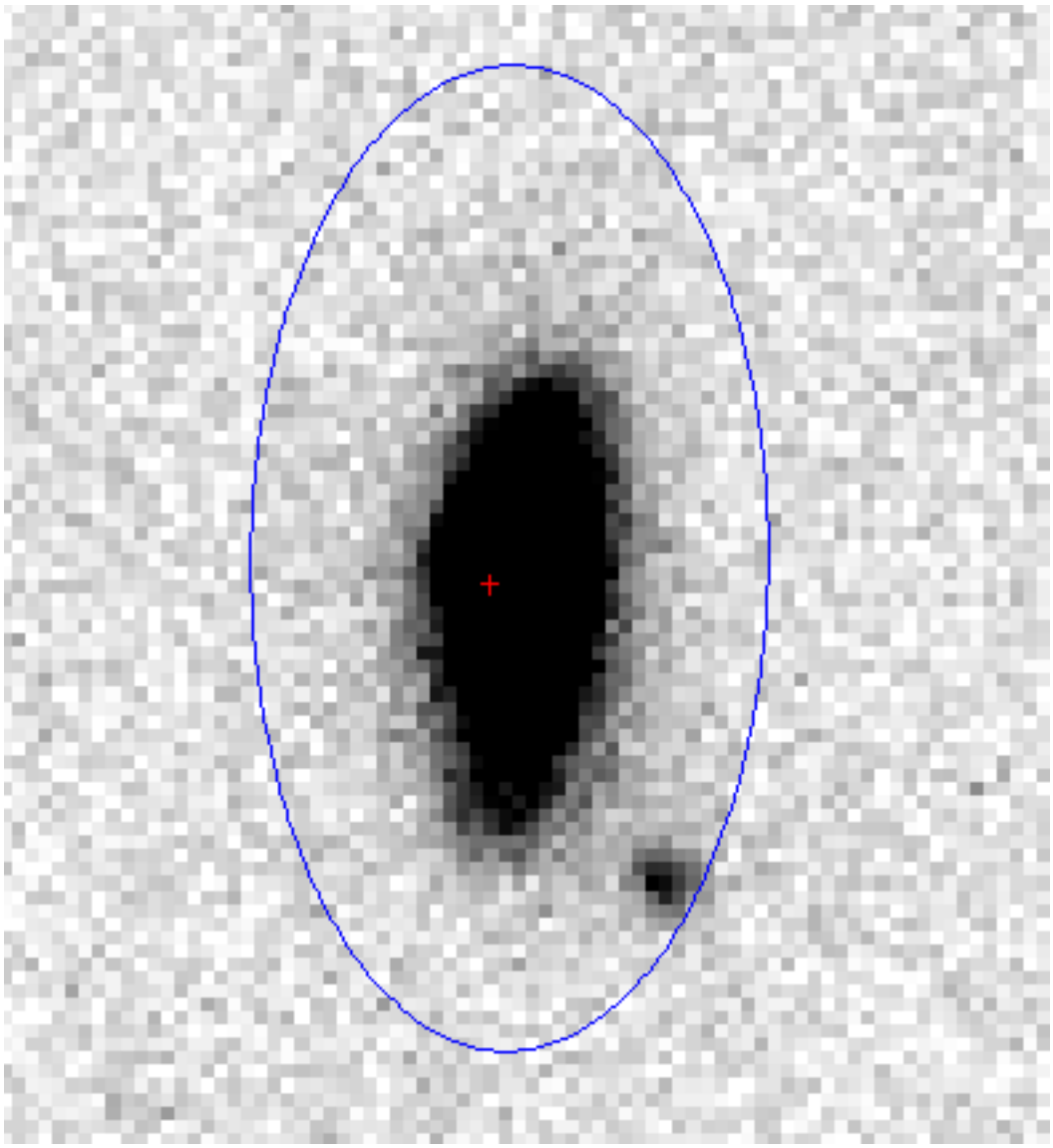

Figure 2.5: SN Ia position (the cross) and the elliptical curve corresponding to $R_{25} = 3.8$ for a $R_{25} = 0.25$ match.

Second, we inspect the complete set of images which capture the complete light curve of 3 randomly picked SNe Ia. The same tests as above were applied to every frame. In addition, this also tests the SDSS II supernova identification pipeline in the sense that the transient objects identified as SNe Ia must have a light curve duration that matches SNe Ia. The results are satisfactory.

Finally, we plot number of SN matches versus the R_{25} criterion. This plot can be seen in Figure 2.6. The vertical line is where we place our criteria, i.e. $R_{25} = 3.8$. We can see that there is a flat "plateau" region beyond $R_{25} = 3.8$, which we assume to be the regime where random matches between SNe and non-host galaxies become dominant.

In summary, we find our matches to be convincing.

We also quantitatively compare the discrepancies between our host-matching method and the "closest angular distance" (CAD) matching method used by many other authors (e.g., Smith et al. 2011). For our sample of SNe and photometric galaxies, we match the SNe with the closest host in angular distance, taking SNe with no host within 5 arcsecs to be hostless. We obtain 325 matches. Out of these, 313 SNe had the same host as our $R_{25} < 3.8$ method, R_{25} matched 36 SNe which CAD did not, and CAD matched 10 which R_{25} did not, and 2 SNe were given different hosts. Thus we conclude that there is a $\sim$10% discrepancy between the matches.

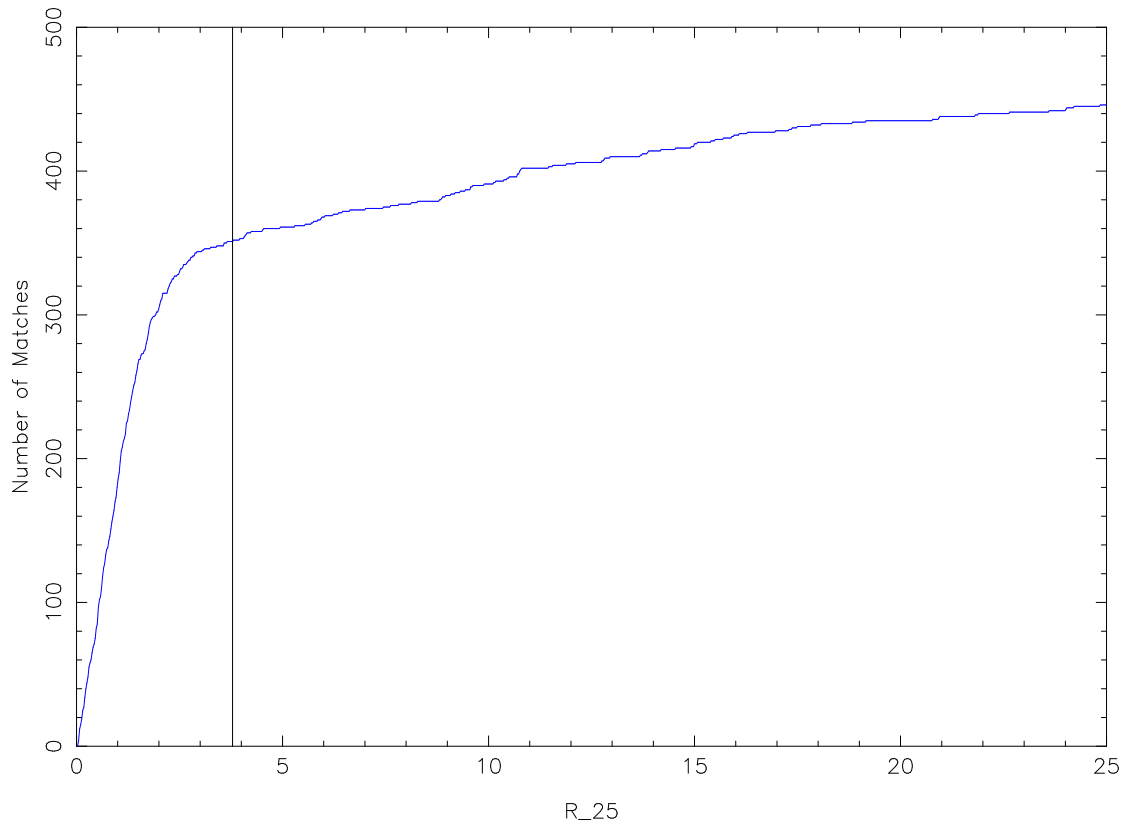

Figure 2.6: R_{25} criteria used (x-axis) plotted against number of SNe matched (y-axis). $R_{25} = 3.8$, the criterion we use, is shown by the vertical line. Note that the curve flattens out very rapidly beyond the line.

Chapter 3

A+B Fits

Having obtained our data, we proceed to calculate the A and B parameters for the $A{\cdot}M + B{\cdot}SFR$ model (commonly called the "A+B" model). In this chapter, we compare the results from two different statistical methods, and test their reliability.

To obtain the A and B parameters for the A+B model, stellar masses and star formation rates for our spectroscopic galaxy sample of 19987 spectroscopic galaxies were obtained from the MPA/JHU catalogue (see section 2.3, as well as Kauffmann et al. 2003, Brinchmann et al. 2004 and Tremonti et al. 2004 for details). The entries in the sample cover 53 of our matched hosts (see Table 3.1 for details). To obtain this sample, we selected only those objects which simultaneously meet the following criteria: "science primary" (meaning the most reliable image of a given galaxy out of a multitude of them), extended source which falls within Stripe 82, and a redshift of < 0.25. The rationale for this is that we wish to include every single galaxy in the MPA/JHU catalogue for which a hosted SN would have been observed, and also exclude any galaxies for which hosted SNe would not have been observed. The redshift cut at 0.25 was chosen because our highest-redshift SN is at z=0.23. Science primaries are used because they are identified to be the most reliable observations of their respective object spectra, and extended sources are chosen since point sources are potentially stars instead of galaxies. Selecting our sample this way negates completeness issues, since we are effectively selecting a magnitude-limited sample and taking into account all SNe hosted by that sample. This is discussed further in Chapter 6.

Table 3.1: Raw data for the 53 spectroscopic galaxies hosting SNe, as well as the positions of the hosted SNe. Note that mass and star formation rate data is available.

Host ID	log**M***	log**SFR***
587730847691047799	10.654	0.834
587730848501203452	9.427	-0.833
587731173306008275	11.118	-0.688
587731185114350067	11.011	-0.663
587731185668849933	11.034	-0.760
587731185669505187	10.557	0.575
587731186195366060	10.019	-1.259
587731186197332148	9.936	0.241
587731511537959123	9.590	0.147
587731511546806433	9.850	0.220
587731513142214757	10.489	-1.020
587731513142542420	10.414	-0.017
587731513143328955	10.845	-0.898
587731513146671215	11.395	-0.681
587731513679675512	10.226	0.345
587731513679610009	10.534	0.576
587731513693569205	11.017	-0.566
587731514222116993	11.444	0.326
587731514227818648	10.177	0.222
587731514231816228	11.104	-0.774
587731514232209584	11.175	0.471
587731172231872692	11.178	-0.930
587731172233183337	10.795	0.809
587731172767368214	10.664	0.919
587731174914786124	10.569	-0.229

Continued on Next Page...

Table 3.1 – Continued

Host ID	log**M***	log**SFR***
587731185121951943	10.669	1.115
587731185126539408	9.637	0.269
587731185129554046	11.168	0.085
587731185132568670	10.878	-1.001
587731187278872773	11.386	0.940
587731512071028897	10.892	-1.102
587731512621465722	10.421	0.426
587731513427624076	9.357	-0.470
587734305949483196	11.551	-0.368
588015507661783172	9.366	-0.655
588015507672137965	10.947	0.782
588015507677642829	11.042	0.752
588015508206518484	11.207	-0.491
588015508211368141	10.247	0.518
588015508215431379	11.033	1.390
588015510339256459	11.264	-0.541
588015510339649629	11.199	-0.711
588015510363373783	10.661	0.596
588015508735393931	11.513	0.140
588015509274427469	11.608	-0.372
588015509275869191	9.540	0.263
588015509283078244	10.635	0.303
588015509285634176	10.880	1.458
588015509292319354	9.103	-0.632
588015509293760750	10.689	0.644
588015509801599099	10.790	-0.946
588015509811626061	10.926	0.479
588015509814313038	10.302	-0.744

* M is in $M_\odot$, SFR is in $M_\odot$/yr

Even with the data obtained, the values of A and B of the $A+B$ model are by no means obvious. To recover the A and B parameters, a statistical fit must be applied to the data.

In our study, two different parametric fitting methods were investigated: the Least Squares method (which was developed by Sullivan et al. 2006), and a Maximum Likelihood method which we have developed. In essence, given a sufficiently large sample, the results of these two methods should not differ too significantly. However, with a small sample such as ours, significant complications arise when utilising the Least Squares method, which we will discuss below. We calculate A and B values for both cases, but conclude that only the Maximum Likelihood results are valid for our analysis.

3.1 Least Squares Method

In the $\log(M/M_\odot)$ - $\log(SFR/(M_\odot \mathrm{yr}^{-1}))$ plane, we bin the galaxy masses and SFRs, and also the observed SNe into 42 equally-spaced bins over the $\log(M/M_\odot)$ range of $9 \sim 12$, and the $\log(SFR/(M_\odot \mathrm{yr}^{-1}))$ range of -1.5 $\sim$ 2. Thus, for each bin, we have $x_i = M_i/M_\odot$, $y_i = SFR_i/(M_\odot \mathrm{yr}^{-1})$, and S'_i = the number of SNe Ia observed in each bin, where i is the bin number, spanning the range 1 to 42 (See Figure 2.1 for the distribution of the 53 hosted SNe on this plane, and refer to Table 3.1 for the raw data).

Applying the original $A+B$ model from Sullivan et al. (2006) to our grid, we have

$$S_i = A \cdot M_i + B \cdot SFR_i, \tag{3.1}$$

where S_i is the theoretical number of SNR that should be seen in that particular grid. According to the definition of the least-squares method, $\Sigma(S_i - S'_i)^2$ must be minimised, where S'_i is the observed number of SNe in the grid; therefore

$$\frac{\partial}{\partial A}\Sigma(S_i - S'_i)^2 = 0, \tag{3.2}$$

$$\frac{\partial}{\partial B}\Sigma(S_i - S'_i)^2 = 0. \tag{3.3}$$

This leads to

$$A[\Sigma(M_i^2)] + B[\Sigma(M_i{\cdot}SFR_i)] - [\Sigma(S_i'{\cdot}M_i)] = 0, \tag{3.4}$$

$$A[\Sigma(M_i{\cdot}SFR_i)] + B[\Sigma(SFR_i^2)] - [\Sigma(S_i'{\cdot}SFR_i)] = 0. \tag{3.5}$$

So A and B can be expressed as

$$A = \frac{\begin{vmatrix} \Sigma(S_i'{\cdot}M_i) & \Sigma(M_i{\cdot}SFR_i) \\ \Sigma(S_i'{\cdot}SFR_i) & \Sigma(SFR_i^2) \end{vmatrix}}{\begin{vmatrix} \Sigma(M_i^2) & \Sigma(M_i{\cdot}SFR_i) \\ \Sigma(M_i{\cdot}SFR_i) & \Sigma(SFR_i^2) \end{vmatrix}} \quad , \tag{3.6}$$

$$B = \frac{\begin{vmatrix} \Sigma(M_i^2) & \Sigma(S_i'{\cdot}M_i) \\ \Sigma(M_i{\cdot}SFR_i) & \Sigma(S_i'{\cdot}SFR_i) \end{vmatrix}}{\begin{vmatrix} \Sigma(M_i^2) & \Sigma(M_i{\cdot}SFR_i) \\ \Sigma(M_i{\cdot}SFR_i) & \Sigma(SFR_i^2) \end{vmatrix}} \quad . \tag{3.7}$$

Substituting the values of M_i, SFR_i, and S_i', we obtain the values $A = 3.5^{+0.3}_{-0.5} \times 10^{-14}/M_\odot$ and $B = 1.1{\pm}0.2 \times 10^{-3}/M_\odot \mathrm{yr}^{-1}$, with the error bars found by assuming a Gaussian distribution of errors for the SNR,

$$P(A,B) = \exp[-\frac{1}{2}(S_i - S_i'(A,B))^2], \tag{3.8}$$

and writing

$$\ln P((A,B)|\{S_i', M_i, SFR_i\}) = -\frac{1}{2}\Sigma(S_i' - M_i - SFR_i)^2, (\text{i=1 to 42}), \tag{3.9}$$

where $P((A,B)|\{S_i', M_i, SFR_i\})$ is the probability of a given set of (A,B) matching the data. This was done for consistency with the way by which we derive error bars for the maximum likelihood method (see Section 3.2). This is a tried-and-tested method (e.g., Brinchmann et al. 2004).

Note that we did not weight the galaxies nor the SNe for accessible volume. The galaxy sample is the result of a magnitude limited survey within the redshift of the farthest SN, and hence the hosted SN sample for these galaxies is complete. Our host matching methods (see Chapter 2) eliminates SNe which are not hosted by these galaxies, which nullifies contamination. Due to this interpretation of our samples, we

do not apply selection function weighting to either of them. This is further explained in the Chapter 6.

In our analysis above, we used the "generic" Least-Squares method, i.e. assumed that the number of SNe observed in each bin intrinsically reflects the SN rate in that bin. In reality, with a finite number of SNe, the number of SNe observed in each bin follows a Poisson distribution, with the mean value μ corresponding to the number that reflects the intrinsic SN rate. To correct for this uncertainty, the standard method is to weight each bin by $1/\sigma^2$, where σ is the standard deviation in the Poisson distribution mentioned earlier in this paragraph. For a Poisson distribution, $\mu = \sigma^2$, and the best estimate that could be made for μ happens to be $\mu = S'_i$. However, for about half of the grids, $S'_i = 0$, rendering this treatment a technical impossibility. Nevertheless, we experiment by discarding all grids yielding no SNe, and thereby apply the above correction:

$$\ln P((A,B)|\{S'_i, M_i, SFR_i\}) = -\frac{1}{2}\Sigma\frac{(S'_i - M_i - SFR_i)^2}{S'_i}, \text{(i=1 to 42)}. \tag{3.10}$$

Ironically, this yields A and B parameter values ($A = 1.9^{+0.7}_{-0.6} \times 10^{-14}/M_\odot$ and $B = 0.83^{+0.32}_{-0.28} \times 10^{-3}/M_\odot \mathrm{yr}^{-1}$) even more erroneous than those obtained via the generic least-squares treatment (compare with results in Section 3.2). The rates are even smaller than our generic least-squares fits, so the discrepancy cannot be explained by the fact that we discarded grids with no SNe prior to the fits. Our interpretation for this is that, for relatively small samples, Least-Squares is not as robust a fitting algorithm as Maximum likelihood. Therefore, we only use the Least-Squares method for comparison with Sullivan et al. (2006), who used the same method, while relying on the Maximum Likelihood method for our scientific goals.

3.2 Maximum Likelihood Method

As explained in the last subsection, for smaller data sets, the Maximum Likelihood method yields better estimates for the parameters. For every set of A and B, and every one of the spectroscopic galaxies falling within Stripe 82, a probability is calculated that its SN-hosting status is as observed, given a hypothesised SNR. The probabilities for all the galaxies are then multiplied for every set of A and B, and the set with the highest product is the one we take to be the calculated values. Thus, in theory, we

maximise

$$L = (\Pi P(S_i|\overline{SN}))(\Pi P(S_j|SN)), \tag{3.11}$$

where i is the number of galaxies without SNe, and j is the number of galaxies hosting them (which happens to be 53 in this case). In practice, to save calculation time, we take the logarithm of L and maximise that instead:

$$\ln L = \Sigma \ln P(S_i|\overline{SN}) + \Sigma \ln P(S_j|SN). \tag{3.12}$$

For $P(S_i|\overline{SN})$ and $P(S_j|SN)$, two different formulations were used.

Since the intrinsic Poisson distribution values for these two expressions are

$$P(S_i|\overline{SN}) = \frac{\lambda^k e^{-\lambda}}{k!} = e^{-S_i}, \tag{3.13}$$

$$P(S_j|SN) = \frac{\lambda^k e^{-\lambda}}{k!} = S_j e^{-S_j}, \tag{3.14}$$

then

$$\ln L = \sum_i (-S_i) + \sum_j (lnS_j - S_j), \tag{3.15}$$

or, in other words,

$$\ln L = -\sum_{n=1}^{19987} S_n + \sum_{m=1}^{53} (lnS_m). \tag{3.16}$$

This is our final formulation. We perform a 500×500 grid search on $\log[A(M_\odot)]$ from -14.2 to -12.2, $\log[B(M_\odot \mathrm{yr}^{-1})]$ from -4.2 to -2.2. We find the maximum likelihood A and B values to be $A = 3.5^{+0.9}_{-0.7} \times 10^{-14}(M_\odot)^{-1}$ and $B = 1.3^{+0.4}_{-0.3} \times 10^{-3}(M_\odot \mathrm{yr}^{-1})^{-1}$ respectively. To check that we have searched the correct regimes in our grid search, we conduct another grid search, this time from -18.5 to -10.5 for $\log[A(M_\odot)]$, -8.5 to -0.5 for $\log[B(M_\odot \mathrm{yr}^{-1})]$, with consistent results. Figure 3.1 plots the probability contours and error bars for our grid search, while Figure 3.2 compares these results with the observed SNR at different specific SFR.

To make sure that this approach could reliably extract A and B values from the data, we conducted a set of Monte Carlo simulations as follows. We assume $A = 4 \times 10^{-14}(M_\odot)^{-1}$ and $B = 2 \times 10^{-3}(M_\odot \mathrm{yr}^{-1})^{-1}$, and, using a pseudorandom

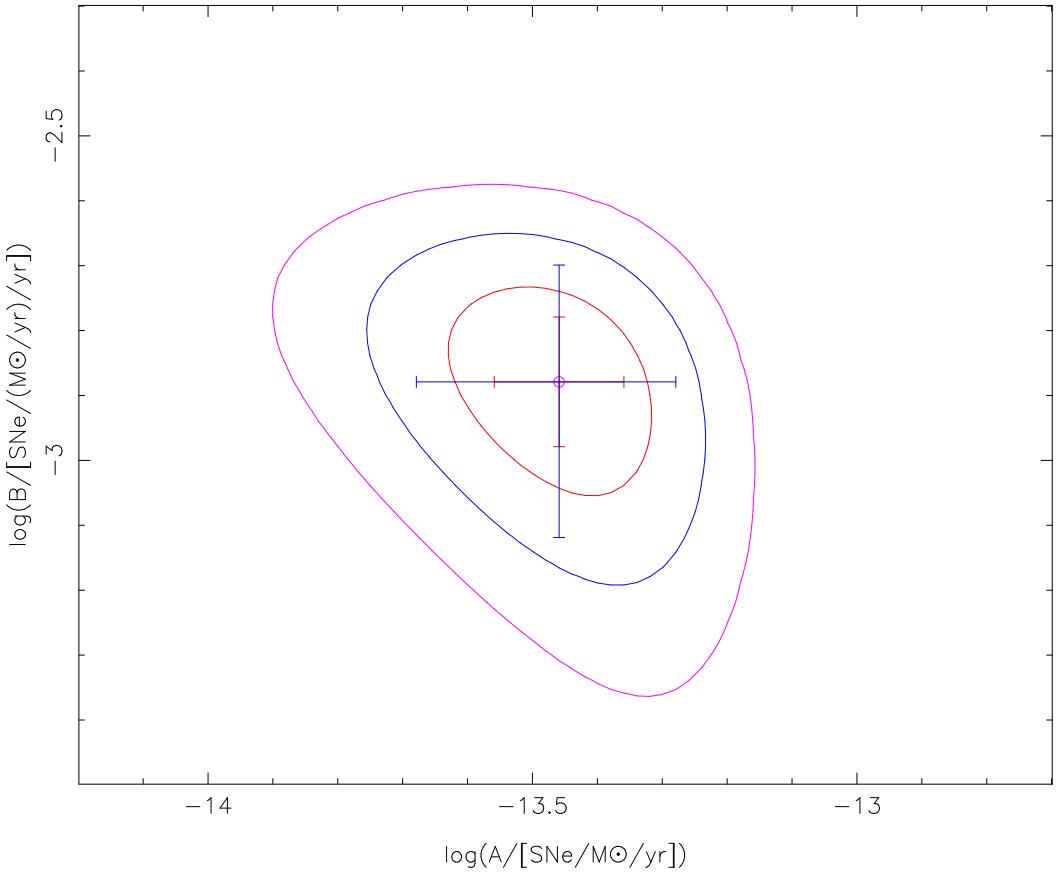

Figure 3.1: Probability contours for the values of A and B in phase space. The red, blue and pink contours represent 1-σ, 2-σ, 3-σ probability respectively, while the circle denotes our final maximum likelihood value. The error bars show the 1- and 2-σ limits of the marginalised distributions of A and B.

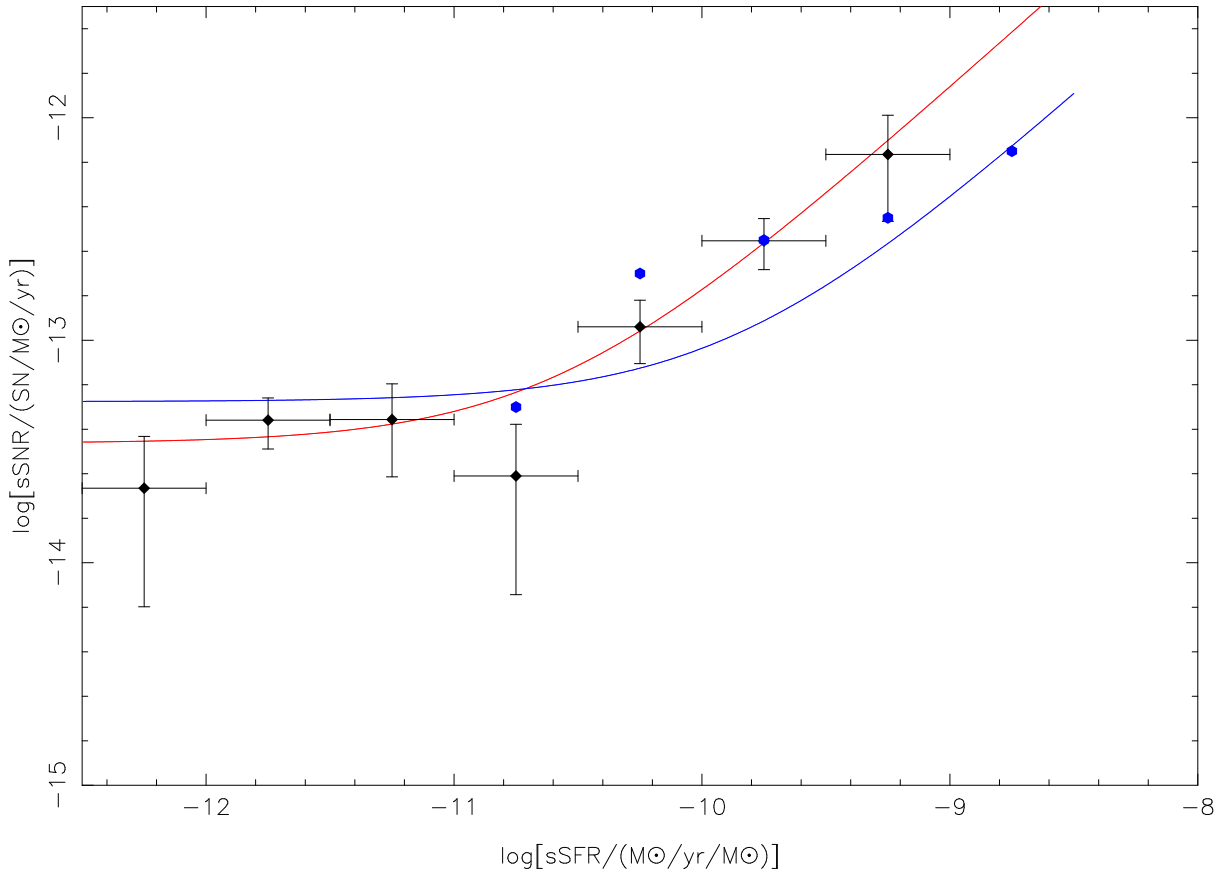

Figure 3.2: Specific supernova rate as a function of specific star formation rate. The black diamond points are for our observed sample. Plotted for comparison are the predictions of our best-fit A+B model (red line), the predictions of Sullivan et al. 2006 (blue line), and their data (blue hexagons).

Table 3.2: Comparison of A,B Values with Previous Studies. The meaning of the abbreviations are as follows: SB05 = Scannapieco & Bildsten (2005), N06 = Neill et al. (2006), D08 = Dilday et al. (2008), S06 = Sullivan et al. (2006), Sm11 = Smith et al. (2011). It can be seen that our results agree within error bars with most of the literature, with the only significant disagreement being the B value for S06.

Paper	$A{\cdot}(10^{14}/M_{\odot}^{-1})$	$B{\cdot}(10^{3}/(M_{\odot}^{-1}{\cdot}\mathrm{yr}))$
This work	$3.5^{+0.9}_{-0.7}$	$1.3^{+0.4}_{-0.3}$
SB05	$4.4^{+1.6}_{-1.4}$	$1.2^{+0.7}_{-0.6}$
N06	1.4 ± 1.0	0.8 ± 0.26
D08	2.8 ± 1.2	$0.93^{+0.34}_{-0.31}$
S06	5.3 ± 1.1	0.39 ± 0.07
Sm11	$2.8^{+0.6}_{-0.5}$	$1.4^{+0.2}_{-0.1}$

number generator, seed SNe into our spectroscopic sample according to the A and B values we assume. Then, using our generated fake data, we use the Maximum Likelihood method to recover A and B. The recovered values ($A(M_{\odot}) = 4.2\pm0.6 \times 10^{-14}$ and $B(M_{\odot}\mathrm{yr}^{-1}) = 1.9\pm0.3 \times 10^{-3}$, the errors being best-estimate sample standard deviations from 10 runs) were consistent with our assumptions ($A(M_{\odot}) = 4 \times 10^{-14}$ and $B(M_{\odot}\mathrm{yr}^{-1}) = 2 \times 10^{-3}$). See Figure 3.3 for a stack of 10 runs of our Monte Carlo simulations.

Our maximum likelihood results agree very well with our generic least-squares ones, indicating that our sample is sufficiently large. The slight discrepancy could be due to two factors. The first is that, in our least-squares binning procedure, we could have missed a minority of galaxies which fell out of the 42 grids. The second is that the least-squares binning procedure results in poisson noise of SNR in each grid, as explained in the last section.

Our final results ($A = 3.5^{+0.9}_{-0.7} \times 10^{-14}/M_{\odot}$ and $B = 1.3^{+0.4}_{-0.3} \times 10^{-3}/M_{\odot}\mathrm{yr}^{-1}$) are consistent within error bars with most of the literature, with the exception of Sullivan et al. (2006). The discrepancy is possibly due to the authors of Sullivan et al. (2006) making accessible volume corrections to their data. This is discussed further in Chapter 6. For a summary/comparison of these results, see Table 3.2.

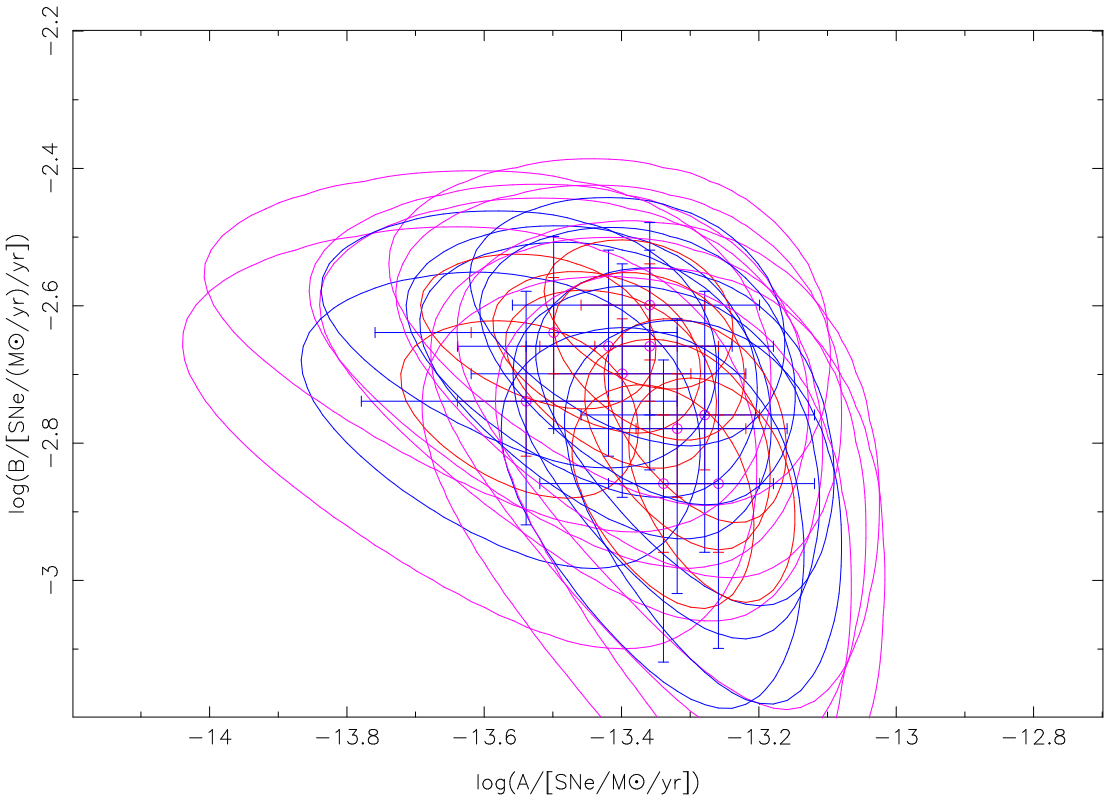

Figure 3.3: A stack of probability contours and error bars corresponding to those in Figure 3.1 for 10 Monte Carlo simulations using artificially inserted SNe.

Chapter 4

Anomaly in SNR: Deviation from the standard A+B Model

So far, we have applied two statistical fitting methods to our data to obtain the values of A and B from the A+B model. We find the maximum likelihood method to be the more reliable of the two for our relatively small data sample. From the fits using the maximum likelihood method, we have obtained values of $A = 3.5^{+0.9}_{-0.7} \times 10^{-14}(M_{\odot})^{-1}$ and $B = 1.3^{+0.4}_{-0.3} \times 10^{-3}(M_{\odot}\mathrm{yr}^{-1})^{-1}$. However, the fact that we have obtained best-fit values for the A and B parameters does not necessarily mean that the model fits the data well. To be able to tell whether or not an A+B model with our derived values for A and B matches the data, a quantitative approach is required.

In this Chapter, we test whether the A+B model explains our data well. It is shown that not only does an A+B model with our best-fit parameters fail to match the data, no A+B model with any set of A and B could match our data. We proceed to investigate a series of alternate models, and constrain them using the same tests. We also consider the SNR model proposed by Smith et al. (2011).

4.1 Rejection of the A+B Model

As a test of the A+B model's consistency, we rank the spectroscopic galaxy sample of 19987 galaxies by mass, from least massive to most massive, calculate the cumulative percentage distribution of SNR for both the A+B model and the observations, and apply a K-S test to the two distributions. This procedure will henceforth be called the mass-ranked K-S test. If the "A+B" model intrinsically reflects the SNR of any

Table 4.1: "Colour Code" refers to the colours used to plot the cumulative distribution functions in the figures of this paper. "$1-\alpha_X$" is the degree of rejection from a K-S test in which the galaxies are ranked by "X". Passing all three tests is a necessary but not sufficient condition for a model to be considered plausible.

Model	Colour Code	$(1-\alpha_M)$	$(1-\alpha_{sSFR})$	$(1-\alpha_{SFR})$
$AM+BSFR$	green	99%	97%	<1%
$AM+BSFR+CM^2$	cyan	>99%	93%	2%
$AM+BSFR+CM^{-1}$	purple	93%	72%	7%
$AM+BSFR+C$	orange	2%	34%	22%
AM only	yellow	>99%	>99%	>99%
$(AM+BSFR)(1+CM^{-1})$	red	2%	80%	26%
constant rate	black	25%	96%	62%
$BSFR$ only	blue	53%	>99%	>99%
$AM+BSFR+CM^{-1/2}$	pink	27%	29%	1%

given galaxy, the KS test should not yield a rejection. To our surprise, the A+B model with our derived values for A and B was rejected at the 99% confidence level (see Figure 4.1). To investigate the possibility that other A and B values could have passed the test, we plot the cumulative distribution functions of our galaxies for both an A-only model (SNR=AM) and a B-only model (SNR=B·SFR), keeping in mind that any set of values of A and B must fall within these two distributions. Note that for the A-only and B-only models, the values taken for A and B do not affect the result. The A-only model was rejected at an even higher degree, while the B-only model passed the test ($\sim$ 50% rejection). This shows that our data do not support a larger value of A/B. The models with a smaller value of A/B are not rejected by this test, but we will proceed to reject them in the next few paragraphs.

Passing the mass-ranked K-S test is a necessary but insufficient condition of an SNR model being plausible. If the A+B model is indeed consistent with the data, then the cumulative distribution of observed SNe should follow the cumulative distribution of SNR, regardless of how the host galaxies are ranked. To investigate other necessary conditions, we rank the host galaxies by sSFR and SFR, and apply the same philosophy to obtain SFR-ranked and sSFR-ranked KS tests. For the sSFR-ranked K-S tests, the A+B model passed the test, rendering it inconclusive (see Figure 4.2 for details). For the SFR-ranked ones, however, there is a significant result.

Both the generic A+B model and the B-only model were rejected by the SFR-

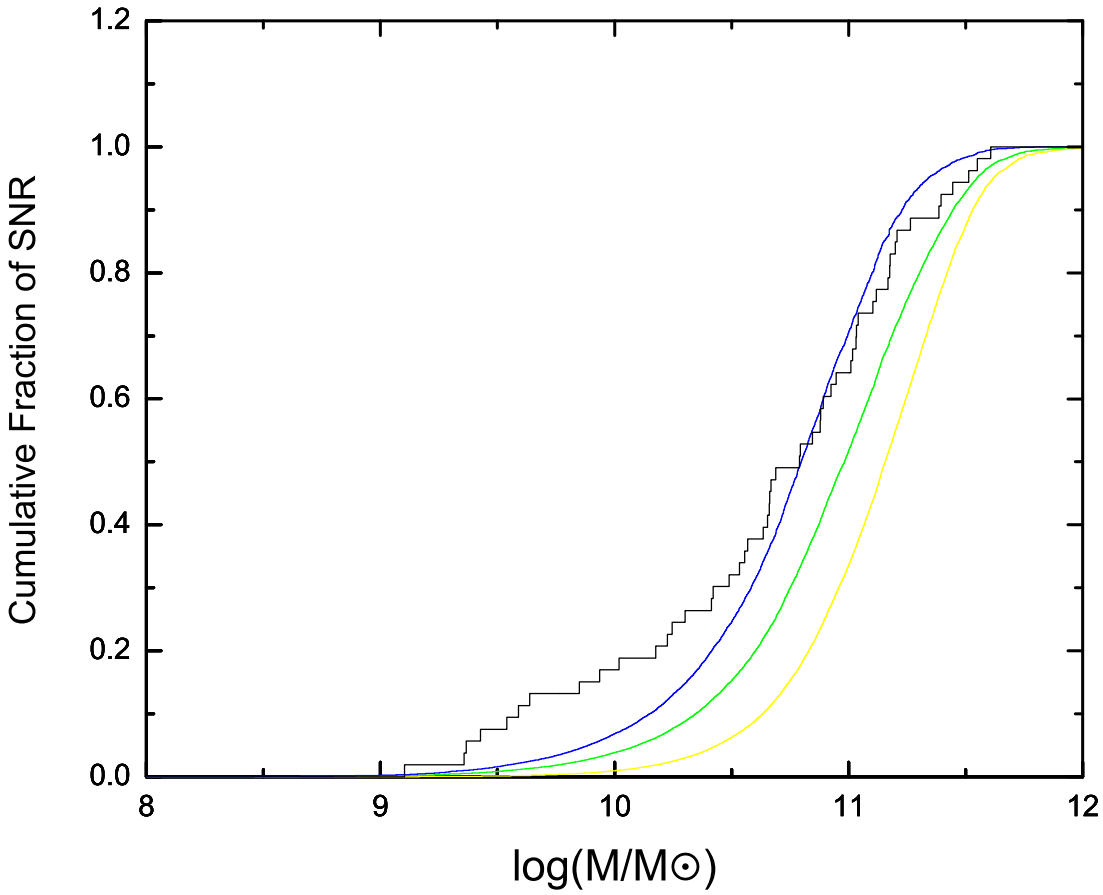

Figure 4.1: Cumulative distribution functions of mass-ranked K-S tests for our best-fit A+B model (green), the AM-term-only model (yellow), and the BSFR-term-only model (blue). This plot follows the colour-coding scheme described in Table 4.1. The green and yellow lines are rejected by the K-S test, showing that our best-fit A+B model and all A+B models with a higher A/B ratio do not agree with our data.

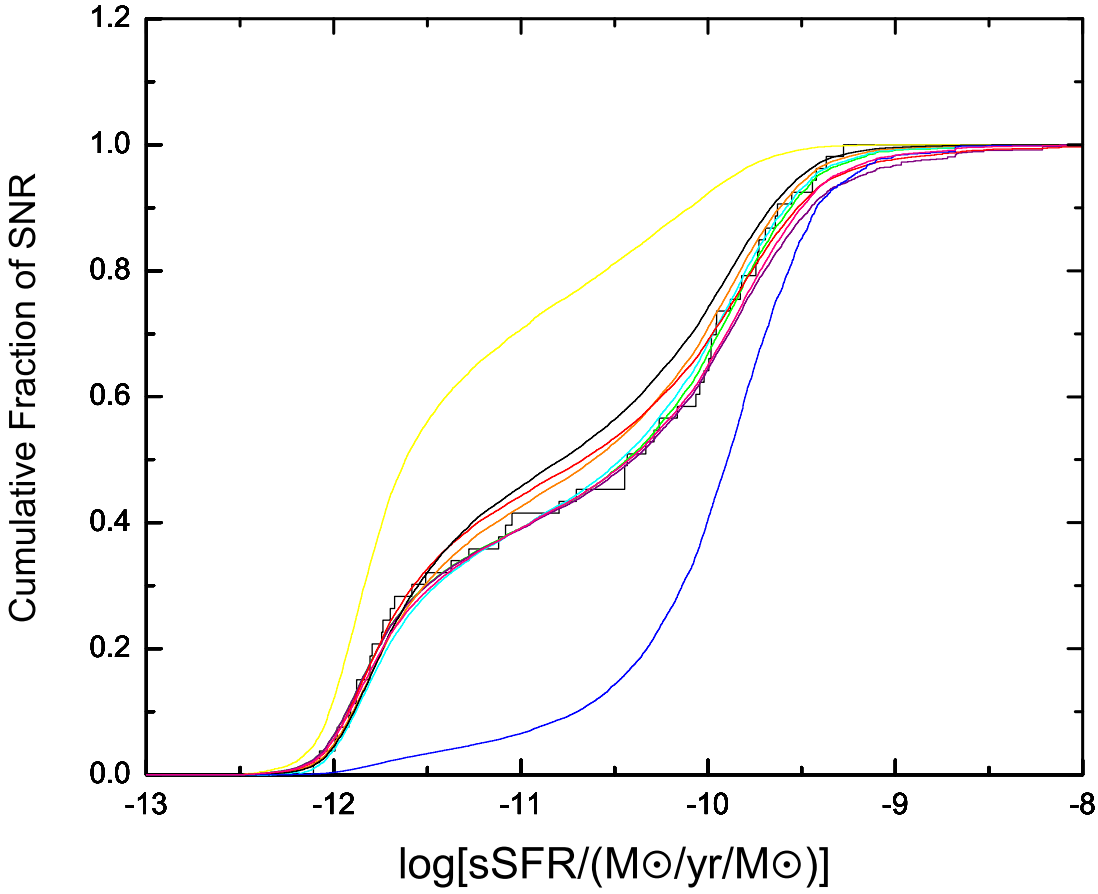

Figure 4.2: Cumulative distribution functions of the specific-star-formation-ranked K-S tests for the various models. The only models which were rejected were the mass-only model (yellow), and the SFR-only model (blue). This plot follows the colour-coding scheme described in Table 4.1. As described in the text, this set of K-S tests is largely inconclusive.

ranked KS test, and the cumulative distribution function of the observed data lies significantly beyond the region encompassed between the lines. This means that modifying the parameters of our A+B fits such that the B value is larger relative to the A value will not yield a satisfactory model (see Figure 4.3). Since we have already concluded that a larger A/B value would not be appropriate for the mass-ranked tests (see the beginning of this section, as well as Figure 4.1), we now reach the conclusion that no A+B model could match our observed data, regardless of what values for A and B are taken. Note that this conclusion holds for all A and B values, regardless of scaling effects, since scaling A and B by a certain factor does not affect the cumulative distributions used in our KS tests. The results of these KS tests (and many more to come) are shown in Table 4.1.

To present a more illustrative view of this discrepancy, we imitate Fig. 6 of Sullivan et al. (2006) in Figure 4.4 of this paper. We bin our galaxies by specific SFR (sSFR), and plot the specific SNR for each bin. Then, we make a mass cut at $\log(M/(M_\odot))$=10.7, dividing the galaxies into two groups of different mass, each containing half the SNe. For each group, we repeat the plotting process above, showing that low-mass galaxies have a systematically higher specific SNR than their high-mass counterparts. Applying different mass cuts consistently results in the same trend. A plot of the differential distribution functions of SNR predicted by the A+B model vs the actual observed SNR (see Figure 4.5) further illustrates the issue, where the curves have been scaled to show the relative absolute SNR obtained by each model.

From Figure 4.5, it can be seen that both the predictions of our best-fit A+B model (green line) and that of Sullivan et al. (2006) (blue line) under predict the rates of supernovae hosted by low mass, high specific star formation rate galaxies, while over-predicting the rates of high mass SNe (the red line is a modified model, to be explained later in this chapter). The two A+B models are in reasonable agreement with each other.

As stated in Section 2, there exists the issue that the MPA/JHU catalogue systematically overestimates the SFRs of passive (non-star-forming) galaxies, assigning them SFRs of $\sim 0.1 M_\odot/yr$. However, this is not expected to be the cause of the discrepancy stated above, since passive galaxies tend to have a high mass (of order 10^{10} to 10^{12} $M_\odot$); therefore a $0.1 M_\odot/yr$ overestimate of the SFR should not significantly affect the predicted SNRs. To further make sure that this systematic effect is not an issue, we redo the A+B fits by setting the SFRs of all galaxies with an sSFR smaller than -11.5 $M_\odot/yr$ per $M_\odot$ to zero. We obtain $A = 3.6^{+1.0}_{-0.6} \times 10^{-14} (M_\odot)^{-1}$

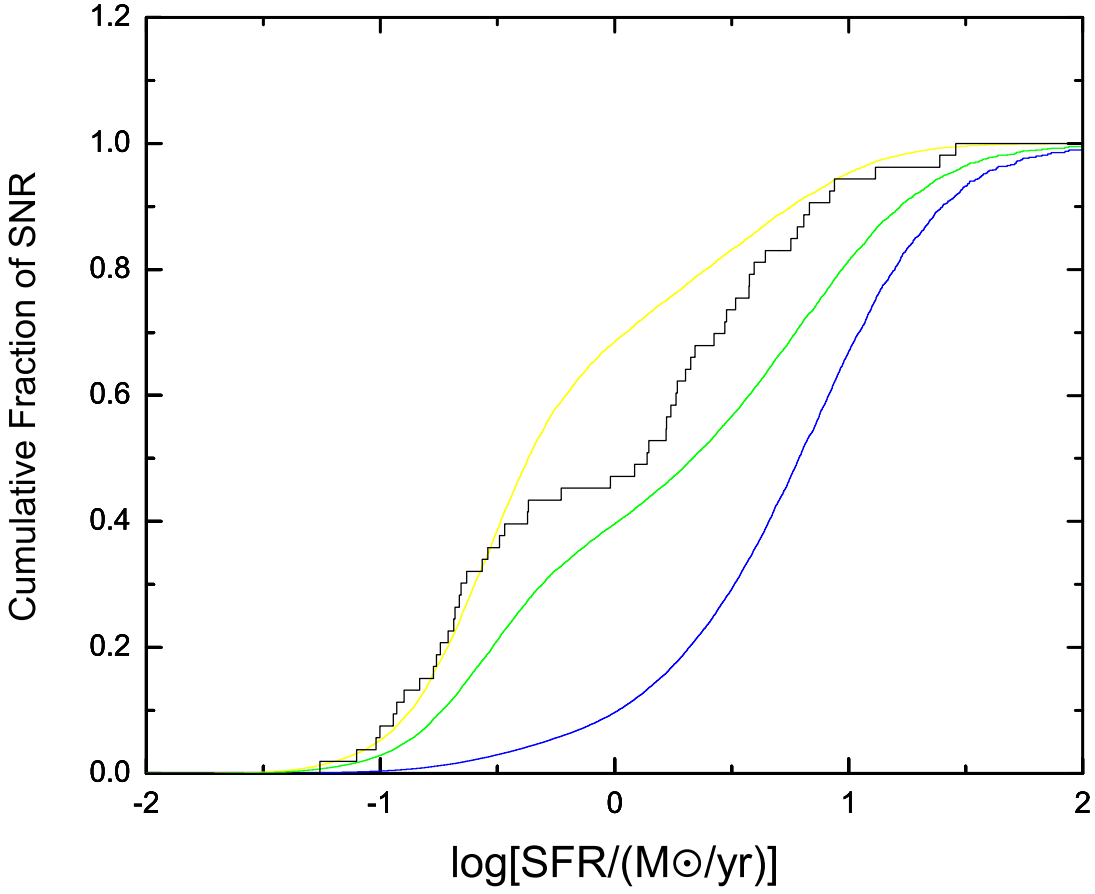

Figure 4.3: Cumulative distribution functions of SFR-ranked K-S tests for our best-fit A+B model (green), the AM-term-only model (yellow), and the BSFR-term-only model (blue). This plot follows the colour-coding scheme described in Table 4.1. The green and blue lines are rejected by the K-S test, showing that our best-fit A+B model and all A+B models with a lower A/B ratio do not agree with our data. This, in conjunction with Figure 4.1, rules out all A+B models.

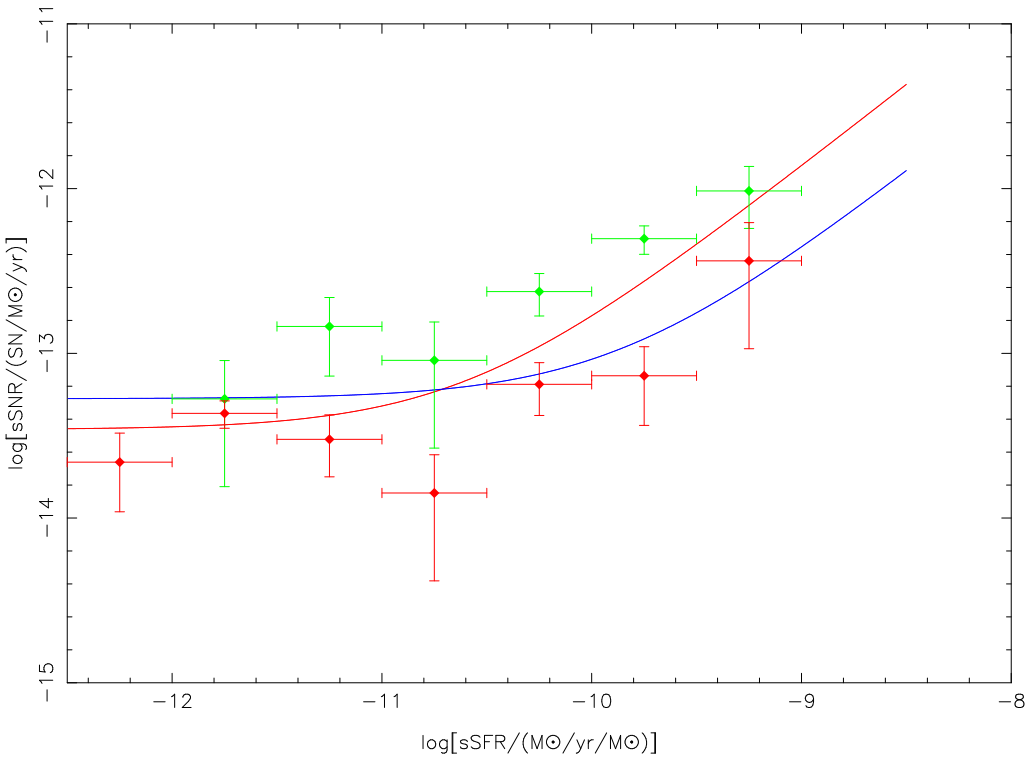

Figure 4.4: Specific supernova rate as a function of specific star formation rate. The green diamond points correspond to our low-mass sample, and the red diamond points our high-mass sample. The vertical error bars indicate Poisson errors for our SNe numbers in each bin, and the horizontal error bars correspond to bin size. The trend that the green points tend to lie above the red ones exists for all mass regime discrimination criteria we try. Also plotted are the predictions of our best-fit A+B model (red line), the predictions of Sullivan et al. (2006) (blue line). Our results have been scaled to account for observing window issues.

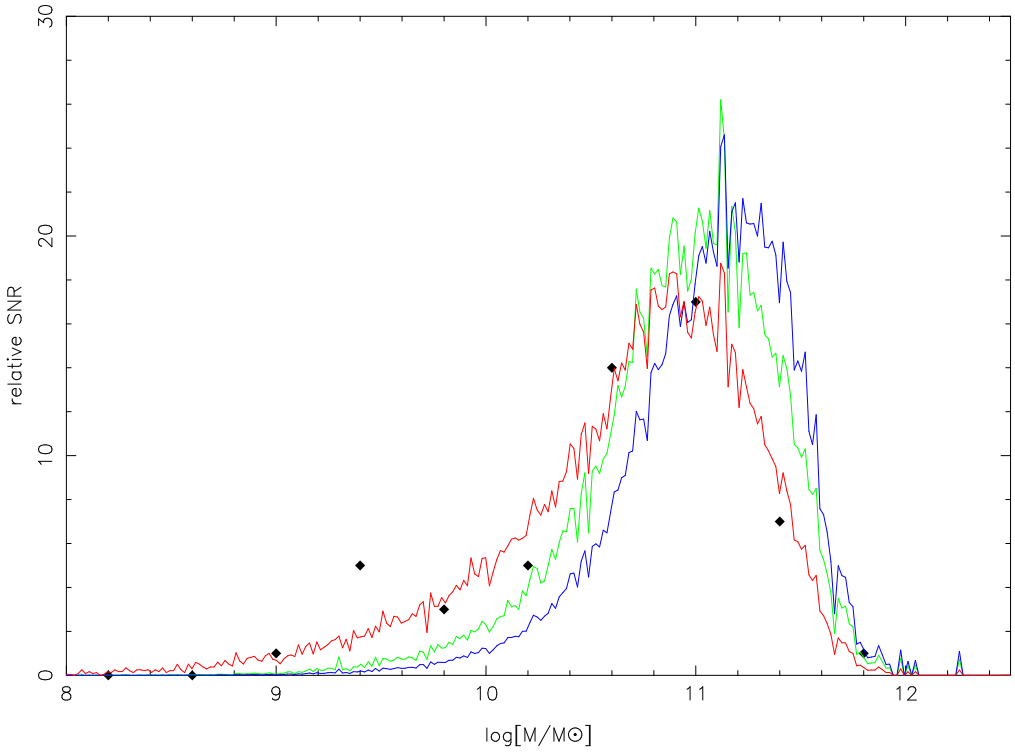

Figure 4.5: Differential distribution functions of supernova rate as a function of host mass. The black data points correspond to our observed data. The green and blue lines are the predictions of our best-fit A+B model and the results of Sullivan et al. (2006) respectively. The red line is the prediction of our best-fit AM+BSFR+C "constant background" model. Our results have been scaled to account for observing window issues.

and $B = 1.3 \pm 0.3 \times 10^{-3} (M_{\odot} \mathrm{yr}^{-1})^{-1}$. This is a negligible difference, as shown in Figure 4.6, which plots the differential distributions of the SNR predicted via this model vs. the actual SNR data. Also plotted for comparison are our previous results for the best fit A+B model obtained in the last section (green line), and the results of Sullivan et al. (2006) (blue line).

4.2 The 3rd Parameter

We have demonstrated above that the A+B model does not reproduce our data well. Mass-ranked KS tests reject all A and B values with a higher A/B ratio than our best-fit values, while SFR-ranked KS tests reject those with a smaller A/B ratio. Furthermore, from Figures 4.1, 4.4 and 4.5, we can see that there exists a SNR excess in low mass galaxies. To account for this, we try adding a third parameter to the A+B model. Previous work proposed a modification to the A+B model of the form $SNR/M = A + B(SFR/M)^{y}$, where $y = 0.5 \pm 0.2$ (see Pritchet et al. 2008). Thus, we attempt this approach first, and apply a 3-parameter fit with A, B and y as the parameters to be determined. The rationale of doing so is that the specific SFR is sensitive to mass, so any deviation from 1 in the parameter y would inevitably cause the discrepancy observed. However, Monte Carlo simulations similar to those in Figure 3.1 show that B and y are highly degenerate for our sample size, and that our maximum likelihood methods cannot distinguish between different sets of (B,y). Lacking the means to fit a third parameter this way, we instead adopt a more explicit formulation for a mass-dependent term:

$$SNR = A \cdot M + B \cdot SFR + C \cdot M^{k}, \tag{4.1}$$

where A, B and C are free parameters, and k is a pre-defined arbitrary power-law index (Similar to the B-y degeneracy, there is no way to determine k given a free C parameter). We will refer to this as the A+B+C model for the rest of this paper. To test that maximum likelihood can reliably recover the C parameter, we again apply Monte Carlo simulations assuming a standard A+B model with $A = 4 \times 10^{-14} M_{\odot}^{-1}$) and $B = 2 \times 10^{-3} (M_{\odot} \mathrm{yr}^{-1})^{-1}$, and generate fake SNe into our spectroscopic sample according to these values. To our simulated data, we apply A+B+C fits with k=0, thus, ideally, the program should return a C value of 0 every time. The results are that the maximum likelihood fitting function returns very small C values, accounting

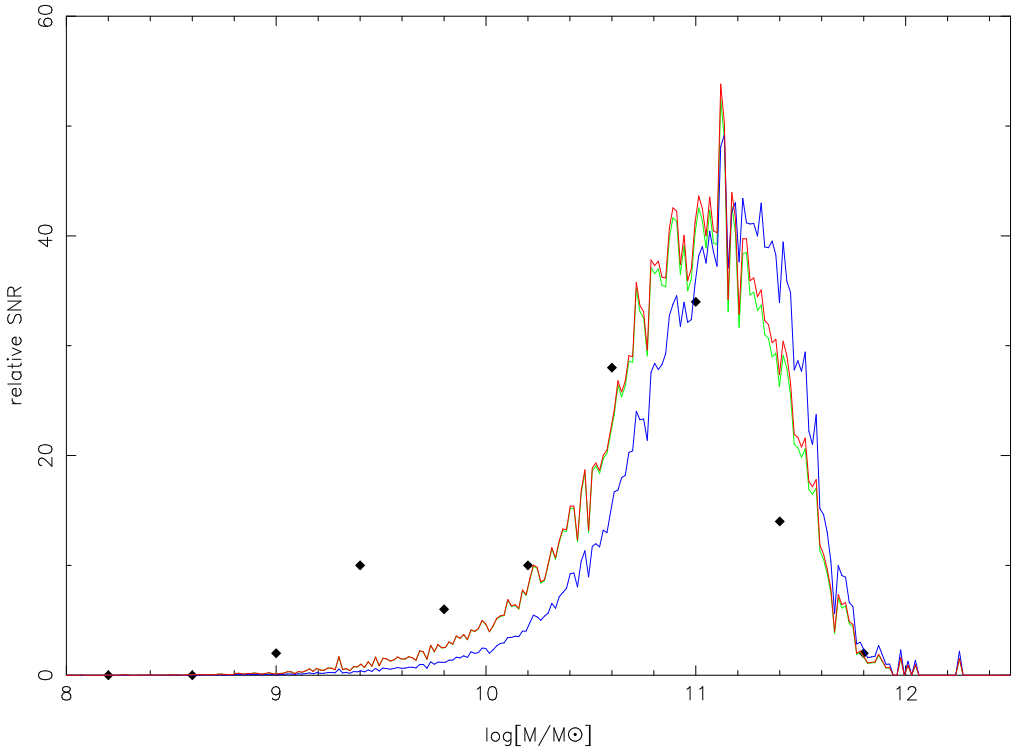

Figure 4.6: Differential distribution of SNe Ia as a function of host mass. Plotted here are the theoretical predictions of our best-fit A+B model (green), the best-fit A+B model after setting the SFR of low specific star formation rate galaxies to zero (red), and the Sullivan et al. (2006) A+B model (blue). It can be seen that there is no significant difference between the red and green lines. Our results have been scaled to account for observing window issues.

for no SNe half the time and rarely accounting for more than 10% of the total number of SNe.

In order to obtain more SNe at low mass extremes, it is intuitive that k must be smaller than 1. To confirm this intuition, we fit A,B and C with k=2. The result is a minus C value ($A = 6.4^{+1.6}_{-1.8} \times 10^{-14}(M_\odot)^{-1}$, $B = 1.2^{+0.4}_{-0.3} \times 10^{-3}(M_\odot \mathrm{yr}^{-1})^{-1}$, $C = (-1.4)^{+0.8}_{-0.2} \times 10^{-25}(M_\odot^2)^{-1}$), which may be unphysical, since extremely high-mass galaxies would have a negative SNR if this were the case, and the resulting distribution is rejected by the mass-ranked K-S test at 99% confidence (see Figure 4.7). Also intuitive is the suspicion that k must also have a lower limit, since otherwise the SNR distribution function would be much higher than observed at the low-mass end. Fitting A,B and C with k=-2, the maximum likelihood method returns a value of 0 for C every time. This hints that k=-2 is below the lower limit.

We fit A,B and C using k=-1,-0.5, and 0, and apply mass-ranked K-S tests to the respective best-fit models respectively (again, see Figure 4.7 for details). We obtain (A,B,C)=($3.4^{+1.0}_{-0.6} \times 10^{-14}(M_\odot)^{-1}$,$1.0^{+0.4}_{-0.2} \times 10^{-3}(M_\odot \mathrm{yr}^{-1})^{-1}$,$2.8^{+2.2}_{-1.5} \times 10^6 M_\odot$), ($2.8^{+1.0}_{-0.6} \times 10^{-14}(M_\odot)^{-1}$,$0.70^{+1.05}_{-0.42} \times 10^{-3}(M_\odot \mathrm{yr}^{-1})^{-1}$,$2.3^{+1.0}_{-0.6} \times 10^2 M_\odot^{1/2}$), and ($9.6^{+12.8}_{-9.5} \times 10^{-15}(M_\odot)^{-1}$,$4.6^{+3.4}_{-2.6} \times 10^{-4}(M_\odot \mathrm{yr}^{-1})^{-1}$,$3.6^{+1.4}_{-0.4} \times 10^{-3}$) respectively. None of them are rejected at the 95% confidence level, though k=-1 was rejected at 93%. The C term accounts for a very significant proportion of the SNe in each case, with 25 out of 53 hosted by the C term in the case of k=0. Also taking into consideration the very good match to the data of the $k = 0$ model as displayed in Figure 4.5, this prompts us to attempt to fit a constant-rate model (ie that SN rates are the same in every galaxy, regardless of mass or SFR). The constant-rate model passes the K-S test (only 25% rejection), though it was rejected to 96% confidence for the SFR-ranked tests (see Figure 4.8 for details). This shows that, although a C term in the form of a constant background SNR could be accomodated, it is at least not overwhelmingly dominant.

We also try a different formulation for C, to probe whether or not the C term could be explained by a model which is not explicitly of the form $SNR = A \cdot M + B \cdot SFR + C \cdot M^k$:

$$SNR = (A \cdot M + B \cdot SFR) \cdot (1 + C/M), \tag{4.2}$$

which also passes the K-S test (see Figure 4.9 for details) once the best-fit values are applied ($A = 1.8^{+0.7}_{-1.3} \times 10^{-15}(M_\odot)^{-1}$, $B = 6.6^{+4.6}_{-6.6} \times 10^{-5}(M_\odot \mathrm{yr}^{-1})^{-1}$, $C = 3.2^{+22.0}_{-2.8} \times 10^{11}(M_\odot)$). This has certain implications for the physics behind the third parameter,

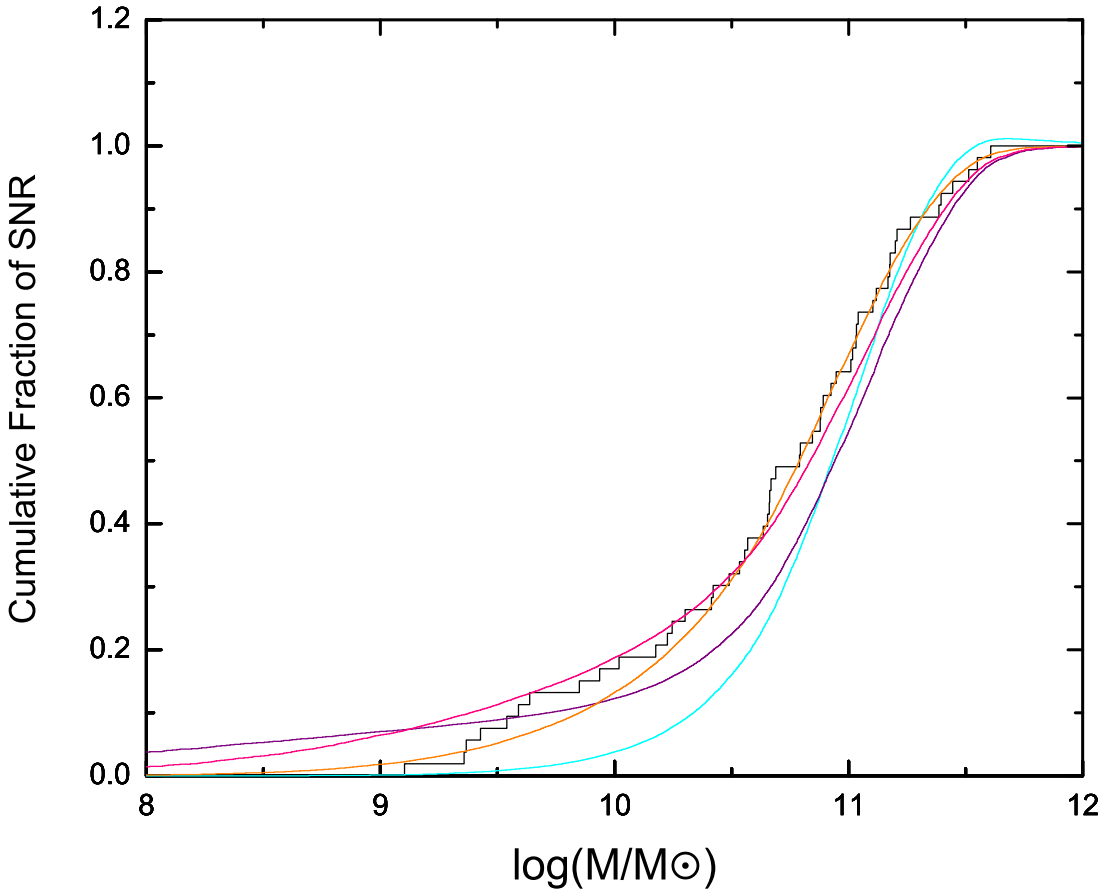

Figure 4.7: Mass-ranked K-S tests for various $SNR = A \cdot M + B \cdot SFR + C \cdot M^k$ models: k=2 (cyan), k=0 (orange), k=-0.5 (pink), and k=-1 (purple). This plot follows the colour-coding scheme described in Table 4.1. Note that part of the cyan curve lies above 1 - this is due to the unphysical negative SNR values of some high - mass hosts derived from a minus C.

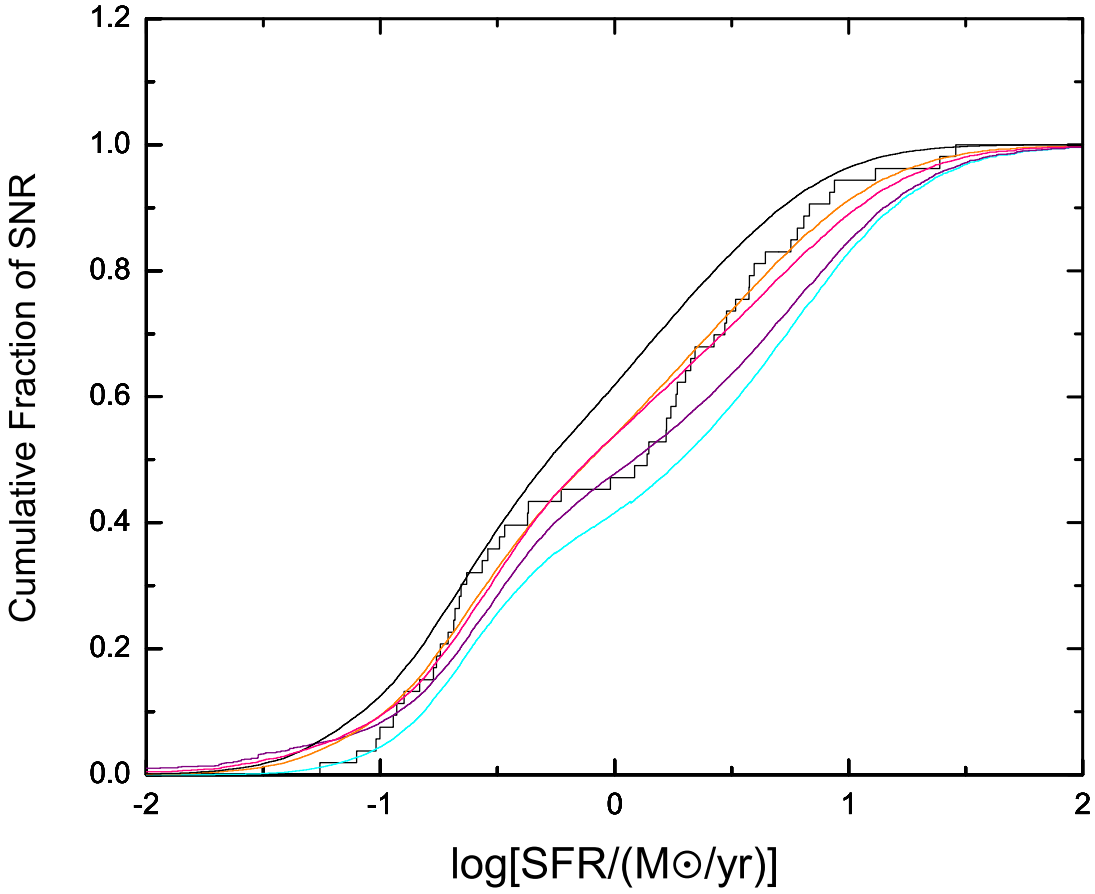

Figure 4.8: Cumulative distribution functions of SFR-ranked K-S tests for various $SNR = A \cdot M + B \cdot SFR + C \cdot M^k$ models: k=2 (cyan), k=0 (orange), k=-0.5 (pink), and k=-1 (purple), as well as the cumulative distribution function for the constant rate model (black). This plot follows the colour-coding scheme described in Table 4.1. The chief significance of this plot is that the constant rate model is rejected.

Table 4.2: These are the best-fit values for the parameters we obtain from our data, which we assume for the parameters when testing the respective models.

Model	A $10^{-14}(M\odot)^{-1}$	B $10^{-3}(M_\odot \mathrm{yr}^{-1})^{-1}$	C (appropriate units)
$AM + BSFR$	$3.5^{+0.9}_{-0.7}$	$1.3^{+0.4}_{-0.3}$	-
$AM + BSFR + CM^2$	$6.4^{+1.6}_{-1.8}$	$1.2^{+0.4}_{-0.3}$	$(-1.4)^{+0.8}_{-0.2} \times 10^{-25}$
$AM + BSFR + CM^{-1}$	$3.4^{+1.0}_{-0.6}$	$1.0^{+0.4}_{-0.2}$	$2.8^{+2.2}_{-1.5} \times 10^{6}$
$AM + BSFR + C$	$0.96^{+1.28}_{-0.95}$	$0.46^{+0.34}_{-0.26}$	$3.6^{+1.4}_{-0.4} \times 10^{-3}$
AM only	6.8±0.9	-	-
$(AM + BSFR)(1 + CM^{-1})$	$1.8^{+0.7}_{-1.3}$	$0.066^{+0.046}_{-0.066}$	$3.2^{+22.0}_{-2.8} \times 10^{11}$
constant rate	-	-	$5.4\pm0.7 \times 10^{-3}$
$BSFR$ only	-	2.7±0.4	-
$AM + BSFR + CM^{-1/2}$	$2.8^{+1.0}_{-0.6}$	$0.70^{+1.05}_{-0.42}$	$2.3^{+1.0}_{-0.6} \times 10^{2}$

as will be mentioned in the discussion.

All the above "third parameter" models pass the sSFR-ranked KS test (see Figure 4.2 for details).

Table 4.2 gives a summary of the maximum likelihood values for our different model parameters. For a summary of the results of our various KS tests, see Table 4.1.

4.3 Tests for the Smith Model

As mentioned above, Smith et al. (2011) found a similar deviation of SNR from the standard A+B model in the SDSS data via photometric masses and SFRs of the

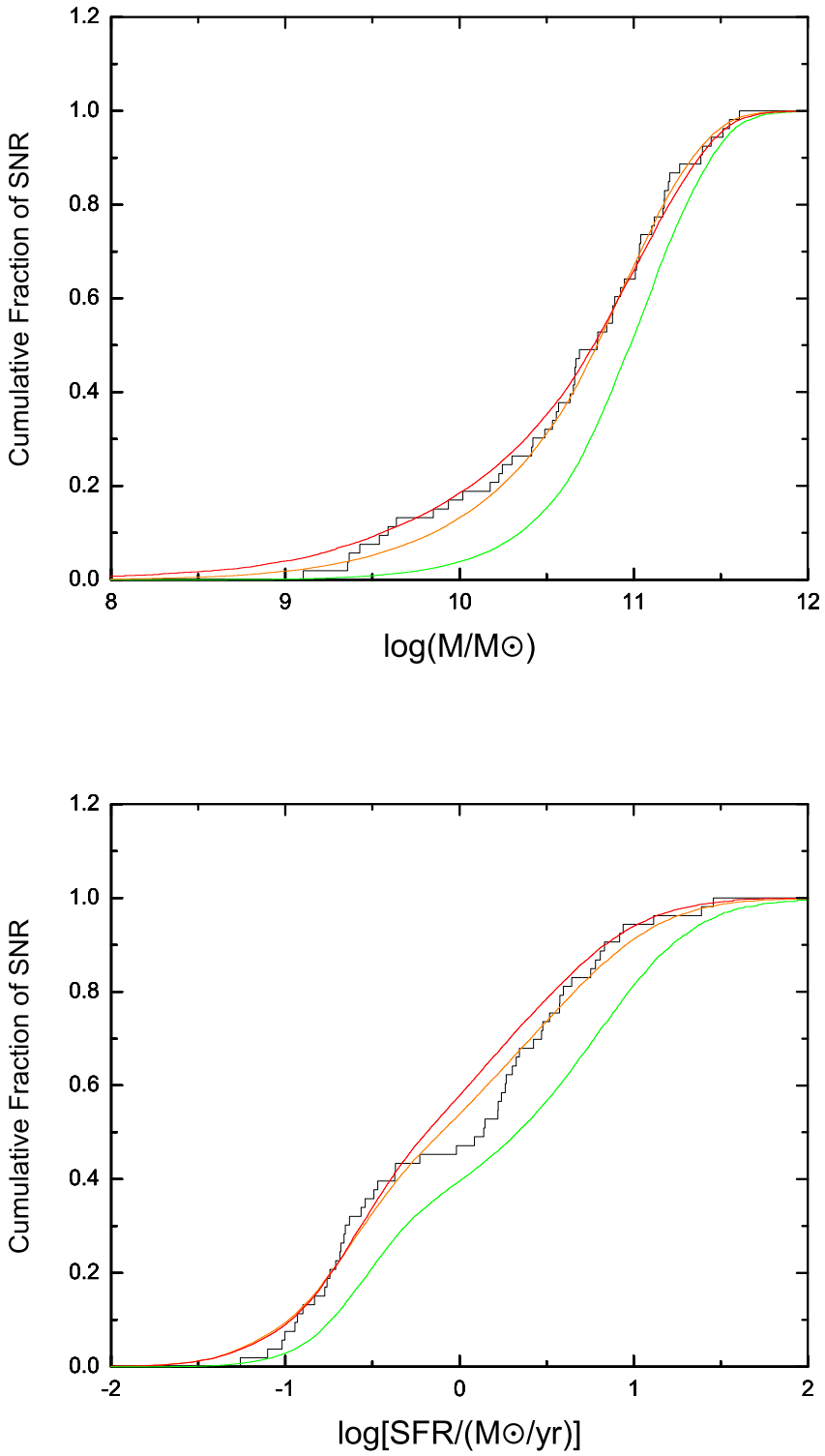

Figure 4.9: Mass-ranked (top) and SFR-ranked (bottom) K-S tests for the $(AM + BSFR)(1+CM^{-1})$ model (red). Also plotted are the AM+BSFR+C model (orange), and the best fit generic A+B model (green). This plot follows the colour-coding scheme described in Table 4.1.

SDSS photometric sample. They proposed the model:

$$SNR = AM^x + BSFR^y, \tag{4.3}$$

and obtained the 4 parameters by the following means. They fit A and x first using passive galaxies and SNe hosted by them, and then performed a 2 parameter fit for B and y using the remainder of the sample, and finally performed a simultaneous fit for all parameters to check the validity of the values, which they found to agree very well. They present values of $A = 1.05 \pm 0.16 \times 10^{-10}$, $x = 0.68 \pm 0.01$, $B = 1.01 \pm 0.09 \times 10^{-3}$, $y = 1.00 \pm 0.05$ from the final simultaneous bivariate fitting as final results, which are shown to explain the observed SNR better than the generic A+B model. They also fit the data using the generic A+B model and show that the resulting parameters are consistent with the findings of previous authors.

Due to the fact that our sample size is much smaller (19987 spectroscopic galaxies with only 53 hosts, as opposed to 750,000 photometric galaxies after various cuts were applied, and 342 hosts), our problems with an A-x and B-y degeneracy are even greater, rendering it impossible to fit either A and x or B and y at the same time. We attempt to apply the method by which Smith et al. (2011) initially obtained the value of x, namely, binning the passive (non-star-forming) galaxies within the galaxy sample by mass, finding the per-galaxy SNR in each bin, and plotting the per-galaxy SNR as a function of mass. A subsequent least-squares straight line fit through the plotted points should then have a slope of equal to x. However, due to a weakness in the MPA/JHU algorithm, the spectroscopic SFRs obtained are never less than $log(SFR) \sim -1$, and there is consequently no clear distinction between truly "passive" galaxies and those merely with a very low SFR (as mentioned above). To approximate the method used by Smith et al, we take galaxies with $\log(M) > 10$ and $sSFR < -11$, a total of 22, and take these to be our "passive" galaxy sample. The resultant plot (see Figure 4.10) yields $x = 0.29 \pm 0.05$ for a least-squares fit through the points for all 5 bins (red line), but if the first point is omitted, a least-squares fit through the remaining 4 points (green line) yields $x = 0.59 \pm 0.13$. Different mass and sSFR cuts yield values for x more or less within this range, but we were not able to distinguish between the values due to our relatively small sample (as few as 2 host galaxies for some points plotted in Figure 4.10), and while relaxing the mass and sSFR cuts would generate a larger sample of "passive" galaxies, it would also aggravate the contamination from non-passive galaxies. Thus, we conclude that our

data sample hints strongly that $x < 1$, with the upper limit about the value obtained by Smith et al. (2011), but is insufficient for obtaining the parameters of the Smith model.

While we were not able to retrieve the parameter values for the Smith model, we were able to test the validity of the model, assuming values for A, x, B and y as found by the authors. A mass-ranked KS test (see above) does not reject the model (only 47% rejection, see Figure 4.11 for cumulative distributions). This is somewhat expected, since the authors (prior to the simultaneous bivariate fitting) placed a greater emphasis on mass dependence when fitting the parameters, fitting A and x before correcting for any discrepancies with the $B{\cdot}SFR^y$ term. This treatment almost guarantees a good mass dependence prediction, since any unknown SNR contributor terms which have a dependence on mass would be absorbed by the AM^x term. Even though the final results for the parameters presented were not the result of this method, the results of the two methods agree well. This is not the case for the SFR dependence, however, and a SFR-ranked KS test rejects the model by >99% (see Figure 4.12). Since either test is a necessary but insufficient condition of the model matching our data, we conclude that the Smith model with the parameter values $A = 1.05 \pm 0.16 \times 10^{-10}$, $x = 0.68 \pm 0.01$, $B = 1.01 \pm 0.09 \times 10^{-3}$, $y = 1.00 \pm 0.05$ does not match our data well, though this does not rule out the possibility that a Smith model with another set of parameter values may perform better.

We also plot the theoretical differential distribution of SNR as a function of mass according to the Smith model with the parameter values quoted within our sample (see Figure 4.13 for details), and compare it with the observed SNR, as well as our best-fit A+B model, the Sullivan et al. (2006) A+B model, and our best-fit $SNR = A \cdot M + B \cdot SFR + C$ model. It can be seen that the Smith model with the given parameters, like the A+B model, does not match the SNR of low-mass galaxies well.

Finally, we test how well the Smith model explains the split between high-mass vs. low-mass hosts on a sSNR-sSFR plane, as depicted in Figure 4.4. We seed our spectroscopic galaxies with imaginary SNe according to the model, and bin the SNe, masses and SFRs in the same bins used to obtain Figure 4.4, taking the same mass cuts ($10^{10.7} M_\odot$). In this figure, we bin the galaxies into 7 specific star formation rate bins, and calculate the average sSNR of each bin:

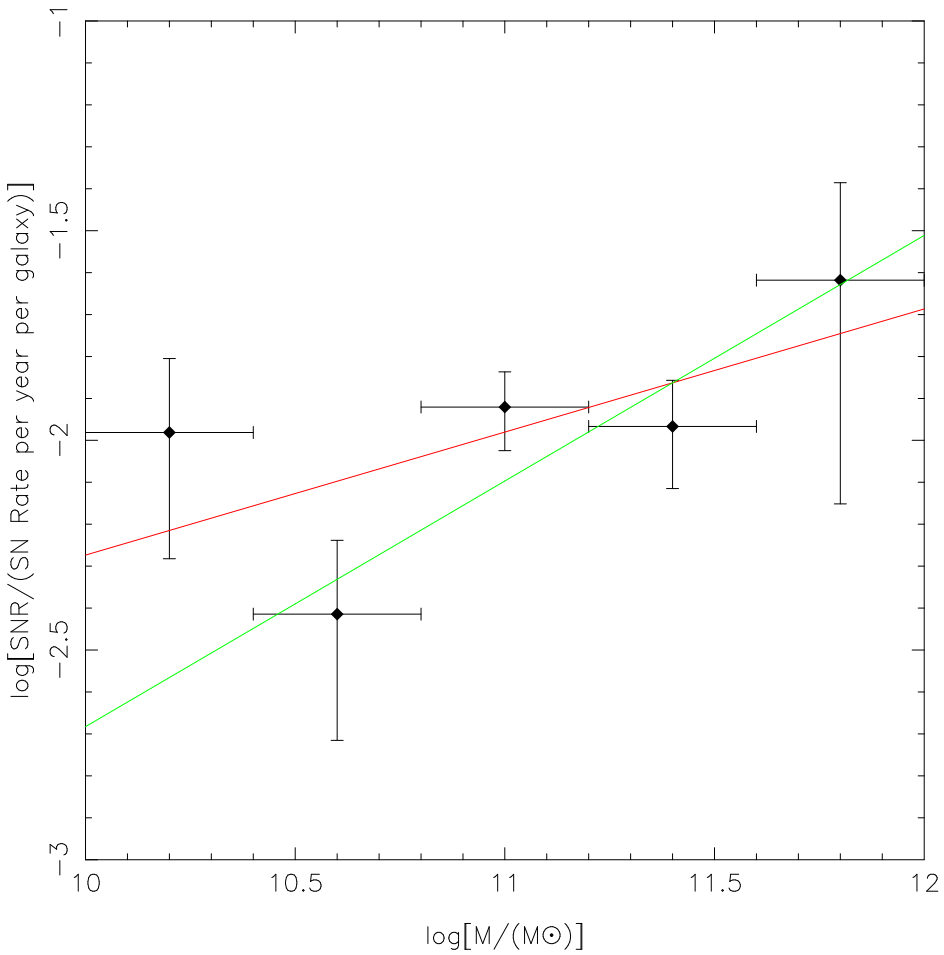

Figure 4.10: Attempt to recover parameter x of the Smith model ($SNR = AM^x + BSFR^y$). The points were obtained through binning the data in mass bins after making mass and sSFR cuts as discussed in the text ($\log(M) > 10$, $sSFR < -11$), the red line (slope 0.29±0.05) is a least-squares fit to all 5 data points, and the green line (slope 0.59±0.13) is a fit to 4 of the data points, omitting the first on the left. 3 of the 5 data points (the first, second and fifth from the left) were plotted with less than 3 SN Ia hosts, and consequently this method suffers from small-number statistics when applied to our sample.

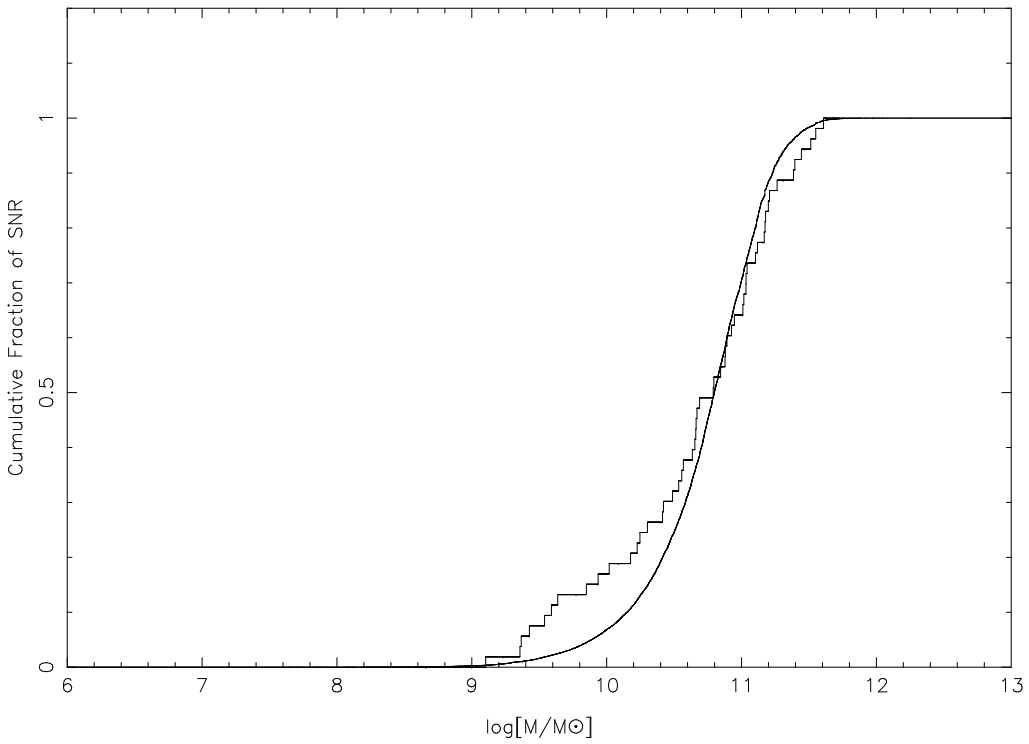

Figure 4.11: Mass-ranked KS test for the Smith model. The model was not rejected (47% rejection), which was expected for reasons explained in the paper.

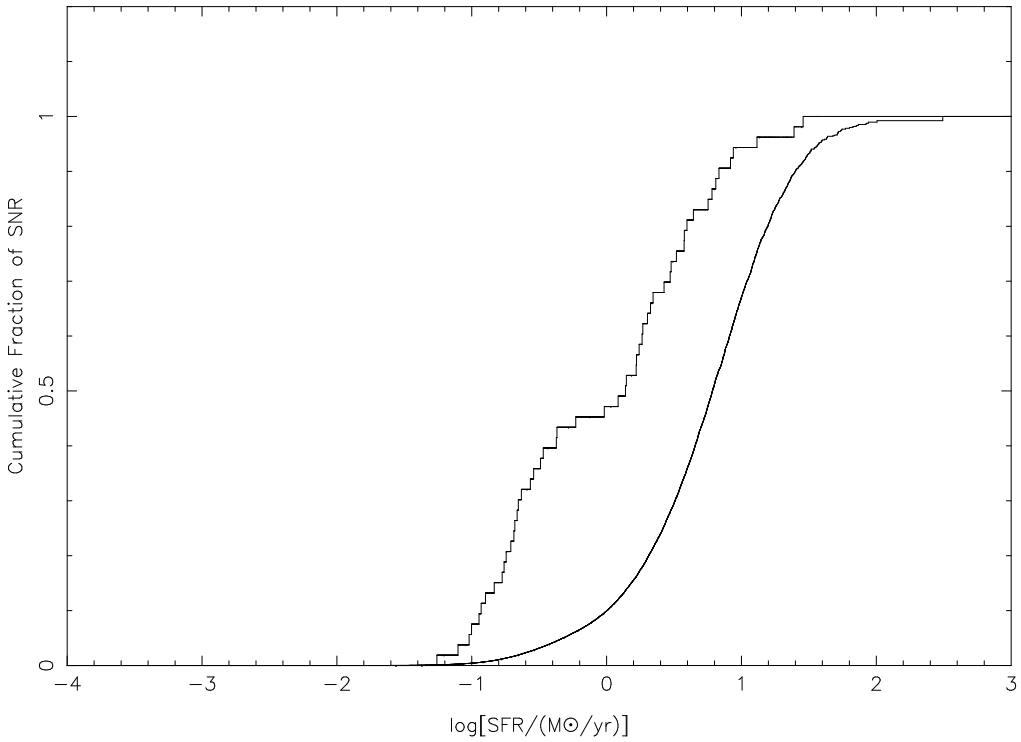

Figure 4.12: SFR-ranked KS test for the Smith model. This test rejects the model at $> 99\%$ confidence, and rejects the possibility that a Smith model with parameters as given by Smith et al. (2011) explains the deviation from the generic A+B model seen in our sample.

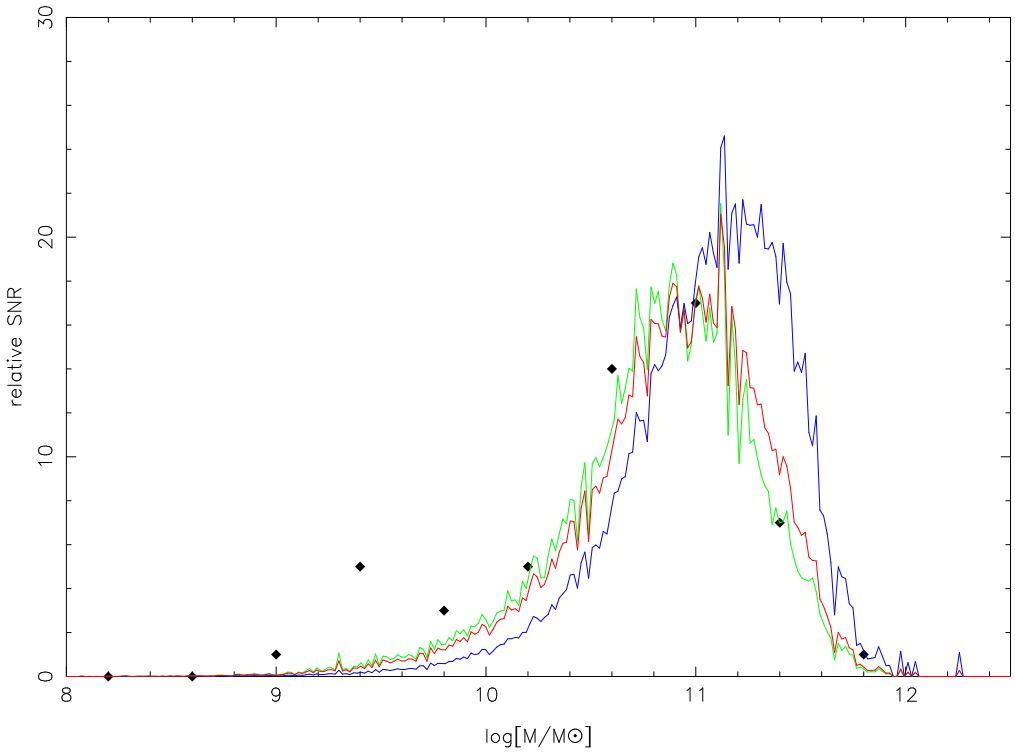

Figure 4.13: Differential distribution functions of supernova rate as a function of host mass. The black data points correspond to our observed data. The red, green, blue and orange lines correspond to the predictions of the Smith model, our best-fit A+B model, the results of Sullivan et al. (2006) and our best-fit $AM + BSFR + C$ model respectively. Our results have been scaled to account for observing window issues.

$$\begin{aligned} sSNR &= \frac{\Sigma SNR_i}{\Sigma M_i} \\ &= A\frac{\Sigma M_i^x}{\Sigma M_i} + \frac{\Sigma SFR_i^y}{\Sigma M_i}, \end{aligned} \tag{4.4}$$

where i denotes a galaxy within the bin. For the Smith model, $y{\sim}1$. Therefore, for a fixed sSFR bin, $\Sigma SFR_i^y/\Sigma M_i$=sSFR. Thus, for each bin, we have

$$sSNR = A\frac{\Sigma M_i^x}{\Sigma M_i} + sSFR. \tag{4.5}$$

The result is shown in Figure 4.14. The trend that high mass galaxies tend to have a lower specific SNR than the A+B model is reproduced, though not as prominent as that seen in our sample.

4.4 Attempts to Create a Metallicity-Dependent SNR Model

It has been proposed by Cooper et al. (2009) that the SNR of a potential host galaxy is correlated with its gas-phase metallicity. By comparing samples of host galaxies with samples of random galaxies with similar distributions of rest-frame colour, luminosity, mass, SFR and redshift, they found that for bluer galaxies (which usually have a higher SFR), SNe preferentially occur in environments which are of low density. They interpret this to be the result of a factor, other than colour, luminosity, mass, SFR or redshift, which affects SNR, and is also correlated to environment density. For this purpose, gas-phase metallicity is a valid candidate, which they present as a likely possibility. They also mention that their results could also be explained by assuming that SNe occur more often in the material that is lost from ram-pressure stripping when galaxies merge, which would happen more frequently in dense environments. The SNe would then be intracluster SNe, and not be matched to any host, thereby leading to fewer SNe in galaxies in dense environments. However, the material galaxies typically lose in ram-pressure stripping consist of their metal-poor outskirts, thereby failing to rule out the possibility that a higher gas-phase metallicity leads to a lower SNR. Thus, they conclude that SNe occur more often in metal-poor systems, contradictory to earlier theoretical models which claim the contrary (eg. Kobayashi

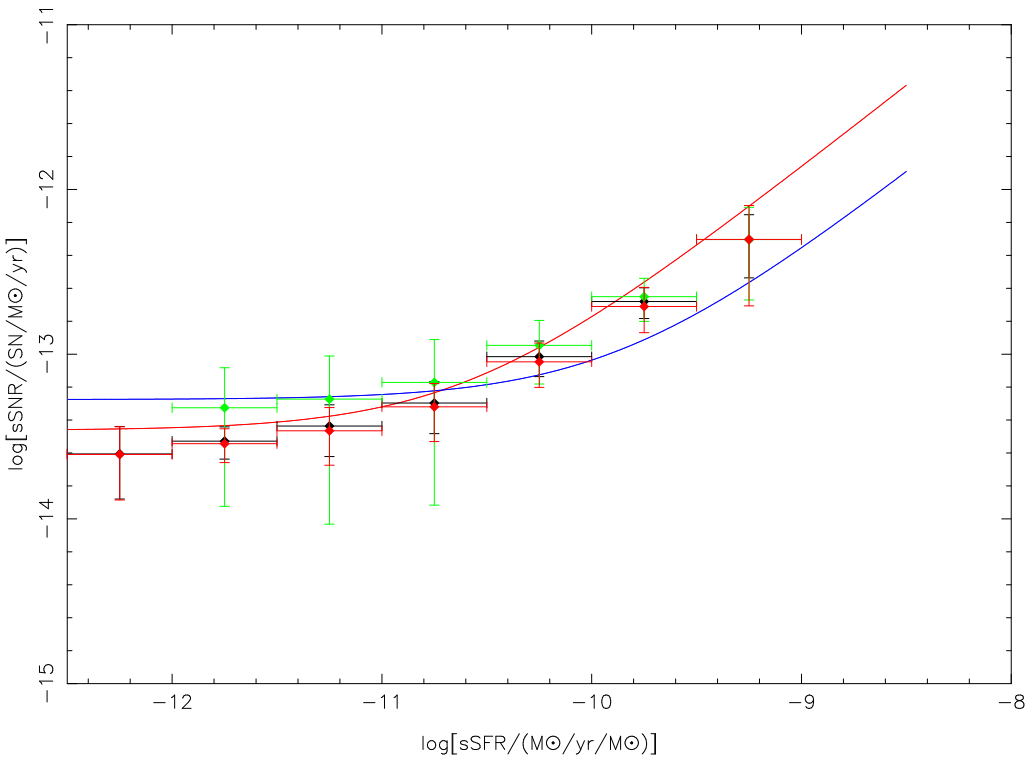

Figure 4.14: Simulation of Smith model SNR Distributions on sSNR-sSFR plane (specific supernova rate as a function of specific star formation rate). The green diamond points correspond to the low-mass sample, the black diamond points the total sample, and the red diamond points the high-mass sample. The vertical error bars indicate Poisson errors for our SNe numbers in each bin, and the horizontal error bars correspond to bin size. The trend that the green points tend to lie above the red ones is successfully predicted, though not as prominently as in our sample. Also plotted are the predictions of our best-fit A+B model (red line), the predictions of Sullivan et al. (2006) (blue line).

et al. 2000).

If this conclusion is taken to be true, it could resolve the observed discrepancy between the A+B model and our data, as it would account for the difference between the observed SNR and that predicted by the A+B model in low-mass galaxies (which are generally metal poor). Therefore, we attempt to create and fit a SNR model which is an explicit function of the gas-phase metallicity (Tremonti et al. 2004). Searching the gas-phase metallicity catalogues of the MPA/JHU sample, however, only yields 4840 galaxies within Stripe 82, 14 of which are SN Ia hosts. By plotting probability distribution functions of the parameters of various models resulting from fits to this data, it can be seen that these data are insufficient for the purposes of discriminating between different models.

To obtain a larger sample for analysis, we look to the VESPA stellar-phase metallicities, which we obtain by taking the mass-weighted average metallicity for each age bin. However, as expected, they are in poor correlation with gas-phase metallicities (see Figure 4.14 for the comparison). Subsequent Maximum Likelihood fits show that an additional linear stellar-phase metallicity term (both $A{\cdot}M + B{\cdot}SFR + C{\cdot}Z$ and $A{\cdot}M + B{\cdot}SFR + C{\cdot}MZ$) is also in poor correlation with SNR, as the contribution of a separate metallicity term is always negligible, accounting for less than 1 SN. This is in agreement with Cooper et al. (2009), the results of which do not support a stellar metallicity-dependent SNR. Future work on our dataset may investigate alternate stellar-phase metallicity dependent models which do not present the stellar metallicity as a linear term.

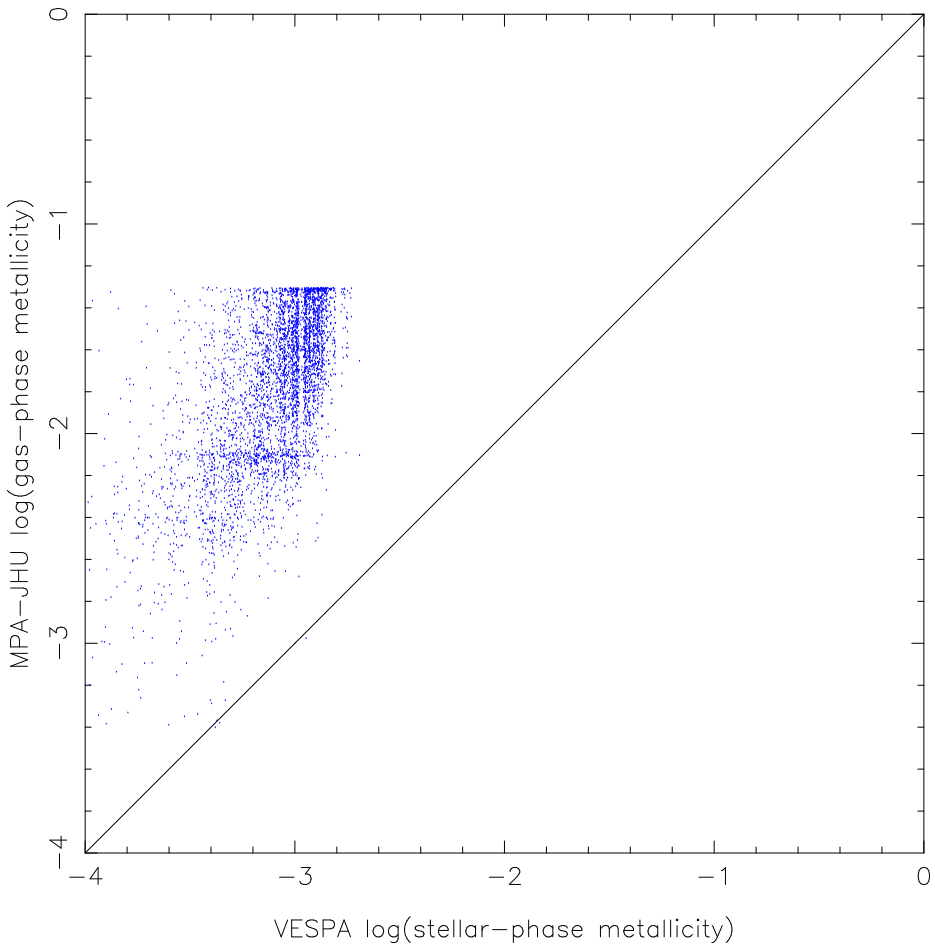

Figure 4.15: Comparison between VESPA stellar-phase metallicities and MPA/JHU gas-phase metallicities. Since gas-phase metallicity does not usually equal stellar-phase metallicity, it is not expected that the distribution of points will follow the diagonal line.

Chapter 5

Bulge/Disk Decompositions & SN Ia Light Dependence

Having investigated the correlation between supernova rates and M and SFR properties of the host galaxies, we proceed to probe the distribution of SNe within the host galaxy, and compare it with the distribution of light. This is important for two reasons.

First of all, although investigating A+B-like models gives a good picture of how certain galaxy properties correlate with the galaxy SNR, it does not specify *why* they are correlated. Since many properties (notably mass and SFR) have different distributions within galaxies, knowing how SNe are distributed within the host galaxies may provide a better understanding of whether it is possible these components intrinsically give rise to SNe Ia.

Secondly, different stellar populations could also have different contributions to SNR. If the progenitor systems of SNe happen to involve certain stellar populations which have a very distinct spatial distribution within the host galaxy, then investigating the spatial distribution of SNe may provide a clue as to what the progenitor population might be.

In the past, it has been suggested that SNe show a concentration in the spiral arms of spiral galaxies (Della Valle & Livio 1994), but subsequent research showed that this trend did not hold for V- and I-band observations (McMillan & Ciardullo 1996). This suggests that SNe arise from a redder population, but otherwise has no further implications as to how SNe are spatially distributed in relation to host light. It was not until much later that Kelly et al. (2008) adopted the methods of Fruchter

et al. (2006), and showed that SNe distributions more or less conform to the total galaxy light. They calculate the "fractional flux" contained within each individual SN as

$$\text{fractional flux} = \frac{\Sigma_{\text{within isophote at SN position}}\text{ADUs in pixel}}{\Sigma_{\text{galaxy}}\text{ADUs in pixel}}, \qquad (5.1)$$

and plot the cumulative distribution of SNe as a function of this fractional flux (see Figure 5.2). Theoretical work has been attempted to reproduce this distribution, with some success (Raskin et al. 2008, who modelled the SNR of spiral galaxies under the assumption of the A+B model by Sullivan et al. 2006).

For our work, we adopt methods similar to Kelly et al. (2008), but with the data from Simard et al. (2011), we are able to investigate how SN spatial positions are related to the light of bulge and disk components of the host galaxy.

This work is done in two steps: first, we reconstruct the equivalent circularly symmetric radial profiles from the parameters obtained by Simard et al. (2011), and second, we compare these profiles with the positions of the SNe being hosted. A total of 78 SNe and their hosts were found to be available for this study.

5.1 Galaxy Light Profile Reconstruction

Simard et al. (2011) characterize the galaxy radial light profiles via a number of parameters, among which are:

r_e, the bulge half light radius along the major axis of the bulge,

e, the "ellipticity" of the bulge, defined as $e = 1 - \frac{b}{a}$ (note that e is not eccentricity)

n, the Sérsic index of the bulge.

r_d, the disk scale radius along the major axis of the disk,

i, the inclination of the disk, with $i = 0$ meaning that the disk is viewed face-on,

b_t, the bulge-to-total light ratio, which we will denote as b_t.

Also available for every galaxy are the redshifts (mostly photometric, spectroscopic where available) and r-band apparent magnitudes, which are also used for our study.

To compare the spatial distribution of SNe with the host light distribution, it is necessary to convert the elliptical profiles to an equivalent circularly-symmetric radial profile. Since r_e and r_d were quoted along the major axes of their respective components, we make the conversion by multiplying these figures with $\sqrt{\frac{b}{a}}$, where a and b are the semi-major and semi-minor axes of the elliptical profile, thereby

assuming that the equivalent radius of an ellipse is $\sqrt{ab}$. For the bulge, the "ellipicity" e is given, therefore we multiply r_e by $\sqrt{1-e}$. Note the definition of ellipticity as described above is $e = 1 - \frac{b}{a}$, and is not to be confused with eccentricity. For the disk, it is assumed that all disks are intrinsically circular when viewed face-on, and that any ellipticity is induced by its inclination. Thus, we multiply r_d by $\sqrt{\cos i}$. For the rest of this paper, any reference to the symbols r_e and r_d will signify these corrected definitions.

Having obtained parameters for an equivalent circularly symmetric 2D light profile, we next convert it into a 1D profile, for an easier comparison to the distance from the hosted SN in the galaxy. For the disk, the annulus at a distance of R away from the galaxy centre should contain an amount of luminosity equal to

$$2\pi R(I_0 e^{(-\frac{R}{r_d})})dR. \tag{5.2}$$

Since the total luminosity of the disk is equal to

$$\int_0^{+\infty} 2\pi R I_0 e^{(-\frac{R}{r_d})} dR = 2\pi I_0 r_d^2, \tag{5.3}$$

dividing the two yields

$$\frac{R}{r_d^2} e^{(-\frac{R}{r_d})}, \tag{5.4}$$

which is the fraction of disk luminosity in a circular annulus of width dR at radius R. Likewise, for the bulge, the luminosity contained within an annulus at R is equal to

$$2\pi R(I_0 e^{-(\frac{R}{a})^{\frac{1}{n}}})dR, \tag{5.5}$$

and the total bulge luminosity is equal to

$$\begin{aligned}\int_0^{+\infty} 2\pi R I_0 e^{-(\frac{R}{a})^{\frac{1}{n}}} dR &= 2\pi I_0 a^2 \int_0^{+\infty} x e^{-x^{\frac{1}{n}}} dx \\ &= 2\pi I_0 a^2 \int_0^{+\infty} x^n e^{-x} (dx^n) \\ &= 2\pi I_0 a^2 \int_0^{+\infty} x^n e^{-x} (n x^{(n-1)} dx) \\ &= 2\pi I_0 a^2 \cdot n \int_0^{+\infty} x^{2n-1} e^{-x} dx \\ &= 2\pi I_0 a^2 \cdot n\Gamma(2n);\end{aligned} \tag{5.6}$$

dividing the two gives the fraction of bulge luminosity in a circular annulus of width dR at R, which is

$$\frac{R}{a^2} \frac{1}{n\Gamma(2n)} e^{(-\frac{R}{a})^{\frac{1}{n}}}, \tag{5.7}$$

where a is the disk scale radius, which can be expressed as a function of r_e and n. According to Ciotti & Bertin 1999, a good approximation to this function is:

$$a = \frac{r_e}{b^n(n)}, \tag{5.8}$$

where

$$b(n) = 2n - \frac{1}{3} + \frac{4}{405n} + \frac{46}{25515n^2} + \frac{131}{1148175n^3} - \frac{2194697}{30690717750n^4} + O(n^{-5}), \tag{5.9}$$

which is an approximation we adopt for our calculations to save computing time. The nature of this approximation renders it unreliable for small n ($n \lesssim 1$), but it is generally expected that a bulge would not have a Sérsic index this small, and in any case we exclude such galaxies from our sample, as explained below. For the values of n that we are concerned with, this approximation is accurate to at least 6 significant digits (returning a value of 1.0000025 for $\Gamma(2)$, and 2.00000024 for $\Gamma(3)$, for reference). Thus, for any given SN, the percentage of total host luminosity contained within its position can be found by integrating Equations 5.3 and 5.6.

Now that we have the normalised ($I_0 = 1$) light profiles of the bulge and disk respectively, we need to obtain the total light profiles as well. This is done via the

parameter b_t, which, as explained above, is the bulge-to-total light ratio. We weight bulge light profile by b_t, the disk light profile by $1 - b_t$, and add the weighted profiles together for all galaxies to obtain the total light profiles (abbreviated as "galaxy profile").

Lastly, we exclude the galaxies in the Simard et al. (2011) sample which have a bulge Sérsic index smaller than 2, leaving a remaining sample of 81331 of the original 101978. This is primarily due to the fact that there are several instances where a Sérsic index smaller than 1 was obtained for the bulge, implying each time that the fitting algorithm malfunctioned for that specific galaxy, for it is generally expected that bulge Sérsic indices are larger than 2. Although there exist exotic phenomena known as "pseudobulges" (eg. Fisher & Drory 2010), where the Sérsic index can be very small ($\lesssim 2$), it is known that these abnormal bulges have different properties in comparison to the better-understood classical bulges (eg. Kormendy et al. 2011), and we do not wish to introduce complications to our analysis that could arise as a result of including them. This Sérsic index cut also eliminates the small Sérsic index algorithm divergence problem with the approximations of Ciotti & Bertin (1999), as explained above. No biasing effects are introduced into the resulting SN sample distribution, as by dropping all $n < 2$ galaxies, we also automatically drop any potential hosted SNe.

5.2 Light Dependence of SNR

Intuitively, one would expect the spatial distribution of SNe to approximately follow the spatial distribution of host galaxy light. Previously, it was investigated whether or not this is the case for SDSS SNe (Kelly et al. 2008), and also studied via theoretical work (eg. Raskin et al. 2008).

For the next paragraph alone, we drop the afore-mentioned convention of "SNe" referring to SNe Ia by default. "SNe" shall instead mean SNe of all types unless otherwise specified.

Kelly et al. (2008) matched a sample of SNe to potential host galaxies in the SDSS photometric sample using very stringent criteria, resulting in SNe only within the g-band 25 mags/arcsec^2 isophote being matched. They then calculate what fraction of light is included within the isophote passing through each SN, using elliptical annuli, and plot their results in a way pioneered by Fruchter et al. (2006), which we also adopt. They found that the SNe Ia were noticably more centrally concentrated than the light profile of the galaxy, with KS tests easily rejecting a match by $\sim$99%.

Lacking further information and unable to effectively correct for seeing effects (the seeing was $\sim 1''$, about the size of the isophote), the authors did not investigate this phenomena further, commenting only briefly that SNe Ia follow light better than SNe Ib and Ic.

In our investigation, we have decomposed bulge/disk components from Simard et al. (2011), which are reliably corrected for seeing effects via GIM2D (see Chapter 2). This allows us to probe the issue in more detail.

After applying the Sérsic index cut (as mentioned in the last section) to the Simard et al. (2011) galaxy sample of 1.12 million objects (see Chapter 2 for details), 81331 entries remain. As mentioned before, we search these remaining 81331 galaxies for hosts which were previously matched to SNe via our $R_{25} = 3.8$ matching method. We find a total of 78 matches (see Table 5.1).

Table 5.1: Raw data for sample of 78 SN Ia hosts for studies of the SN Ia spatial distributions.

D_{SN}	m_r	z	b_t	r_e	n	r_d
4.49284799	15.45	0.1164	0.51	5.05620112	4.194	11.4773384
3.97710421	16.74	0.0466	0.121	2.63345006	3.976	4.26169413
5.06711041	14.37	0.0407	0.67	6.90283785	3.877	11.931458
0.298767168	17.8	0.087	0.234	2.92821201	5.776	2.20946167
0.6167574	17.21	0.067	0.068	2.82166453	4.284	5.05949685
2.6864838	17.02	0.1369	0.162	3.13457287	3.769	3.51713438
6.54694441	16.83	0.0768	0.355	9.7216	2.703	3.47078306
0.26155781	16.93	0.175	0.356	4.07325739	7.805	6.90030553
7.16659621	17.68	0.1655	0.677	2.21896847	2.373	4.9909473
12.4020948	17.24	0.2107	0.534	4.90569981	4.007	9.67275222
3.7813986	17.46	0.1287	0.51	3.72698328	2.752	3.08449702
5.8651272	16.79	0.034	0.279	8.21002711	2.624	8.67544846
2.9547444	17.34	0.1615	0.882	3.43978463	5.239	5.2699526

Continued on Next Page...

Table 5.1 – Continued

D_{SN}	m_r	z	b_t	r_e	n	r_d
1.381263	16.95	0.105	0.294	3.05026692	4.522	3.77840993
10.936407	17.21	0.1393	0.227	6.43713874	2.773	4.79985702
3.82764719	17.81	0.1749	0.699	2.19100639	4.52	5.1442591
0.27144582	17.29	0.0628	0.447	3.56378573	3.605	5.82973519
1.049046	17.46	0.1191	0.409	3.66796236	4.452	1.52491994
1.7629686	17.29	0.136	0.016	3.75466364	4.304	3.67833301
0.738548399	17.7	0.1318	0.963	4.154122	6.579	2.28641261
7.9264674	17.82	0.183	0.649	0.608971702	6.67	7.6339841
5.88551101	17.73	0.1181	0.196	5.7988	5.159	3.32304562
5.21291819	16.49	0.0843	0.487	2.89055835	5.201	6.09556879
5.388948	17.82	0.2353	0.362	0.991048748	6.565	4.60454874
6.691761	17.46	0.1474	0.239	6.65888535	4.029	5.13306686
0.7726914	17.88	0.1465	0.951	2.31615539	3.646	1.14232074
7.81091219	17.01	0.1294	0.986	6.49841962	5.655	4.13444801
2.7432732	17.49	0.167	0.512	2.41232841	4.817	2.75055264
6.6536838	16.43	0.0799	0.178	8.82549205	7.101	9.87033048
4.36929901	17.64	0.1993	0.456	3.36405941	4.219	3.70556654
5.86786259	14.3	0.0591	0.346	12.0906011	7.968	21.3335548
7.83206399	16.84	0.1046	0.983	6.41328934	5.322	4.0111032
4.0363164	17.68	0.1813	0.307	2.73068352	7.977	7.31225459
5.34598859	17.02	0.1309	0.201	3.70744825	4.56	3.39934393
0.966807601	16.45	0.1184	0.836	7.80883293	7.855	9.40707545
1.397295	17.66	0.0826	0.311	2.69808132	4.509	3.39734846
11.261589	16.45	0.1191	0.949	10.2268235	7.182	5.92078275
6.46877999	16.35	0.0796	0.913	4.07301363	5.998	5.05520531
1.2698178	17.09	0.115	0.414	2.54846475	2.116	5.21996889
3.427716	17.31	0.1318	0.918	2.54910078	3.339	6.29106577
0.0726712409	17.63	0.0579	0.613	1.21818024	6.436	3.10313762

Continued on Next Page. . .

Table 5.1 – Continued

D_{SN}	m_r	z	b_t	r_e	n	r_d
0.412520926	16.47	0.0653	0.874	1.99097001	6.931	5.43752796
0.413019508	17.94	0.1988	0.667	2.32885515	3.697	4.34145798
9.54115261	18.15	0.146	0.98	2.6148472	6.725	1.27970805
2.6338164	17.97	0.2064	0.188	0.402518509	5.505	4.81253866
2.2384572	16.6	0.089	0.947	7.96051354	3.386	7.30272258
1.126575	18.01	0.1072	0.357	2.22748321	3.984	2.80859298
2.4756726	16.47	0.0865	0.297	1.5305074	6.79	6.91951213
0.254276815	17.94	0.0713	0.944	2.49942663	3.994	3.19525587
2.8991502	18.01	0.1894	0.979	3.53392826	6.306	2.55124665
2.202888	16.97	0.1076	0.711	3.03433662	4.812	4.53679983
2.8609038	17.72	0.1307	0.961	3.2512095	4.771	1.59659563
0.113686707	17.22	0.1021	0.365	2.00916125	6.112	5.36696452
1.4651856	17.18	0.0935	0.462	2.78506984	5.145	3.36812776
13.8466344	16.68	0.0797	0.076	7.94986717	3.455	7.37348983
2.5907904	18.06	0.1447	0.022	7.92495594	5.846	3.28581949
0.163386588	17.48	0.1197	0.4	1.1003595	4.497	5.22335104
0.107942347	18.	0.1664	0.545	2.51833739	4.285	3.27005395
4.59252241	18.03	0.3249	0.923	6.65804912	4.624	0.038261195
0.777357	18.06	0.1232	0.544	1.85091006	4.166	3.48444473
2.2331094	17.	0.1299	0.838	4.08075202	6.689	5.32249832
0.348144977	17.2	0.0719	0.174	0.852264403	4.65	2.20998543
6.66355259	16.6	0.1043	0.164	4.43525499	4.522	6.05768778
4.01219039	18.06	0.0902	0.488	6.45563129	3.924	1.97992297
2.9427246	17.95	0.2577	0.175	5.75060866	6.781	6.02040236
1.3571208	17.91	0.1072	0.959	2.06345016	5.479	2.6317477
2.1280224	15.77	0.0454	0.225	2.34165893	5.038	4.4339566
5.3619462	16.22	0.1241	0.23	4.01293696	6.03	8.05512963
0.219688689	16.47	0.0381	0.782	2.29156239	3.464	5.5691085

Continued on Next Page. . .

Table 5.1 – Continued

D_{SN}	m_r	z	b_t	r_e	n	r_d
0.400873064	17.91	0.1246	0.04	2.24260812	5.05	3.18215666
4.51202339	17.25	0.0664	0.493	1.5504592	5.915	11.8121255
3.81619559	18.03	0.2375	0.26	2.34462509	4.823	2.85348078
1.8944916	17.84	0.243	0.439	1.20923558	4.25	2.15628838
7.44862381	16.15	0.1064	0.418	0.554155097	5.295	6.48824852
0.254388682	17.99	0.1664	0.986	2.12266753	7.678	0.096372693
18.3827514	14.48	0.013	0.044	5.95757826	3.438	21.90396
0.7185816	18.11	0.1604	0.474	2.39029672	3.557	2.96133664
9.2950614	15.12	0.0459	0.176	9.1424813	4.861	10.7619182

D_{SN}, m_r, z, b_t, r_e, n and r_d are the angular distance to the SN, r-band apparent magnitude, redshift, bulge-to-total light ratio, bulge half-light radius, bulge Sérsic index and disk scale radius respectively.

For each of these SNe, we integrate the galaxy light according to our 1D galaxy profiles out to the distance of the SNe, and take this amount of light to be that included in the SNe (L_{inc}). We also integrate the galaxy profiles out to a distance of $3.8R'_{25}$, where $R'_{25} = \sqrt{a'b'}$, a' and b' being the semimajor and semiminor axes of the r-band 25 mag/arcsec^2 isophote, and take this to be the accessible light of the galaxy (L_{acc}). L_{acc} is used in place of the actual total light of the galaxy when calculating the percentage of light included in each SN. This is due to the fact that our host matching method excluded SNe further than $R_{25} = 3.8$, and therefore would have introduced a bias had we used the actual total light. Dividing the two, we obtain

$$\% \text{ light included} = 100 \times \frac{L_{inc}}{L_{acc}}, \tag{5.10}$$

which is representative of the percentage of galaxy light found within the SN. This is done for all 78 SN-host pairs, and a cumulative histogram of number of SNe is

plotted as a function of the "% light included" as calculated above. Note that this process is done for only the 78 SN-host pairs found, and makes no use of the remaining galaxies in the 81331 galaxy sample. This process is repeated for the bulge and disk light respectively, and the 3 lines are shown in Figure 5.1 (red for bulge, green for the sum of bulge light and disk light, blue for disk). A 45° diagonal line is drawn in comparison, which would be what the histogram should converge to if SNe were to follow the light of that specific component. KS tests show that the cumulative histograms for the disk and total light are rejected at ∼99% confidence, while that of the bulge component is not.

However, the green curve in Figure 5.1 does not agree well with the corresponding curves obtained from the literature (Kelly et al. 2008, Raskin et al. 2008, see Figure 5.2). This prompts us to plot the same diagram with an $R_{25} = 1$ cut, which would make it consistent with the annulus cuts made by Kelly et al. 2008, since all their sample SNe are within the 25 mags/arcsec^2 isophote. Thus, we match hosts with SNe using the $R_{25} = 1$ criteria, obtaining 44 matches, and repeat the plotting process above, taking L_{acc} to be the light within R'_{25}. The resulting plot is shown in Figure 5.3, again with the green line representing galaxy light, and the red and blue lines corresponding to bulge and disk light respectively. The corresponding green line (galaxy light) agrees much better with the literature than Figure 5.1. The galaxy total light cumulative distribution is not rejected by the KS test, being rejected at only 43% confidence level, partly due to the lack of a sufficient number of data points, partly due to the fact that within $R_{25} = 1$, the bulge light is much more dominant than within $R_{25} = 3.8$.

To illustrate and compare where the regions hosting SNe and light lie within the galaxy itself, we plot a differential distribution of bulge, galaxy, and disk light vs physical distance in kpc from the centre of the galaxy, and overlay a histogram depicting the percentage of SNe over it. The plotting of the galaxies is done in 3 steps. First, we take each galaxy within the Simard et al. 2011 sample which meets our Sérsic index cuts (81331 in total), and calculate its relative luminosity L_{rel}, a quantity which is proportional to luminosity. Luminosity can be calculated as follows:

$$L = F \cdot D_L^2 \tag{5.11}$$

where D_L is the luminosity distance, and F is the flux received by the observer. Since, at low redshifts,

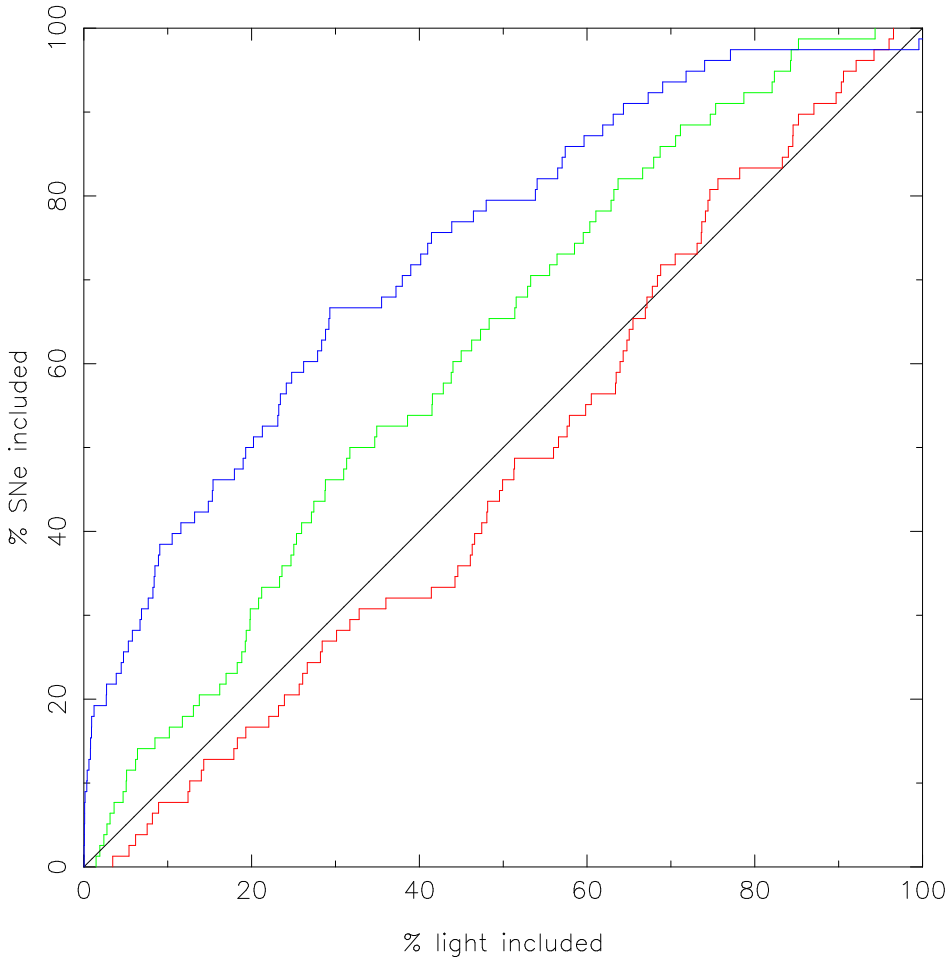

Figure 5.1: Comparison between SN positions and galaxy light distribution out to 3.8 times the equivalent radius of the 25 mags/arcsec^2 isophote, corresponding to $R_{25} = 3.8$. The x-axis is the percentage of light contained within the SN, the y-axis is the cumulative percentage of SNe. The red, blue and green lines correspond to bulge, disk and total light of the host galaxy respectively. All 78 SNe were applicable for this plot. Compare with Fig. 2 of Kelly et al. (2008).

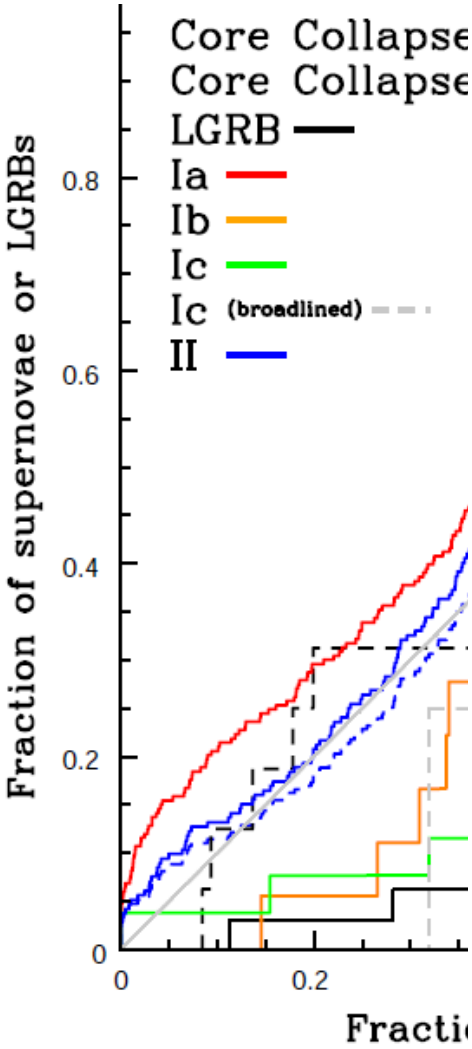

Figure 5.2: Comparison between SN positions and galaxy total light spatial distributions, taken from Kelly et al. (2008).

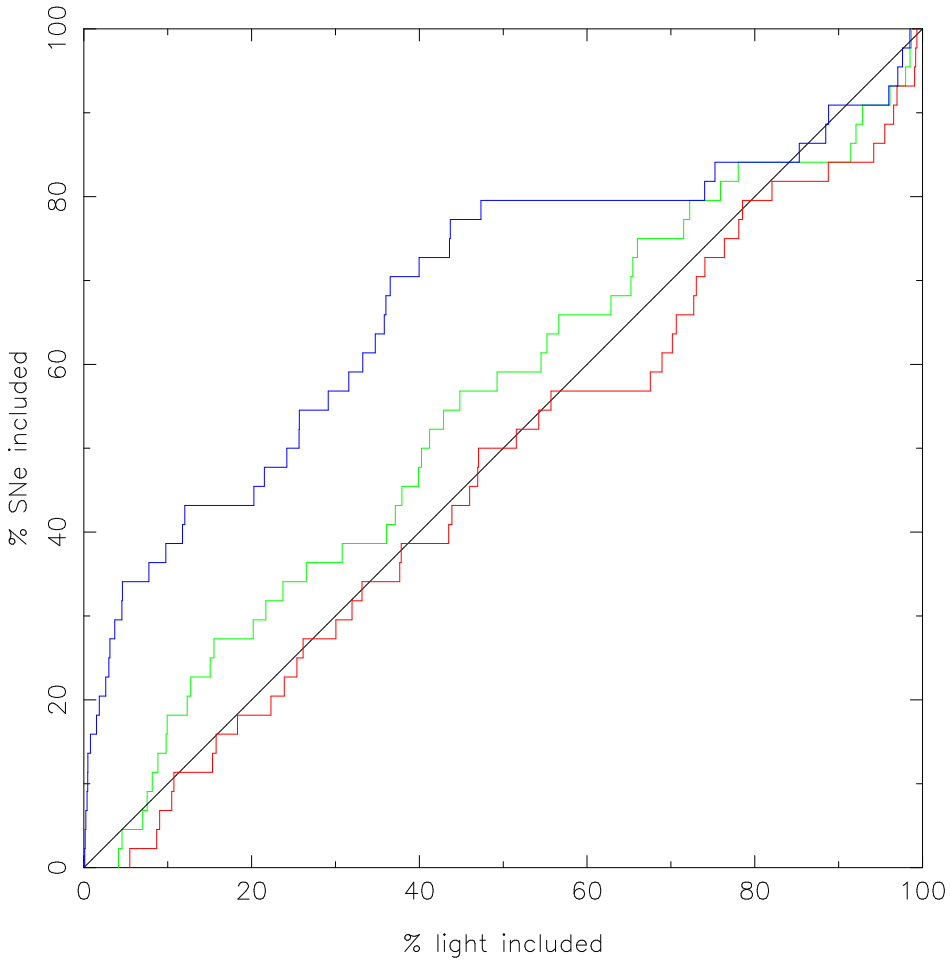

Figure 5.3: Similar to Figure 5.1, only that the comparison is extended out to an equivalent radius corresponding to $R_{25} = 1$. A total of 44 SNe were applicable for this plot.

$$\begin{aligned} -2.5\log F &\propto m_r, \\ D_L &\propto z, \end{aligned} \tag{5.12}$$

where m_r is the r-band apparent magnitude of the galaxy in question, and z is the redshift, we define L_{rel} to be

$$L_{rel} = 10^{-\frac{2}{5}m_r} z^2, \tag{5.13}$$

such that L_{rel} is proportional to the total light of the galaxy. Second, we weight the galaxy total light profiles of each galaxy by L_{rel}, the bulge profiles by ($b_t \times L_{rel}$, and the disk profiles by $(1 - b_t)L_{rel}$, and sum them to obtain the 3 respective summed profiles. Third and last, we normalize all 3 summed profiles such that the total light within 30kpc (the range of the plot) equals 1. All SNe found to be within 30 kpc of their host galaxies are binned into 15 bins, and the number in each bin is then divided by the total number of SNe found withn 30kpc. The resulting plot is shown in Figure 5.4, again with red for bulge, green for galaxy and blue for disk. It is apparent that bulge light (red) matches the SN distribution better than any other component. The rationale behind plotting this only out to 30kpc is that a sharp break in the number of SNe matched is observed just beyond this distance, hinting that our matching algorithm cuts off most matches beyond this value.

We next plot two figures analogous to Figure 5.1, this time using only those galaxies which have $b_t \leq 0.5$ and $b_t > 0.5$ respectively. These figures are shown in Figures 5.5 top and bottom respectively, where it can be seen that the galaxy cumulative distribution (green line in top figure) for disk-dominated galaxies deviate further from the 45° line than their bulge-dominated counterparts (green line in bottom figure), further supporting our previous findings that SNe formation follows bulge light better than disk light. However, worthy of note is the fact that a majority (45 out of 78) of the SNe used in our analysis were hosted by galaxies with $b_t \leq 0.5$, even though the summed bulge to total light ratio of both the host sample and the 81331 complete galaxy sample is very close to 0.5, and there is no significant dominance of $b_t \leq 0.5$ galaxies in the 81331 galaxy sample (see Table 5.2 for details). This shows that SNe do not preferentially occur in bulge-dominated galaxies, and hints that it is not intrinsically a population which exclusively exists in the bulge that is responsible for SNe, even though the SNe seem to follow the bulge light. The implications of this

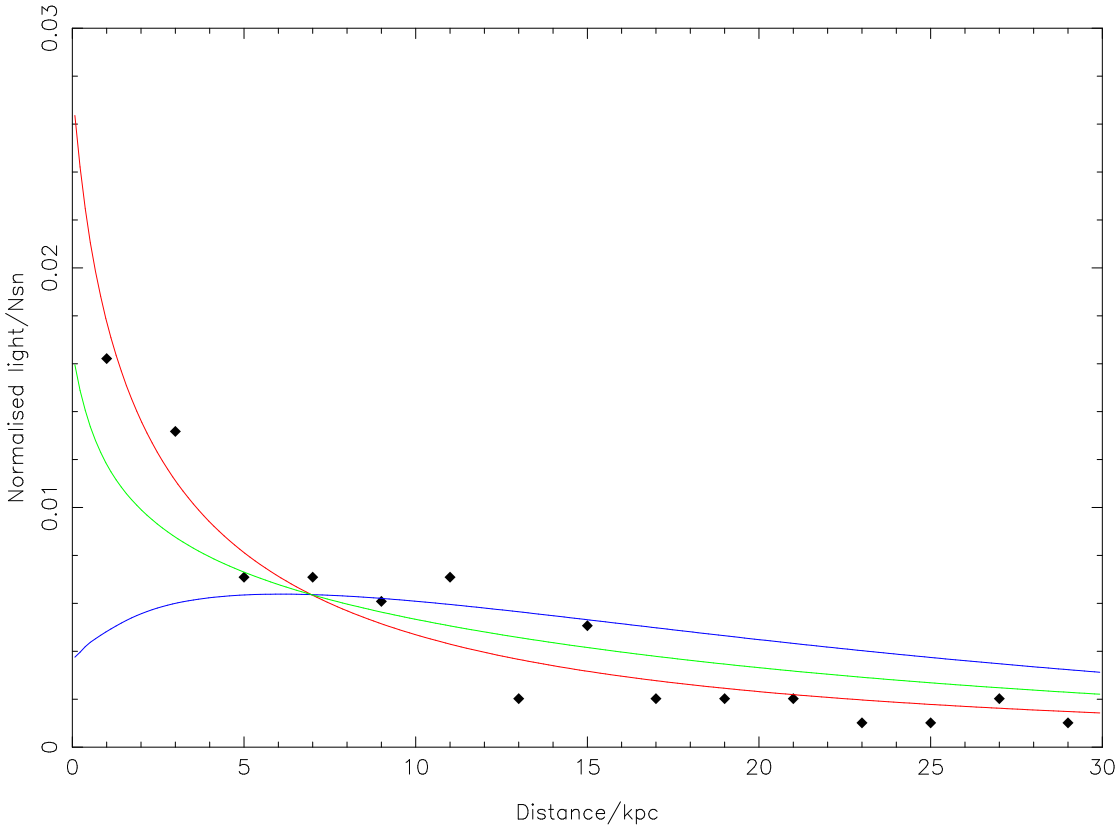

Figure 5.4: Fractional differential distributions of bulge (red), disk (blue) and total (green) galaxy light within a physical distance of 30 kpc from the centre of the galaxy. Plotted for comparison is the fractional distribution of SNe (black diamonds). It can be seen that the SNe follow bulge light much better than that of any other component, as suggested by our previous KS tests. The SN data points have been scaled down by a factor of 15/200 to account for the fact that there are 200 bins for the galaxy light profiles and only 15 bins for the SNe.

Table 5.2: The "81331 Sample" refers to the galaxies in the Simard et al. (2011) catalogue which remain after applying Sérsic index cuts as explained in the text. The "78 Sample" refers to the 78 elements of those 81331 which have hosted SNe. "Relative Luminosity" is L_{rel}, a quantity that is proportional to luminosity, and explained in detail in the text.

Quantity	81331 Sample	78 Sample
Number of Disk-Dominated Entries ($L_{Bulge} \leq L_{disk}$)	41822	45
Number of Bulge-Dominated Entries ($L_{Bulge} > L_{disk}$)	39509	33
Ratio of Disk- to Bulge-Dominated Entries	1.06	1.36
Amount of Relative Luminosity Contained in Disk	1288011	859
Amount of Relative Luminosity Contained in Bulge	1336031	872
Ratio of Disk Light to Bulge Light	0.96	0.98

finding are further debated in the discussion.

Then again, it is entirely possible that light from the bulge and disk components intrinsically are not equal in their contribution towards SN progenitors in the first place. It is generally not expected that bulges and disks have the same mass-to-light ratios, which would result in a different mass contribution despite having the same amount of light. Also, the rate of specific SFR in different bulges can vary dramatically in comparison to the disk (e.g., Fisher et al. 2009). Thus, if we take mass and star formation to be intrinsically responsible for SNe, it makes sense to hypothesize that the disk light has a correlation to the SN position, such that the positions of the SNe follow a distribution of $B + \epsilon_D D$, where B is the bulge light, D is the disk light, and ϵ_D is some constant factor smaller than 1. We ask the question of how large could ϵ_D be before the model is rejected. We find that at $\epsilon_D = 0.3$ (Figure 5.6), the model (green line) is rejected by the KS test at the 90% confidence level, meaning that if the degree to which SNe follow a certain light component could be interpreted as the contribution to SNR of that specific component, then the disk contribution is at most one-third that of the bulge.

We attempt to reconcile our result for ϵ_D above with the generic A+B model. Unfortunately, since the mean mass-to-light ratios and SFRs of our sample is poorly understood, we are unable to predict how the relative luminosities of the bulge and disk contribute to mass and SFR. To remedy this problem, we take our spectroscopic host sample of 19987 galaxies, match them to our 81331 galaxy sample, and obtain a subset of 16289 galaxies for which mass, SFR, bulge light, and disk light are all

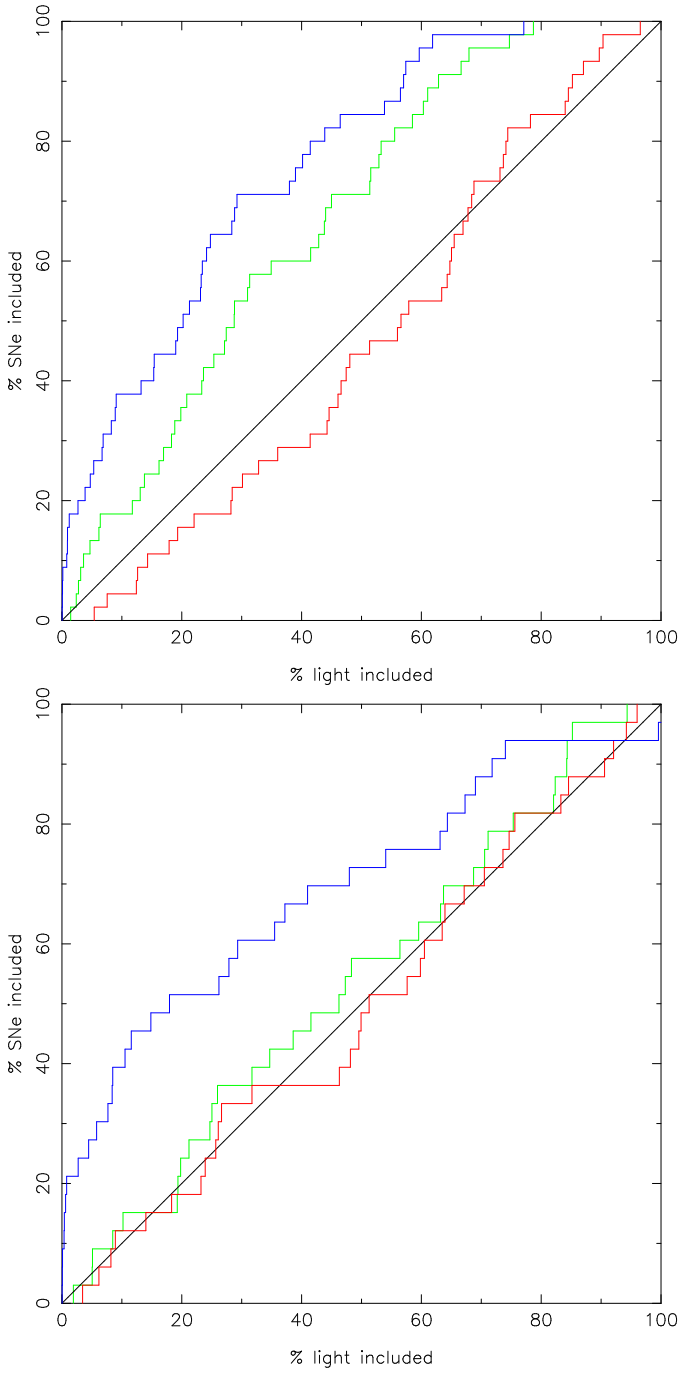

Figure 5.5: Comparisons between SN positions and galaxy light distribution out to the equivalent radius of $R_{25} = 3.8$. Compare with Figure 5.1. The figure at the top is plotted with the 45 hosts with a bulge-to-total light ratio smaller than or equal to 0.5, while the figure at the bottom is plotted with the 33 hosts with a bulge-to-total light ratio greater than 0.5.

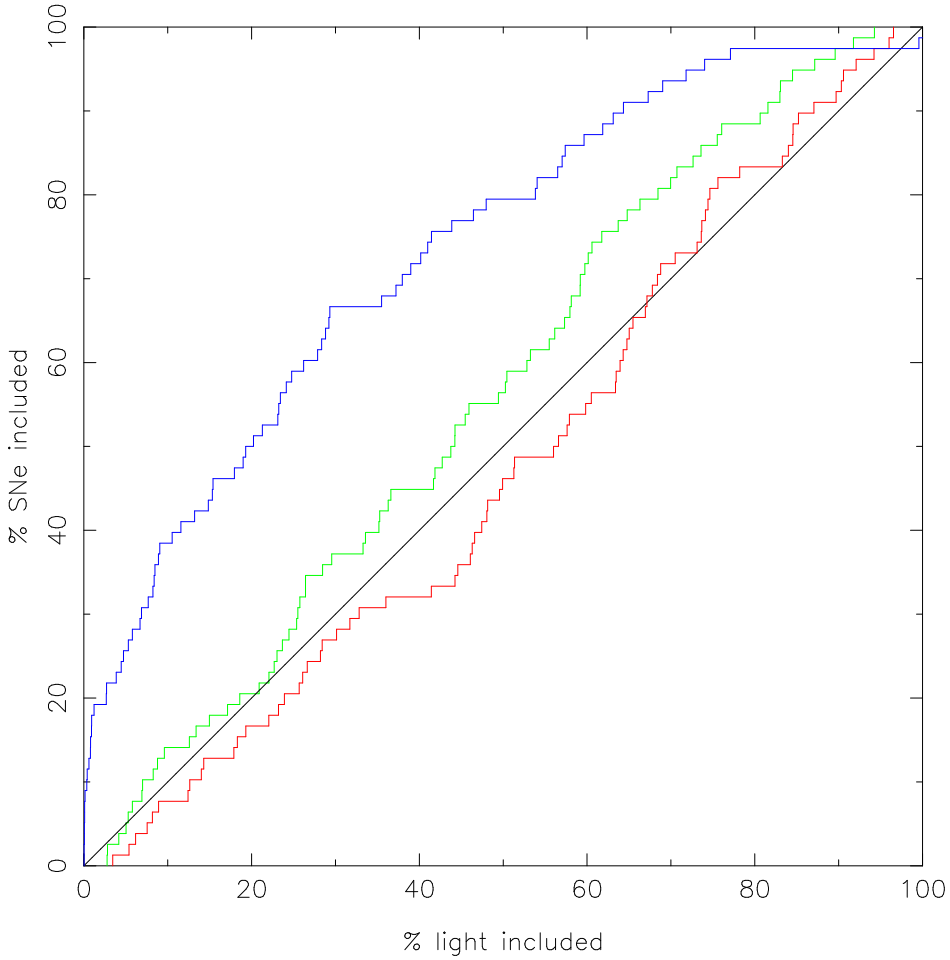

Figure 5.6: Comparisons between SN positions and galaxy light distribution out to the equivalent radius of $R_{25} = 3.8$, where red is the bulge light, blue is the disk light, and green is a weighted sum of the two, $B + \epsilon_D D$, where B is the bulge light, D is the disk light, and ϵ_D is taken to be 0.3 for this plot. When a KS test is applied to the green line, with the 45° straight black line as the theoretical distribution, it is rejected at 90% confidence.

known. From this new sample, we retrieve a linear relation between mass, SFR, bulge light, and disk light:

$$M = P_1 \cdot L_{B,rel} + Q_1 \cdot L_{D,rel}, \tag{5.14}$$

$$SFR = P_2 \cdot L_{B,rel} + Q_2 \cdot L_{D,rel}, \tag{5.15}$$

where P_1,P_2,Q_1 and Q_2 are constants to be determined. A least-squares fit results in

$$M = 5.6^{+2.1}_{-1.6} \times 10^{19} M_\odot \cdot L_{B,rel} + 4.3^{+4.0}_{-2.5} \times 10^{19} M_\odot \cdot L_{D,rel}, \tag{5.16}$$

$$SFR = (-0.25)^{+2.15}_{-1.45} \times 10^9 \cdot M_\odot / yr L_{B,rel} + 2.0^{+1.6}_{-1.7} \times 10^9 M_\odot / yr \cdot L_{D,rel}. \tag{5.17}$$

From this very crude treatment, it can be seen that, if we take our best-fit values, the contribution of bulge light to SFR is negligible, while its contribution to mass is about equal to disk light. Since the total $L_{B,rel}$ and $L_{D,rel}$ are about equal for our sample, and the contribution of the A and B terms of the A+B model have roughly equal contributions to SNR, we conclude that the ϵ_D in $B + \epsilon_D D$ should be significantly larger than 1 if the A+B model could predict SN intragalactic spatial distributions. Even taking the large error bars into account, it would be unlikely that the disk dominates significantly over the bulge in terms of contribution towards mass or SFR, which is required to bring ϵ_D down to 0.3. Hence, our results are not compatible with a generic A+B model.

Finally, we test if it is possible to explain the central SN spatial concentration in our data by assuming that SNe follow a power law of the disk light. There is at least one possible explanation why this might be the case, as follows. According to the Schmidt-Kennicutt law (see Kennicutt 1998), the spatial distribution of SFR follows the molecular gas density to some power

$$\Sigma_{\rm SFR} = k \Sigma^{\Gamma}_{\rm gas}, \tag{5.18}$$

where k and Γ are constants. When $\Sigma_{\rm gas}$ is presented in units of $M_\odot pc^{-2}$, $\Gamma = 1.4 \pm 0.15$. Thus, if we take disk light to be a proxy for molecular gas density, SFR (and hence SNR) should follow disk light to the power of Γ. Thus, we create profiles for disk light to the power of some number τ, and perform the KS tests above. Mathematically, this is identical to dividing the disk scale length by a factor of τ.

The results are that, to obtain a degree of rejection as low as 90% confidence, τ needs to be as large as 2.4 (see Figure 5.7). In other words, for the above Schmidt-Kennicutt law interpretation of our results to be valid, the lower limit for Γ is 2.4.

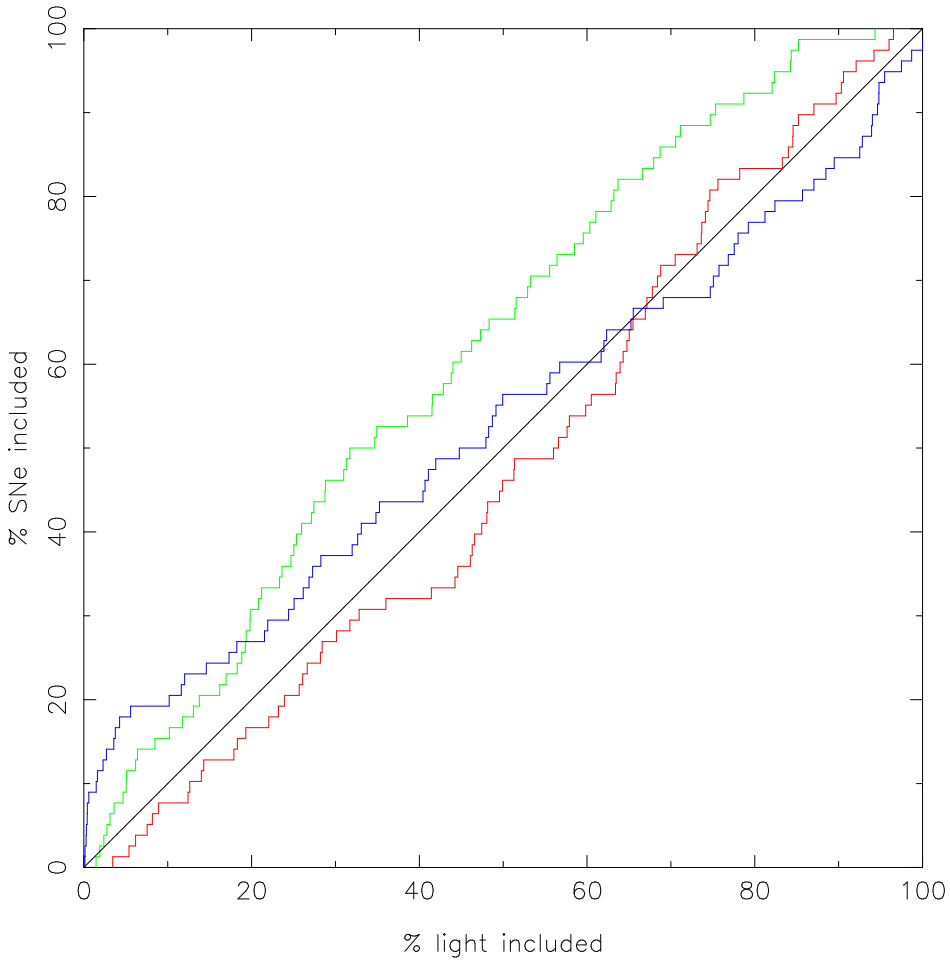

Figure 5.7: Comparisons between SN positions and a disk luminosity to the power of τ profile (blue line), where $\tau = 2.4$. This is the minimum τ required for the green line not to be rejected at 90% confidence. Also shown for comparison are the bulge profile (red), and the galaxy total light profile (green).

Chapter 6

Discussion & Conclusion

6.1 Supernova Ia Rates as a Function of Mass and Star Formation Rate

One of the two main tasks of this work was to obtain the most reliable values of the parameters of the "A+B" model to date. We obtained these best-fit values, but then found that no value for A and B could possibly match our data well. We assembled a series of alternate models we constructed ourselves, as well as a few established models from the literature, and subjected them to tests via our data. During the description of this process in Chapters 2, 3 and 4, a few controversial issues remained unaddressed. The following few paragraphs in this section address these issues, and also offer an interpretation of the results.

For any magnitude-limited survey (a survey which can only observe objects above a fixed apparent magnitude) such as the SDSS, faraway luminous objects can be seen, while less intrinsically objects at the same distance may not. This leads to a bias in which more luminous objects are sampled more heavily in proportion to the total population, resulting in apparent demographics which have a higher proportion of luminous objects than actually exist. To correct for this bias, one must weight every observed object by $1/V_{acc}$, where V_{acc} is the theoretical "accessible" spatial volume of the observation within which the object can be observed, given its absolute magnitude. As mentioned above, we apply no $1/V_{acc}$ weighting to the spectroscopic galaxy and SNe Ia samples when we make the A+B fits, instead taking a cut at z=0.25 for the spectroscopic galaxy sample. Thus, for the A+B fits, our data contain a spectroscopic galaxy sample which is demographically biased in terms of luminosity

function and large-scale spatial distribution. Our justification for this is that while the host sample may not be representative of the general population of galaxies in the universe, the host sample and the SN sample are complete with respect to each other. As long as it is assumed that the parameters of the various SNR models deployed are independent of both the luminosity of the host and the spatial positioning of the potential host population, it can be concluded that this treatment is reasonable.

Since the highest-redshift SN in our sample has a redshift of 0.23, one may argue that our redshift cut of 0.25 is too high. To test the robustness of this redshift cut, we make the same computations with a redshift cut at z=0.2, eliminating 1000 galaxies from our spectroscopic sample, along with 2 SNe. This leads to no significant difference in our results (see Figure 6.1 for the resultant differential distribution of SNR, and compare with Figure 4.3). Also, other authors (e.g., Smith et al. 2011) take the reshift cut to be 0.25 for the same sample, further validating our choice.

It is true that our simplified treatment of the observation windows and very complicated detection efficiency function of the SDSS II SN Survey could affect the absolute values of our A and B measurements (and also those of the C parameter for later models) by a certain factor. We assume a constant homogeneous efficiency independent of redshift for all epochs within the official observing windows of 3×3 months, and an efficiency of zero for all epochs outside. This is not the actual case, as shown in Figure 6.2 (number of SNe detected as a function of the observation epoch) and Figure 6.3 (SN identification pipeline efficiency as a function of redshift, taken from Dilday et al. 2010), but the assumptions can be justified as follows. Our main justification for assuming a redshift-independent observation efficiency is that none of our models explicitly take redshift into account. In other words, we assume that any of our models with the same parameters should hold for any galaxy at any redshift, given that the model itself is valid. This, coupled with the fact that our rates do not concern volumetric/spatial properties, renders the effect of a redshift-variant efficiency $\epsilon(z)$ the same as that of a redshift-invariant efficiency ϵ_z equal to $\epsilon(z)$ appropriately averaged over z for our purposes:

$$\epsilon_z = \frac{\int_0^{0.25} \epsilon(z) w_z(z) dz}{\int_0^{0.25} w_z(z) dz}, \tag{6.1}$$

where $w_z(z)$ is some appropriate weighting for a given redshift. For the assumption that the efficiency is a positive constant throughout the official observing window,

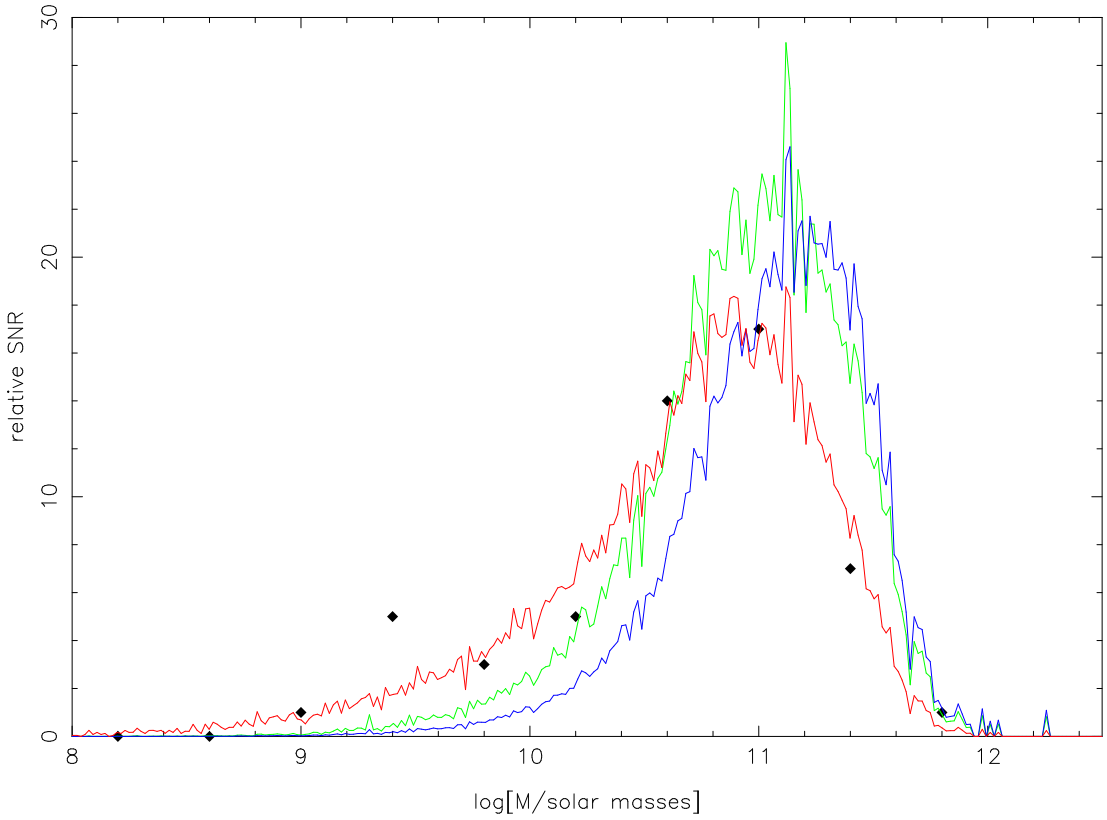

Figure 6.1: Identical to Figure 10, except that the spectroscopic galaxy sample and SNIa sample have been subjected to a redshift cut at 0.2 instead of 0.25 (see text for details). Our results have been scaled to account for observing window issues.

the argument is very similar: our models and their parameters do not explicitly contain the epoch at which the SNe were observed. Thus, for any given observation-time-dependent efficiency function $\epsilon(t)$, an equivalent constant efficiency ϵ_t can be constructed for our purposes:

$$\epsilon_t = \frac{\int_{-\infty}^{+\infty} \epsilon(t) w_t(t) dt}{\int_0^{t_{win}} w_t(t) dt}, \tag{6.2}$$

where $w_t(t)$ is again some weighting function, and t_{win} is the "official" observing window of 3 years $\times$ 3 months/year. The weighting functions $w_z(z)$ and $w_t(t)$ are hard to obtain, since doing so would require some prior assumption of what we expect to see in such an observation, which is not well understood. As a result, we are not able to analytically calculate the equivalent constant efficiency of the observations, and are only able to infer from Figure 6.2 that $\epsilon_t \sim 1$, and from Figure 6.3 that $\epsilon_z \sim 0.6$. This could potentially cause significant errors in our calculations leading up to our conclusion that $\epsilon_t \epsilon_z T \sim 0.5$ years, which could change our derived values of A, B and C by a significant factor. However, comparisons with the results of Sullivan et al. (see Figure 4.3) seem to show an agreement in terms of total predictions of SN rates, hinting that this factor is at least not overwhelmingly large. Furthermore, one must note that the "ranked" KS tests deployed in this study are only sensitive to the ratio of A and B (and C, where applicable), while being completely oblivious to the absolute values of the parameters themselves. Therefore, our rejection of the A+B model for any given value of A+B (which is one of our most important results) holds regardless of how erroneous our estimated value of $\epsilon_t \epsilon_z T$ might be. The same can be said for all our rejections/non-rejections for the other models we investigate.

Though our mass-ranked and SFR-ranked KS tests unambiguously reject the generic A+B model for any value of A and B, and support a modification with an extra "C" term, the interpretation of these results is a matter requiring great caution. Physically speaking, the $SNR = A \cdot M + B \cdot SFR + C$ model implies a massless progenitor, an inference that is unphysical.

Could the progenitors of SNe arising from the C term be due to a background intergalactic stellar population? Since such a population (e.g., Gonzalez et al. 2005) could be invisisble against the sky background, its effects on the photometric light output of the potential host galaxy should not register in SDSS photometry, and consequently have no effect whatsoever on the MPA/JHU photometric mass mea-

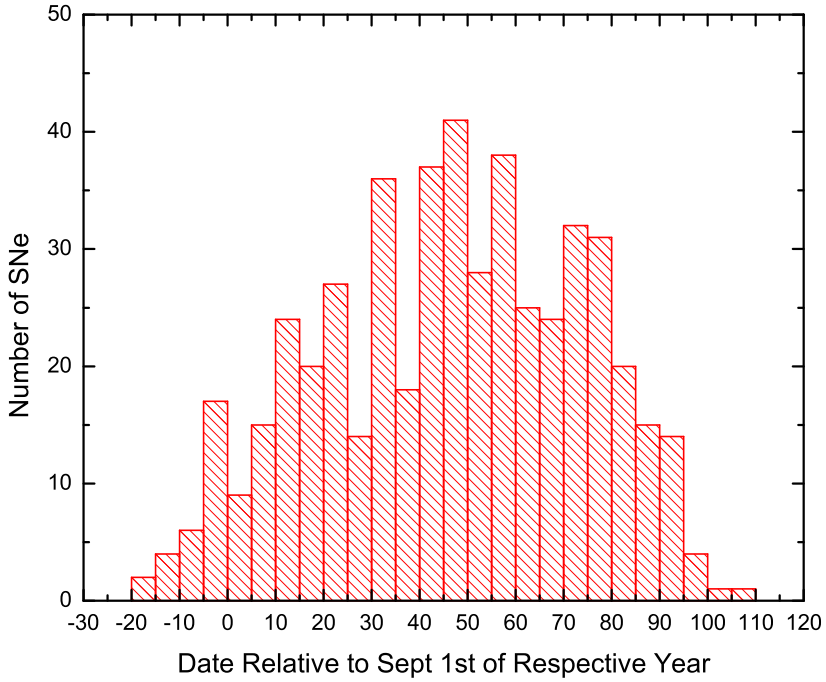

Figure 6.2: SNe Ia detection histogram relative to observing windows. The "official" observing windows correspond to 0 to 90 days on this plot.

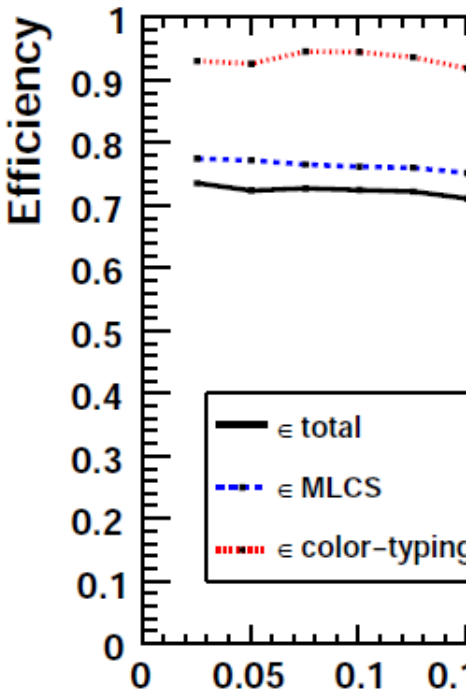

Figure 6.3: SNe Ia Identification Pipeline Efficiency as a function of redshift. This figure was taken from Dilday et al. (2010).

surements. Therefore, if intergalactic stellar mass accounts for SNe, it would result in such an apparent background such as the one observed. Also, the constant C term accounted for ∼25 of 53 SNe according to our calculations, which is marginally consistent with estimates of mass contribution from the intergalactic stellar population (Sand et al. 2011, "$0.17^{+0.14}_{-0.09}$" for X-ray galaxy clusters, and McGee & Balogh, 2010, "$47\%^{+16\%}_{-15\%}$" for low redshift galaxy groups). However, for this explanation to be feasible, it must be assumed that SNe contributed by intergalactic stars preferentially occur in or near galaxies, or else our matching algorithm would declare such SNe hostless. However, our analysis of SN spatial distributions within host galaxies (see next section for details) does not support this possibility, since SNe contributed from an intergalactic component would be more extended than the bulge.

The $SNR = A \cdot M + B \cdot SFR + C \cdot M^{-1/2}$ and $SNR = A \cdot M + B \cdot SFR + C \cdot M^{-1}$ models pass our KS tests. It is unlikely (though not an impossibility) that there exists a progenitor channel that physically favours a higher *total* SNR in low-mass galaxies, it is probable that these models merely approximate the intrinsic SNR mechanism well. One of such possibilities is given as an example in the next paragraph.

The $SNR = (A \cdot M + B \cdot SFR) \cdot (1 + C/M)$ model also passed our KS tests, and it happens to have the quality of asymptotically approaching the $SNR = A \cdot M + B \cdot SFR + C$ model at higher mass, where specific SFR is low. It could be interpreted as the result of two SN formation channels, one of which is less efficient for massive galaxies than the other. As mentioned in the introduction, existing evidence hints strongly that SNe Ia may arise from more than one scenario. Since the $SNR = (A \cdot M + B \cdot SFR) \cdot (1 + C/M)$ model suffers a very small degree of rejection by any of our tests, it is expected that a range of models supporting two formation channels, one more mass efficient than the other, would also be plausible.

It is also possible that the discrepancies we see between A+B models and our data are caused by a metallicity term. If metallicity somehow suppresses SNR, then it would account for the discrepancy observed in our low-mass galaxies; massive galaxies typically have high metallicities, and the A+B models tend to relatively overestimate the SNR for them.

As explained in Chapter 4, Cooper et al. (2009) found that SNIa rates are very likely correlated with the gas-phase metallicity of the host galaxy. However, we were not able to discriminate between different gas-phase-metallicity-dependent models due to the lack of data. This lack of data is due to only 14 SN hosts in the MPA/JHU catalogue being found with gas-phase metallicity measurements, while

VESPA stellar-phase metallicities are not good approximations for gas-phase metallicity. Even though Cooper et al. (2009) explicitly mention that they do not find SNR to be correlated stellar-phase metallicity, future work on our data may focus on finding such a correlation. After all, since the A+B models rely on both prompt and delayed channels, SN Ia rates could depend on both stellar-phase and gas-phase metallicities (the former of which would have an impact on the delayed channel).

A metallicity effect could also potentially manifest itself as a power law index, as in the x and y of the Smith et al. model ($SNR = A{\cdot}M^x + B{\cdot}SFR^y$). Of these power law index models, there is very little we can say, as we have too little data to disentangle the effects of A versus x, and B versus y. We did test and reject the Smith et al. model under the assumption that the parameters are as found by the authors, but this rejection does not rule out the possibility that the model would be plausible under a different set of parameters. We also demonstrate that a Smith model produces the observed mass separation in the sSNR vs. sSFR plane. Pfahl et al. 2009 proposed that dynamical interactions may enhance SN rates in massive systems, which would be hard to disentangle from such models, but our data does not support such an enhancement.

In summary, from our analysis regarding SN Ia host matching, we found no reason to suspect that our R_{25} matching methods or its $R_{25} = 3.8$ cut is erroneous. We also found that it matches $\sim$10% of the SNe differently relative to the more common method of matching every SN to the closest host within a certain angular distance (5 arcsecs), which is a much simpler algorithm. While the latter may serve well for some studies where a good SN-host match is not a top priority, this was not the case for this paper, so we decided to use the R_{25} matching method.

From our spectroscopic data of 19987 spectroscopic galaxies, their derived spectroscopic mass and SFR values and their hosted SNe, we used a new method to obtain the A and B parameters of the A+B model. We conclude that the generic A+B model of SNR is inconsistent with our data, regardless of the values used for A and B, with a high degree of rejection using KS tests. We show that this is due to the fact that the A+B model underestimates the SNR of low-mass galaxies (most notably Figure 4.4).

Among our corrected versions, 3 models have not yet been rejected to 90% confidence by our KS tests:

$SNR = A \cdot M + B \cdot SFR + C$,

$SNR = A \cdot M + B \cdot SFR + C \cdot M^{-1/2}$,

$SNR = (A \cdot M + B \cdot SFR) \cdot (1 + C/M)$,

with another model being rather disputable, having been rejected to a confidence level of 93%:

$SNR = A \cdot M + B \cdot SFR + C \cdot M^{-1}$.

A summary of all our models and their rejection levels can be found in Table 1. There is a bias in the derived SFRs for high-mass end galaxies, but this is not expected to have a significant effect on our KS tests for the models.

We investigated the Smith model, but were unable to obtain reasonable fits to the 4 parameters, due to a lack of sufficient data. KS tests reject the Smith model with parameter values as found by Smith et al. 2011, but we are unable to rule out the possibility of a different set of parameters matching our data, as the x parameter could theoretically address the issue of the A+B model underestimating the SNR of low-mass galaxies, and different values for B and y could adjust the SFR dependence.

An attempt is made to create a metallicity-dependent SNR model, but due to a lack of sufficient data, we were not able to discriminate between different models and parameters for a gas-phase metallicity-dependent model. Stellar-phase metallicity is shown to both have a poor correlation with gas-phase metallicity, and have little effect on the SNR, which is in agreement with the literature (Cooper et al. 2009).

6.2 SNR Distribution Within Host Galaxies

The other main task of this work was to investigate how SNe are distributed within their own host galaxies compared to the distribution of light in different galaxy components. Surprisingly, no study has yet been conducted on this subject prior to this work. The next few paragraphs focus on our findings in this very new field, as well as our interpretations of them.

We find that, for our sample, the null hypotheses that SNe follow either total galaxy light or disk light are both rejected at $> 99\%$ confidence. The hypothesis that SNe follow bulge light is not rejected, seemingly hinting that SNe progenitors are a stellar population unique to host bulges and evenly distributed within bulge light.

We tried different cutoff values for our calculations of total light from $R_{25} = 1$ to $R_{25} = 3.8$. It is shown that, as long as the cutoff didn't allow the bulge light to dominate (which it did in the case for $R_{25} = 1$), the distribution of total light could not be reconciliated with that of the SNe. Beyond $R_{25} = 3.8$, SN completeness issues prevented us from investigating further. Therefore, we conclude that total light

completeness is not the cause of the issue.

Seeing effects are unlikely to be the cause of these results. The galaxy profiles from Simard et al. (2011) have been corrected simultaneously for seeing effects and PSFs by deconvolution. For the SNe, all we use for our analysis is the central position, which should not be significantly affected by seeing effects for relatively bright SNe. This is due to the fact that seeing effects would only extend a point source (such as a SN Ia) in a circularly symmetric way. For faint SNe from which only a few photons are received, we estimate the errors, under the assumption that seeing effects distort point sources into gaussian distributions, as follows. Considering a one-dimensional case,

$$\frac{(\bar{x}_i - \mu)}{\sigma/\sqrt{N}} \tag{6.3}$$

should follow a Gaussian distribution with a mean of 0 and a standard deviation of 1, where $\bar{x}_i$ is the mean position of the detected photons, μ is the intrinsic SN position, N is the number of photons observed, and σ is the standard deviation of the seeing disc. The seeing disc is known to have a FWHM of $1.4''$ (Kelly et al. 2008), corresponding to a σ of $0.59''$. It could be seen that the numerator is the error of the SN position. Thus, the errors are estimated to be less than $0.1''$ for any SN which has more than 36 photons observed, which is insignificant for our purposes.

One last effect one must take into account before trusting the result that SNR conforms better to the bulge- than the disk-light distribution is the possibility that galactic nuclei (a component even more concentrated than the bulge, available in most galaxies) may have significantly distorted the galaxy profile fits of Simard et al. (2011). The galaxy profile fits were made using an exponential disk component, and a Sérsic profile with a variable Sérsic index. The authors assumed that the effect of a nucleus is negligible, which is not always the case. There are 2 possibilities by which the presence of a nucleus can affect the fits. The first is that the fitting algorithm could accidentally fit an exponential profile to the nucleus, and attempt to fit the rest of the galaxy with a Sérsic profile. In this case, the disk scale radius would be extremely small, even smaller than what the bulge *scale radius* would have been, while the bulge half light radius would be larger than the half light radius of the entire galaxy. Thus, it is expected that the resultant disk scale radius is at least 4 orders of magnitude larger than the bulge half-light radius. Examining Table 5.1, no such case is found. The second way by which a nucleus could affect our results is by masquerading as

either a part or the whole of the bulge of the galaxy. In this case, the galaxy profiles would be even more concentrated than they actually are, and we should see that SN spatial distributions are more diffuse than galaxy light, if we assume that SNe are distributed in the same way as galaxy light. Thus, we conclude that distortion of galaxy profiles by galactic nuclei could not have reproduced our results, had the distribution of SNe conformed to that of galaxy light. Worthy of note is the fact that galactic nuclei themselves are unlikely to have contributed a significant number of SNe, or otherwise there should have been many more inner-region SNe in the KS tests of Chapter 5.

Comparing the SN spatial distributions with a disk profile centrally concentrated via a power law shows that only disk light to the power of at least 2.4 would reconciliate the disk light with SN formation. This was done primarily to investigate whether SNR might follow the distribution of interstellar material, but the lower limit of the power law (which is much larger than the index of the Schmidt-Kennicutt law) shows that this cannot be the case.

We then test, under the assumption that disks contribute to SNR, how large the contribution is in comparison to the bulge. This is done by a series of follow-up KS tests. They show that, under the assumption that SNe follow a composite light profile of $B+\epsilon D$, where B is the bulge light, D is the disk light, and ϵ is some constant factor, then for any $\epsilon > 0.3$, the composite light profile is rejected too. This hints further that disk light has very little to do with SN formation. Considering the contributions of bulges and disks to the masses and star formation rates, it is very probable that the A+B model does not intrinsically reflect the source of progenitors within a galaxy.

However, if this were the case, it would be expected that SNe would predominantly occur in bulge-dominated systems, while it is shown in Table 3 that this is not the case. From Table 3, it can be seen that the bulge and disk components are roughly equal in terms of contribution to total light, and the number of bulge-dominated and disk-dominated galaxies are roughly equal for the original sample of 81331 galaxies. In other words, for the original sample of galaxies from Simard et al. with Sérsic cuts applied, we have no reason to believe that the sample itself shows a preference to either bulge or disk populations. It can also be seen from Table 3 that the statistics show that the 78 galaxy subsample known to host SNe are not preferentially bulge-dominated systems. This shows that bulge light cannot be the intrinsic "flowerbed" of SN progenitors, but rather that the distribution of the population leading to SNe somehow correlates very well with the distribution of bulge light.

If any environmental preference of SNe could be inferred from Table 3, the statistics seem to marginally show that SNe Ia mainly occur in disk dominated systems (45 out of 78), which would be in general agreement with the literature (e.g., Raskin et al. 2008). However, this is only a 1σ result, and hence is not significant.

This result also does not support the hypothesis in the last section that the C term in the $SNR = A \cdot M + B \cdot SFR + C$ model is caused by intergalactic SNe, for reasons as follows. The bulge + disk decompositions by Simard et al. used SDSS photometry, which would not have registered the signal from an intergalactic stellar population, so if it were the case that the C term were supported by intergalactic SNe, about half the SNe ($\sim$25/53 of the total,) should be randomly distributed in a way that disregards the light distribution of the galaxy itself. The resulting spatial distribution of SNe would be highly extended, and less likely to follow bulge light than disk light. The spatial distribution should also exhibit linear enhancement of SNR at large distances from the galactic centre in Figure 5.3, proportional to the distance, since the number of intergalactic SNe occuring at a distance R from the centre of a galaxy should be proportional to $2\pi RdR$.

As mentioned above, the interpretation of our results is that the distribution of the stellar population comprising SN progenitors somehow correlates very well with the distribution of bulge light, even though members of the population do not generally contribute to the bulge light itself.

In summary, by reconstructing seeing-corrected host galaxy light profiles with bulge+disk decompositions from the results of Simard et al. 2011 (after applying a Sérsic index cut of 2), we show that the spatial distribution of SNe Ia within a host galaxy conforms neither to the spatial distribution of total galaxy light, nor that of the disk light. Plotting the galaxy-luminosity-weighted summed profiles of all galaxies in our sample (81331 in total) in physical units (kpc), we see that the spatial distribution of bulge light matches that of SNe very well. Subsequent plots using selected samples from different bulge-to-total light ratio regimes further drive home this issue, but the fact that SNe do not preferentially occur in bulge-dominated galaxies does not support the hypothesis that SNe are a direct result of bulge populations.

Bibliography

[Abazajian, K.N. et al. (2009)] Abazajian, K.N. et al. , 2009. APJS, 182, 543.

[Astier, P. et al. (2006)] Astier, P. et al. , 2006. A&A, 447, 31.

[Benitez-Herrera, S. et al. (2011)] Benitez-Herrera, S. et al. , 2011. arXiv1109.0873.

[Bertin, E. , Arnouts, S. (1996)] Bertin, E. , Arnouts, S. , 1996. A&AS, 117, 393.

[Bianco, F. et al. (2011)] Bianco, F. et al. , 2011. AAS, 21730807.

[Brinchmann, J. et al. (2004)] Brinchmann, J. et al. , 2004. MNRAS, 351, 1151.

[Bruzual, G. , Charlot, S. (2003)] Bruzual, G. , Charlot, S. , 2003. MNRAS, 344, 1000.

[Chandrasekhar, S. (1931)] Chandrasekhar, S. , 1931. ApJ, 74, 81.

[Charlot, S. , Fall, S.M. (2000)] Charlot, S. , Fall, S.M. , 2000. ApJ, 539, 718.

[Charlot, S. , Longhetti, M. (2001)] Charlot, S. , Longhetti, M. , 2001. MNRAS, 323, 887.

[Ciotti, L. , Bertin, G. (1999)] Ciotti, L. , Bertin, G. , 1999. A&A, 352, 447.

[Colgate, S.A. (1979)] Colgate, S.A. , 1979. APJ, 232, 404.

[Cooper, M.C. et al. (2009)] Cooper, M.C. et al. , 2009. APJ, 704, 687.

[de Vaucouleurs, G. (1948)] de Vaucouleurs, G. , 1948. Ann. d'Astroph, 11, 247.

[Della Valle, M. , Livio, M. (1994)] Della Valle, M. , Livio, M. , 1994. ApJ, 423, 31.

[Dilday, B. et al. (2008)] Dilday, B. et al. , 2008. ApJ, 682, 262.

[Dilday, B. et al. (2010a)] Dilday, B. et al. , 2010a. ApJ, 713, 1026.

[Dilday, B. et al. (2010b)] Dilday, B. et al. , 2010b. ApJ, 715, 1021.

[Doi, M. (2010)] Doi, M. , 2010. AJ, 139, 1628.

[Filippenko, A.V. (1997)] Filippenko, A.V. , 1997. ARA&A, 35, 309.

[Fioc, M. , Rocca-Volmerange, B. (1997)] Fioc, M. , Rocca-Volmerange, B. , 1997. A&A, 326, 950.

[Fisher, D.B. , Drory, N. (2010)] Fisher, D.B. , Drory, N. , 2010. ApJ, 716, 942.

[Fisher, D.B. , Drory, N. , Fabricius, M.H. (2009)] Fisher, D.B. , Drory, N. , Fabricius, M.H. , 2009. ApJ, 697, 630.

[Folatelli, G. et al. (2010)] Folatelli, G. et al. , 2010. AJ, 139, 120.

[Forster, F. et al. (2006)] Forster, F. et al. , 2006. MNRAS, 368, 1893.

[Frieman, J.A. et al. (2008)] Frieman, J.A. et al. , 2008. AJ, 135, 338.

[Fruchter, A.S. et al. (2006)] Fruchter, A.S. et al. , 2006. Nature, 441, 463.

[Gilfanov, M., Bogdán, A. (2010)] Gilfanov, M., Bogdán, A. , 2010. Nature, 463, 924.

[Gonzalez, A.H. et al. (2005)] Gonzalez, A.H. et al. , 2005. ApJ, 618, 195.

[Greggio, L. (2005)] Greggio, L. , 2005. A&A, 441, 1055.

[Gunn, J.E. et al. (1998)] Gunn, J.E. et al. , 1998. AJ, 116, 3040.

[Gupta, R.R. et al. (2011)] Gupta, R.R. et al. , 2011. ApJ, 740, 92.

[Guy, J. et al. (2005)] Guy, J. et al. , 2005. A&A, 443, 781.

[Hachisu, I. (1996)] Hachisu, I. , 1996. ApJ, 470, 97.

[Han, Z. , Podsiadlowski, Ph. (2004)] Han, Z. , Podsiadlowski, Ph. , 2004. MNRAS, 350, 1301.

[Hillebrandt, W. , Niemeyer, J.C. (2000)] Hillebrandt, W. , Niemeyer, J.C. , 2000. ARA&A, 38, 191.

[Hogg, D.W. (1999)] Hogg, D.W. , 1999. arXiv:astro-ph/9905116.

[Hopkins, A.M. , Beacom, J.F. (2006)] Hopkins, A.M. , Beacom, J.F. , 2006. ApJ, 651, 142.

[Howell, D.A. et al. (2006)] Howell, D.A. et al. , 2006. Nature, 443, 308.

[Kasen, D. et al. (2009)] Kasen, D. et al. , 2009. Nature, 229.

[Kauffmann, G. et al. (2003)] Kauffmann, G. et al. , 2003. MNRAS, 341, 33.

[Kelly, P.L. (2008)] Kelly, P.L. , 2008. ApJ, 687, 1201.

[Kennicutt, R.C. (1998)] Kennicutt, R.C. , 1998. ARA&A, 36, 189.

[Kewley, L.J. et al. (2001)] Kewley, L.J. et al. , 2001. ApJS, 132, 37.

[Kobayashi, C. et al. (2000)] Kobayashi, C. et al. , 2000. ApJ, 539, 26.

[Kormendy, J. (2011)] Kormendy, J. , 2011. Nature, 469, 374.

[Lampeitl, H. et al. (2010)] Lampeitl, H. et al. , 2010. ApJ, 722, 566.

[Li, W. et al. (2011)] Li, W. et al. , 2011. MNRAS, 412, 1473.

[Mannucci, F. et al. (2005)] Mannucci, F. et al. , 2005. A&A, 433, 807.

[McGee, S.L. , Balogh, M.L. (2010)] McGee, S.L. , Balogh, M.L. , 2010. MNRAS, 403, 79.

[McMillan, R.J. , Ciardullo, R. (1996)] McMillan, R.J. , Ciardullo, R. , 1996. ApJ, 473, 707.

[Mennekens, N. et al. (2010)] Mennekens, N. et al. , 2010. A&A, 515, 89.

[Minkowski, R. (1941)] Minkowski, R. , 1941. PASP, 53, 224.

[Neill, J.D. et al. (2006)] Neill, J.D. et al. , 2006. AJ, 132, 1126.

[Nomoto, M.(1982)] Nomoto, M., 1982. ApJ, 253, 798.

[Perlmutter, S. et al. (1997)] Perlmutter, S. et al. , 1997. ApJ, 483,565.

[Perlmutter, S. et al.(1999)] Perlmutter, S. et al., 1999. ApJ, 517,565.

[Pfahl, E., Scannapieco, E., Bildsten, L. (2009)] Pfahl, E., Scannapieco, E., Bildsten, L. , 2009. ApJ, 695,111.

[Phillips, M.M. (1993)] Phillips, M.M. , 1993. ApJ, 413,105.

[Pritchet, C.J. et al. (2008)] Pritchet, C.J. et al. , 2008. ApJ, 683, 25.

[Pritchet, C.J. et al. (2012)] Pritchet, C.J. et al. , 2012. in preparation.

[Raskin, C. et al. (2008)] Raskin, C. et al. , 2008. ApJ, 689, 358.

[Riess, A.G. et al. (1998)] Riess, A.G. et al. , 1998. AJ, 116, 1009.

[Riess, A.G. et al. (1999)] Riess, A.G. et al. , 1999. AJ, 118, 2668.

[Sérsic, J.L. (1968)] Sérsic, J.L. , 1968. Atlas de galaxias australes. Observatorio Astronomico, Cordoba.

[Salim, S. et al. (2007)] Salim, S. et al. , 2007. ApJS, 173, 267.

[Sand, D.J. et al. (2011)] Sand, D.J. et al. , 2011. ApJ, 729, 142.

[Scannapieco, E. , Bildsten, L. (2005)] Scannapieco, E. , Bildsten, L. , 2005. ApJ, 629, 85.

[Simard, L. et al. (2002)] Simard, L. et al. , 2002. ApJS, 142, 1.

[Simard, L. et al. (2011)] Simard, L. et al. , 2011. ApJS, 196, 11.

[Smith, M. et al. (2011)] Smith, M. et al. , 2011. arxiv1108.4923.

[Sullivan, M. et al. (2006)] Sullivan, M. et al. , 2006. ApJ, 648, 868.

[Sullivan, M. et al. (2010)] Sullivan, M. et al. , 2010. MNRAS, 406, 782.

[Thompson, T.A. (2010)] Thompson, T.A. , 2010. arXiv1011.4322.

[Thuan, T.X. , Gunn, J.E. (1976)] Thuan, T.X. , Gunn, J.E. , 1976. PASP, 88, 543.

[Tojeiro, R. et al. (2009)] Tojeiro, R. et al. , 2009. ApJS, 185, 1.

[Totani, T. et al. (2008)] Totani, T. et al. , 2008. PASJ, 60, 1237.

[Tremonti, C.A. et al. (2004)] Tremonti, C.A. et al. , 2004. ApJ, 613, 898.

[Wang, B. et al. (2010)] Wang, B. et al. , 2010. ScChG, 53, 586.

Appendix A

Summary of Different Cosmology Distance Measures

A.1 A Few Useful Parameters

Before introducing the various cosmology distance measures, it is useful to introduce a few parameters which would simplify the explanations of the following sections.

The universe is an expanding entity. The rate at which this happens is the "Hubble parameter" H, as shown below:

$$H = 100\ h\ \mathrm{km{\cdot}s^{-1}{\cdot}Mpc^{-1}}, \tag{A.1}$$

where h is a parameter which is a function of time. In the present-day universe, it is measured to be about 0.7. The Hubble parameter of the present-day universe is denoted as H_0, which is called the Hubble constant (note that H changes with time, so H_0 is only a constant if the time at which it is measured is fixed). The inverse of the Hubble constant is the Hubble time t_H

$$t_H = \frac{1}{H_0}. \tag{A.2}$$

Physically, t_H would be the age of the universe since the Big Bang if the expansion velocity of all objects had remained the same throughout the history of the universe. t_H multiplied by the speed of light c gives the Hubble distance D_H

$$D_H = ct_H = \frac{c}{H_0}, \tag{A.3}$$

which would have been the radius of the observable universe today, had the recession velocity of the edge of the observable universe (also called the particle horizon) remained a constant since the Big Bang.

Another three useful parameters are Ω_M, Ω_Λ and Ω_k, which are measures of mass density, dark energy density and curvature of the universe at the present epoch respectively. They are defined as

$$\Omega_M = \frac{8\pi G\rho_0}{3H_0^2}, \tag{A.4}$$

$$\Omega_\Lambda = \frac{\Lambda c^2}{3H_0^2}, \tag{A.5}$$

$$\Omega_k = -\frac{kc^2}{a_0^2 H_0^2}, \tag{A.6}$$

where G is the gravitational constant, Λ is the cosmological constant, ρ_0 is the density of the universe at the present epoch, and a is the scale factor at the present epoch. They are correlated with each other by

$$\Omega_M + \Omega_\Lambda + \Omega_k = 1. \tag{A.7}$$

For a flat universe, $k = 0$, and hence $\Omega_k = 0$, $\Omega_M + \Omega_\Lambda = 1$.

A.2 Comoving Distance

Comoving distance D_C is defined as a distance measure between two objects in the universe which remains constant if the two objects are stationary with respect to the fabric of the universe (i.e. if the expansion of the universe is the only source of relative motion between the two). In a flat universe, it can be expressed as

$$D_C = D_H \int_0^z \frac{dx}{E(x)}, \tag{A.8}$$

where $E(z) = \sqrt{\Omega_M(1+z)^3 + \Omega_k(1+z)^2 + \Omega_\Lambda}$, and $\Omega_k = 0$ for a flat universe. Worthy of note is that, if the universe were not flat (which it is), the radial comoving distance and the transverse comoving distance would not be equal.

A.3 Angular Diameter Distance

The angular diameter distance D_A from an observer to an object is defined as the ratio of the object's physical size to its angular size as seen by the observer. In a flat universe,

$$D_A = \frac{D_C}{1+z}, \tag{A.9}$$

where z is the redshift.

A.4 Luminosity Distance

The luminosity distance D_L from an observer to a given object is defined such that the flux received from that object could be expressed as

$$F = \frac{L}{4\pi D_L^2}. \tag{A.10}$$

In a flat universe, it is equal to

$$D_L = D_C(1+z), \tag{A.11}$$

where z is the redshift.